High-resolution volumetric imaging constrains compartmental models to explore synaptic integration and temporal processing by cochlear nucleus globular bushy cells

George A. Spirou[1†*], Matthew G. Kersting[1‡], Sean Carr[1], Bayan Razzaq[2§], Carolyna Y. Alves-Pinto[1¶], Mariah Dawson[2], Mark H. Ellisman[3,4], Paul B. Manis[5†*,6]**

***For correspondence:** gspirou@usf.edu (GAS); pmanis@med.unc.edu (PBM)

[†]These authors contributed equally to this work.

Present address: [‡]Noblis Inc., Reston, VA USA; [§]Department of Neurosurgery, Stony Brook University, Stony Brook, NY, USA; [¶]Department of Biomedical Engineering, Johns Hopkins University, Baltimore, USA; [**]PNC Financial Services, Cleveland, OH, USA

[1]Department of Medical Engineering, University of South Florida, Tampa FL, USA; [2]Department of Otolaryngology, Head and Neck Surgery, West Virginia University, Morgantown, WV, USA; [3]Department of Neurosciences, University of California San Diego, La Jolla, CA, USA; [4]National Center for Microscopy and Imaging Research, University of California, San Diego, La Jolla, CA, USA; [5]Department of Otolaryngology/Head and Neck Surgery, University of North Carolina, Chapel Hill, NC, USA; [6]Department of Cell Biology and Physiology, University of North Carolina, Chapel Hill, NC, USA

Abstract

Globular bushy cells (GBCs) of the cochlear nucleus play central roles in the temporal processing of sound. Despite investigation over many decades, fundamental questions remain about their dendrite structure, afferent innervation, and integration of synaptic inputs. Here, we use volume electron microscopy (EM) to construct synaptic maps that precisely specify convergence ratios and synaptic weights for auditory- nerve innervation and accurate surface areas of all postsynaptic compartments. Detailed biophysically-based compartmental models can help develop hypotheses regarding how GBCs integrate inputs to yield their recorded responses to sound. We established a pipeline to export a precise reconstruction of auditory nerve axons and their endbulb terminals together with high-resolution dendrite, soma, and axon reconstructions into biophysically-detailed compartmental models that could be activated by a standard cochlear transduction model. With these constraints, the models predict auditory nerve input profiles whereby all endbulbs onto a GBC are subthreshold (coincidence detection mode), or one or two inputs are suprathreshold (mixed mode). The models also predict the relative importance of dendrite geometry, soma size, and axon initial segment length in setting action potential threshold and generating heterogeneity in sound-evoked responses, and thereby propose mechanisms by which GBCs may homeostatically adjust their excitability. Volume EM also reveals

new dendritic structures and dendrites that lack innervation. This framework defines a pathway from subcellular morphology to synaptic connectivity, and facilitates investigation into the roles of specific cellular features in sound encoding. We also clarify the need for new experimental measurements to provide missing cellular parameters, and predict responses to sound for further *in vivo* studies, thereby serving as a template for investigation of other neuron classes.

Introduction

Both spherical and globular subpopulations of bushy cells of the cochlear nucleus (CN) encode temporal fine structure and modulation of sound with high fidelity, but the globular bushy cells (GBCs) do so with greater precision. (***Bourk, 1976***; ***Joris et al., 1994a***,b; ***Wei et al., 2017***; ***Spirou et al., 1990***; ***Smith et al., 1991***). GBCs, many of which are located in the auditory nerve fiber (ANF) entry zone, play central roles in hearing as they are essential for binaural processing and are a key cell type that defines and drives the early stages of the lemniscal auditory pathway (***Warr, 1966***; ***Tolbert et al., 1982***; ***Smith et al., 1991***; ***Yin et al., 2019***; ***Spirou et al., 1990***). The temporal encoding capabilities of GBCs arise from a convergence circuit motif whereby many ANFs project, via large terminals called endbulbs that contain multiple active synaptic zones, onto the cell body. (***Lorente de Nó, 1933***, ***1981***; ***Tolbert and Morest, 1982***; ***Brawer et al., 1974***; ***Ryugo and Fekete, 1982***; ***Ryugo and Sento, 1991***; ***Ryugo et al., 1993***; ***Sento and Ryugo, 1989***; ***Spirou et al., 2005***; ***Cant and Morest, 1979a***; ***Nicol and Walmsley, 2002***; ***Lauer et al., 2013***; ***Held, 1893***). Furthermore, the BC membrane has low threshold K^+ channels and a hyperpolarization-activated conductance (***Rothman and Manis, 2003a***,b; ***Manis and Marx, 1991***; ***Cao et al., 2007***; ***Cao and Oertel, 2011***) that together constrain synaptic integration by forcing a <2 ms membrane time constant and actively abbreviate synaptic potentials. This short integration time functionally converts the convergence circuit motif into either a slope-sensitive coincidence detection mechanism or a first input event detector, as tested in computational models, depending upon whether activity in the ANF terminals is subthreshold or suprathreshold (***Joris et al., 1994a***; ***Rothman et al., 1993***; ***Rothman and Young, 1996***). The number of convergent ANF inputs onto GBCs has been estimated using light microscopy and counted using electron microscopy (EM) for a small number of neurons (***Liberman, 1991***; ***Spirou et al., 2005***). However, neither approach permits more realistic assessment of biological variance within sub- and suprathreshold populations of ANF terminals, nor their definition based on delineation of actual synaptic contacts to estimate synaptic weight. These parameters are essential for prediction of neural activity and understanding the computational modes employed by BCs.

Although the preponderance of ANF inputs are somatically targeted, the dendrites of BCs exhibit complex branching and multiple swellings that are difficult to resolve in light microscopic (LM) reconstructions (***Lorente de Nó, 1981***). Consequently the dendritic contributions to the electrical properties of BCs have not been explored. Innervation of dendrites and soma was revealed from partial reconstruction from EM images (***Ostapoff and Morest, 1991***; ***Tolbert and Morest, 1982***; ***Smith and Rhode, 1987***), but values are often estimated as percent coverage rather than absolute areas. Sub-sampling using combined Golgi-EM histology has shown innervation of swellings and dendritic shafts (***Ostapoff and Morest, 1991***), and immunohistochemistry has further indicated the presence of at least a sparse dendritic input (***Gómez-Nieto and Rubio, 2009***). Nonetheless, a complete map of synapse location across dendrite compartments, soma, and axon has not been constructed.

To resolve these longstanding issues surrounding this key cell type, we employed volume electron microscopy (EM) in the auditory nerve entry zone of the mouse CN to provide exact data on numbers of endbulb inputs and their active zones along with surface areas of all cellular compartments. Nanoscale connectomic studies typically provide neural connectivity maps at cell to cell

resolution (***Zheng et al., 2018***; ***Scheffer et al., 2020***; ***Turner et al., 2022***; ***Bae et al., 2021***; ***Shapson-Coe et al., 2021***; ***Cook et al., 2019***). We extend these studies and previous modeling studies of BCs, by using detailed reconstructions from the EM images to generate and constrain compartmental models that, in turn, are used to explore mechanisms for synaptic integration and responses to temporally modulated sounds. A large range of endbulb sizes was quantified structurally, and the models predict a range of synaptic weights, some of which are suprathreshold, and responses to modeled acoustic input that exhibit enhanced temporal processing relative to auditory nerve. The pipeline described here for compartmental model generation yields a framework to predict sound-evoked activity and its underlying cellular mechanisms, and a template on which to map new structural, molecular and functional experimental data.

Results

Cellular organization of the auditory nerve root region of the mouse cochlear nucleus

Despite many years of study, fundamental metrics on morphology of BC somata, dendrites and axons, and the synaptic map of innervation across these cellular compartments is far from complete. We chose volume electron microscopy (serial blockface electron microscopy (SBEM)) to systematically address these fundamental questions at high resolution and quantify structural metrics, such as membrane surface area and synaptic maps, in combination with compartmental modeling that is constrained by these measurements, to deepen our understanding of BC function. We chose the mouse for this study for three reasons. First, the intrinsic excitability, ion channel complement, and synaptic physiology of mouse bushy cells has been extensively characterized, which facilitates developing biophysically-based computational representations. Second, the mouse CN is compact, permitting the evaluation of a larger fraction of the circuit in a prescribed EM volume. Third, the tools available for mouse genetics provide an advantage for future studies to identify cells and classes of synapses, which can be mapped onto the current image volume. The image volume was taken from the auditory nerve entry zone of the mouse CN, which has a high concentration of BCs. The image volume was greater than 100 μm in each dimension and contained 26 complete BC somata and 5 complete somata of non-BCs that were likely multipolar cells (MCs; beige and rust colored, respectively, in ***Figure 1***). Fascicles of ANFs coursed perpendicular to other fascicles comprised, in part, of CN axons, including those of BCs, as they exit into the trapezoid body (ANF and BC (colored mauve) axons, respectively in ***Figure 1***A).

Segmentation of neurons from the image volume revealed BC somata as having eccentrically located nuclei (25/26 BCs) with non-indented nuclear envelopes (25/26 BCs; the one indented nuclear envelope was eccentrically located), and stacks of endoplasmic reticulum only along the nuclear envelope facing the bulk of the cell cytoplasm (26/26 BCs; ***Figure 1***B-C). Based on these cytological criteria, location of cells in the auditory nerve root, and multiple endbulb inputs (see below), we classify these cells as globular bushy cells (GBC). We use that notation throughout the remainder of the manuscript.

Myelinated ANF's connected to large end-bulb terminals synapsing onto the GBC somata. Reconstructions from volume EM permitted accurate measurement of the directly apposed surface area (ASA) between the endbulb terminal and postsynaptic membrane, and identification of synapses as clusters of vesicles along the presynaptic membrane (***Figure 1***B-D, D'). In a subset of terminals we counted the number of synapses. Because the density of synapses showed only a small decrease with increasing ASA (***Figure 1***F), we used the average density to estimate the number of synapses in each terminal and to set synaptic weights in computational models (***Figure 1***F, and see Methods).

An important goal of this project was to provide accurate measurements of membrane surface

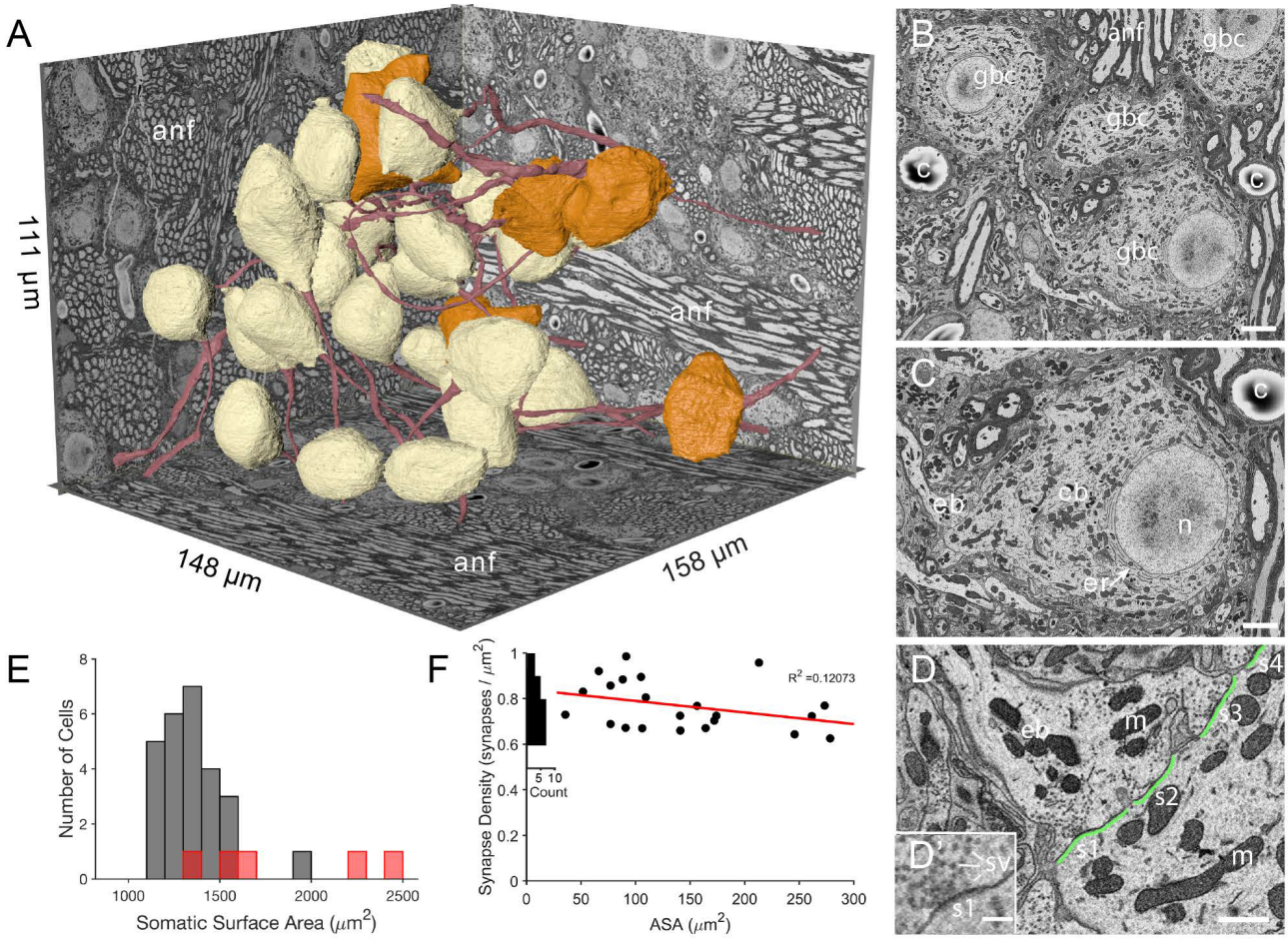

Figure 1. The imaged volume in the cochlear nucleus captures globular bushy (GBC) and multipolar cells (MC), and reveals synaptic sites. (**A**) The VCN region that was imaged using SBEM is depicted within walls of the image volume. Twenty-six GBCs (beige) and 5 MCs (orange) are shown with their axons (red). Left rear wall transects auditory nerve (anf) fascicles, which run parallel to the right rear wall and floor. Non-anf axons exit into the right rear wall and floor as part of other fascicles that are cross-sectioned. The complete volume can be viewed at low resolution in Figure 1–***video 1***. (**B**) Example image, cropped from the full field of view, from the data set in panel A. Field of four GBC (bc) cell bodies, myelinated axons in anf fiber fascicles, and capillaries (c). (**C**) Closeup of the cell body (cb) of lower right GBC from panel **B**, illustrating the eccentrically located nucleus (n), short stacks of endoplasmic reticulum (er) aligned with the cytoplasm-facing side of the nuclear envelope, and contact by an endbulb (eb). (**D**) Closeup of the labeled endbulb contacting the cell in panel **C** (eb), revealing its initial expansion along the cell surface. Apposed pre- and postsynaptic surface area (ASA; green) are accurately determined by excluding regions with intercellular space (ASA is discontinuous), and synaptic sites (s1-4) are indicated as clusters of vesicles with some contacting the presynaptic membrane. (**D'**) Inset in panel **D** is closeup of synapse at lower left in panel **D**. It shows defining features of synapses in these SBEM images, which include clustering of vesicles near the presynaptic membrane, convex shape of the postsynaptic membrane, and in many cases a narrow band of electron-dense material just under the membrane, as evident here between the "s1" symbol and the postsynaptic membrane.Green line indicates regions of directly apposed pre- and postsynaptic membrane, and how this metric can be accurately quantified using EM. (**E**) Histogram of all somatic surface areas generated from computational meshes of the segmentation. GBCs are denoted with grey bars and MCs with red bars. (**F**) Synapse density plotted against ASA shows a weak negative correlation. Marginal histogram of density values is plotted along the ordinate. Scale bars = 5 μm in **B**, 2 μm in **C**, 1 μm in **D**, 250 nm in **D'**.

Figure 1–Figure supplement 1. Steps in mesh generation and compartmental representation from EM volumes, related to Figure 1A.

Figure 1–video 1. Exploration of the relation between an image volume and a globular bushy cell (GBC) mesh derived from that volume. This video opens with a top-down view of the SBEM image volume from the ventral cochlear nucleus. The video zooms in as the volume is slowly cut away to reveal GBC05, including its dendrites (red), cell body (beige), axon (pink), and all large somatic inputs (various colors). The perspective then shifts laterally to view several of the large terminals (various colors) contacting the cell body.

areas, in order to anchor compartmental models of GBC function and facilitate comparison across species and with other cell types. We standardized a procedure based on a method to generate computational meshes (***Lee et al., 2020a***), yet preserve small somatic processes (see Methods and Figure 1–***Figure Supplement 1***). The population of GBC somatic surface areas was slightly skewed from a Gaussian distribution (1352 (SD 168.1) μm^2), with one outlier (cell with indented nucleus) near 2000 μm^2 (***Figure 1***E). The MCs (red bars in ***Figure 1***E) may represent two populations based on cells with smaller (<1700 μm^2) and larger (>2000 μm^2) somatic surface area.

A comparison of two proposed synaptic convergence motifs for auditory nerve inputs onto globular bushy cells

With image segmentation parameters set, we next addressed competing models for synaptic organization by which GBCs can achieve higher temporal precision at the onset of sound and in phase locking to periodic stimuli than ANFs, and exhibit physiologically relevant values for spike regularity (***Rothman et al., 1993***; ***Joris et al., 1994b***,a). These models are based on convergence of large, somatic endbulbs of Held (***Rouiller et al., 1986***; ***Liberman, 1991***; ***Ryugo and Fekete, 1982***) (***Figure 2***A,B). At one extreme, all convergent inputs, although harboring multiple release sites, are subthreshold for spike generation, and also of similar weight. With the functional attribute of a brief temporal integration window defined by the short membrane time constant, this convergence motif defines GBC operation as a coincidence detector. At the other extreme, all somatic ANF inputs are large and suprathreshold, also of similar weight. In this scenario, the GBC operates as a latency detector, such that the shortest latency input on each stimulus cycle drives the cell. In both models, the GBC refractory period suppresses delayed inputs.

In order to evaluate the predictions of these models, key metrics of the number of ANF terminal inputs and the weights of each are required. We first determined a size threshold to define endbulb terminals. All non-bouton (endbulb) and many bouton-sized somatic inputs onto 21 of 26 GBCs were reconstructed, including all somatic inputs onto 2 cells. We then compiled a histogram of input size based on ASA. A minimum in the distribution occurred at $\sim 25 - 35\ \mu m^2$, so all inputs larger than 35 μm^2 were defined as large terminals of the endbulb class (***Figure 2***C). We next investigated whether this threshold value captured those terminals originating from ANFs, by tracing retrogradely along the axons. Terminals traced to branch locations on ANFs within the volume matched the size range of large terminals estimated from the histogram (only two were smaller than the threshold value), and were all (except one branch) connected via myelinated axons (***Figure 2***C inset, top). Nearly all axons of the remaining large terminals were also myelinated (***Figure 2***C inset, middle). The remaining few unmyelinated axons associated with large terminals immediately exit the image volume, and may become myelinated outside of the field of view (***Figure 2***C inset, bottom, right of vertical dashed line). These data together lent confidence to the value of 35 μm^2 as the size threshold for our counts of endbulb terminals. We use the terminology "endbulb" or "large terminal" interchangeably throughout this report.

Five-12 auditory nerve endbulbs converge onto each globular bushy cell.

After validating the size range for the endbulb class, we found a range of 5-12 convergent endings (***Figure 2***D, right). This range exceeds prior estimates of 4-6 inputs, based on physiological measures in mouse (***Cao and Oertel, 2010***). We next inquired whether the range of input size was similar across all cells. Inspecting the largest input onto each cell revealed, however, two groups of GBCs, which could be defined based on whether their largest input was greater than or less than 180 μm^2 (histogram along left ordinate in ***Figure 2***D). Plotting endbulb size in rank order (largest to smallest) for each cell revealed that, excluding the largest input, the size distributions of the remaining inputs overlapped for both groups of GBCs (black and red traces in ***Figure 2***D). A catalogue of all inputs for the representative cells illustrates these two innervation patterns and

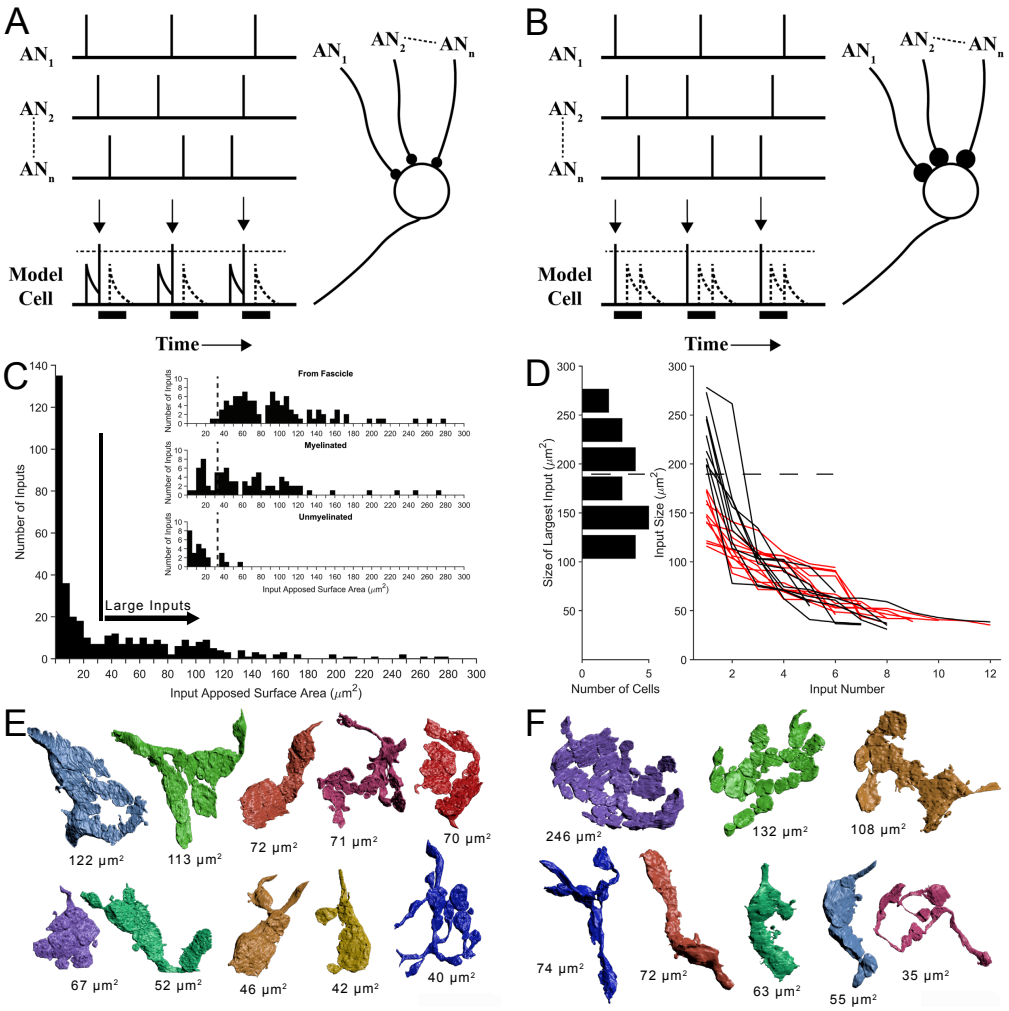

Figure 2. Two competing models for synaptic convergence evaluated using size profiles of endbulb terminals. (**A**) Coincidence Detection model, all inputs are subthreshold (small circles), have similar weight, and at least two inputs are active in a short temporal window to drive a postsynaptic spike. Each vertical bar is a presynaptic spike and each row is a separate auditory nerve (AN) input. Bottom line is activity of postsynaptic globular bushy cell (GBC). EPSPs are solid; action potentials indicated by vertical arrows. Dotted lines are inputs that occur during the refractory period (solid bar). Drawn after ***Joris et al.*** (***1994a***). (**B**) First-Latency model, whereby all inputs are suprathreshold (large circles), have similar weight, and the shortest latency input drives a postsynaptic spike. Longer latency inputs are suppressed during the refractory period. For a periodic sound, both models yield improved phase-locking in the postsynaptic cell relative to their auditory nerve (AN) inputs. (**C**) Histogram of input sizes, measured by apposed surface area (ASA), onto GBC somata. Minimum in histogram (vertical bar) used to define large somatic inputs (arrow). Inset: Top. Size distribution of somatic terminals traced to auditory nerve fibers within the image volume. Middle. Size distribution of somatic terminals with myelinated axons that exited the volume without being traced to parent fibers within volume. Bottom. Size distribution of somatic terminals with unmyelinated axons. Some of these axons may become myelinated outside of the image volume. Small terminals (left of vertical dashed lines) form a subset of all small terminals across a population of 15 GBCs. See Figure 2–***Figure Supplement 1*** for correlations between ASA and soma areas. (**D**) Plot of ASAs for all inputs to each cell, linked by lines and ranked from largest to smallest. Size of largest input onto each cell projected as a histogram onto the ordinate. Dotted line indicates a minimum separating two populations of GBCs. Linked ASAs for GBCs above this minimum are colored black; linked ASAs for GBCs below this minimum are colored red. (**E, F**). All large inputs for two representative cells. View is from postsynaptic cell. (**E**) The largest input is below threshold defined in panel (**D**). See Figure 2–***Figure Supplement 2*** for all 12 cells with this input pattern. (**F**) The largest input is above threshold defined in panel **D**). All other inputs have similar range as the inputs in panel (**E**). See Figure2–***Figure Supplement 3*** for all 9 cells with this input pattern. Scale bar omitted because these are 3D structures with extensive curvature, and most of the terminal would be out of the plane of the scale bar. See Figure 2–***video 1*** to view the somatic inputs on GBC18.

Figure 2–Figure supplement 1. Morphological correlations for synapse and somatic area, related to Figure 2C,D.

Figure 2–Figure supplement 2. Large somatic terminals onto each globular bushy cell (GBC) that fit the Coincidence Detection model, related to Figure 2E.

Figure 2–Figure supplement 3. Large terminals onto each globular bushy cell (GBC) that fit the mixed Coincidence Detection/First-Arrival model, related to Figure 2F.

Figure 2–video 1. Exploration of all features of a globular bushy cell (GBC). This video opens with a full view of GBC18, including its dendrites (red), cell body (beige), axon (pink), and all large somatic inputs (various colors). Note that the proximal dendrite and axon emerge from the same pole of the cell. Two endbulb terminals each extend onto the axon (blue arrows) and proximal dendrite (green arrows). The view pans around the cell body to reveal all somatic inputs and short segments of their axons.

reveals the heterogeneity of input shapes and sizes for each cell and across the cell population (***Figure 2***E,F; Figure 2–***Figure Supplement 2*** and Figure2–***Figure Supplement 3*** show all modified endbulbs for the 21 reconstructed cells). We hypothesized from this structural analysis that one group of GBCs follows the coincidence detection (CD) model depicted in ***Figure 2***A where all inputs are subthreshold (12/21 cells; red lines in ***Figure 2***D), and a second group of GBCs follows a mixed coincidence-detection / latency detector model (mixed-mode, MM) where one or two inputs are suprathreshold and the remainder are subthreshold (9/21 cells; black lines in ***Figure 2***D). No cells strictly matched the latency detector model (all suprathreshold inputs) depicted in ***Figure 2***B.

Innervation of globular bushy cells shows specificity for auditory nerve fiber fascicles

The majority (98/158) of end bulbs could be traced along axon branches to parent ANFs constituting fascicles within the image volume. The remaining branches exited the volume (2/6 and 3/8 branches (white arrowheads), respectively, for example cells in ***Figure 3*** A, B). We then asked whether the fascicle organization of the auditory nerve fibers was related to innervation patterns, whereby most inputs to a particular cell might be associated with the same fascicle. We identified nine fascicles in the image volume, containing in total 1,100 axons (based on a section taken through middle of volume), which is 7-15% of the total number of ANFs in mouse (7,300-16,600) (***Burda et al., 1988***; ***Anniko and Arnesen, 1988***; ***Camarero et al., 2001***). The largest five fascicles (containing between 115 and 260 axons/fascicle) each split into as many as seven sub-fascicles along their trajectory (***Figure 3***A,B). Excluding 4 cells near the edge of the image volume (GBCs 02, 24, 29, 14 plotted at left in right histogram of ***Figure 3***C), 2-9 endbulbs from individual cells were traced to ANFs in the same major fascicle (for the example cells in ***Figure 3***A,B, 2 fascicles each contained 2 parent axons of inputs to each cell (fascicles #2, #3, and #2, #7, respectively)). None of the parent ANFs that were linked to endbulbs branched more than once within the volume. The proportion of axons yielding endbulb terminals within the image volume was low in some fascicles (fasicles #3, #4, #5, #6; fasicle #4 contributed no endbulbs), and high in others (#1, #7; GBC08 had 9 endbulbs traced to fascicle #7). These observations indicate that the auditory nerve fascicles preferentially innervated different rostro-caudal territories of the same frequency region (***Figure 3***D).

The myelinated lengths of branches from parent fibers to terminals varied from 0 (endbulbs emerged *en passant* from parent terminal in two cases) to 133 μm (***Figure 3***G). For a subset of 10 GBCs with at least 4 branches traced back to parent ANFs, we utilized the resolution and advantages of volume EM to assay axon morphology. Branches were thinner than the parent ANFs, (1.4 (SD 0.33) vs 2.7 (SD 0.30) μm diameter), and both the parent ANF and branches had the same g-ratio of fiber (including myelin) to axon diameter (***Figure 3***F; ratio 0.76 across all axons). From these data we applied a conversion of 4.6 * fiber diameter in μm (***Boyd and Kalu, 1979***; ***Waxman and Bennett, 1972***) to the distribution of fiber lengths, yielding a conduction velocity range of 2.3 - 8.9 m/sec, and a delay range of 0 (*en passant* terminal) - 15.9 μs. These values were then scaled by the L/d ratio, where L is the length between the ANF node and the terminal heminode, and d is the axon diameter (***Brill et al., 1977***; ***Waxman, 1980***). The L/d ratio slows conduction velocity to a greater extent in short branches, yielding a latency range of 0–21 μs across the cell population, and a similar range among different branches to individual cells (***Figure 3***G). Such small variations in delays may affect the timing of spikes at sound onset, which can have a standard deviation of 0.39 ms in mouse (***Roos and May, 2012***, measured at 30dB re threshold, so it likely that there is a smaller SD at higher intensity), similar to values in cat (***Young et al., 1988***; ***Blackburn and Sachs, 1989***; ***van Gisbergen et al., 1975***; ***Spirou et al., 1990***) and gerbil (***Typlt et al., 2012***). We conclude, however, that the diameter of ANF branches is sufficiently large to relax the need for accurate branch location and short-range targeting of the cell body in order to achieve temporally precise responses to amplitude-modulated or transient sounds.

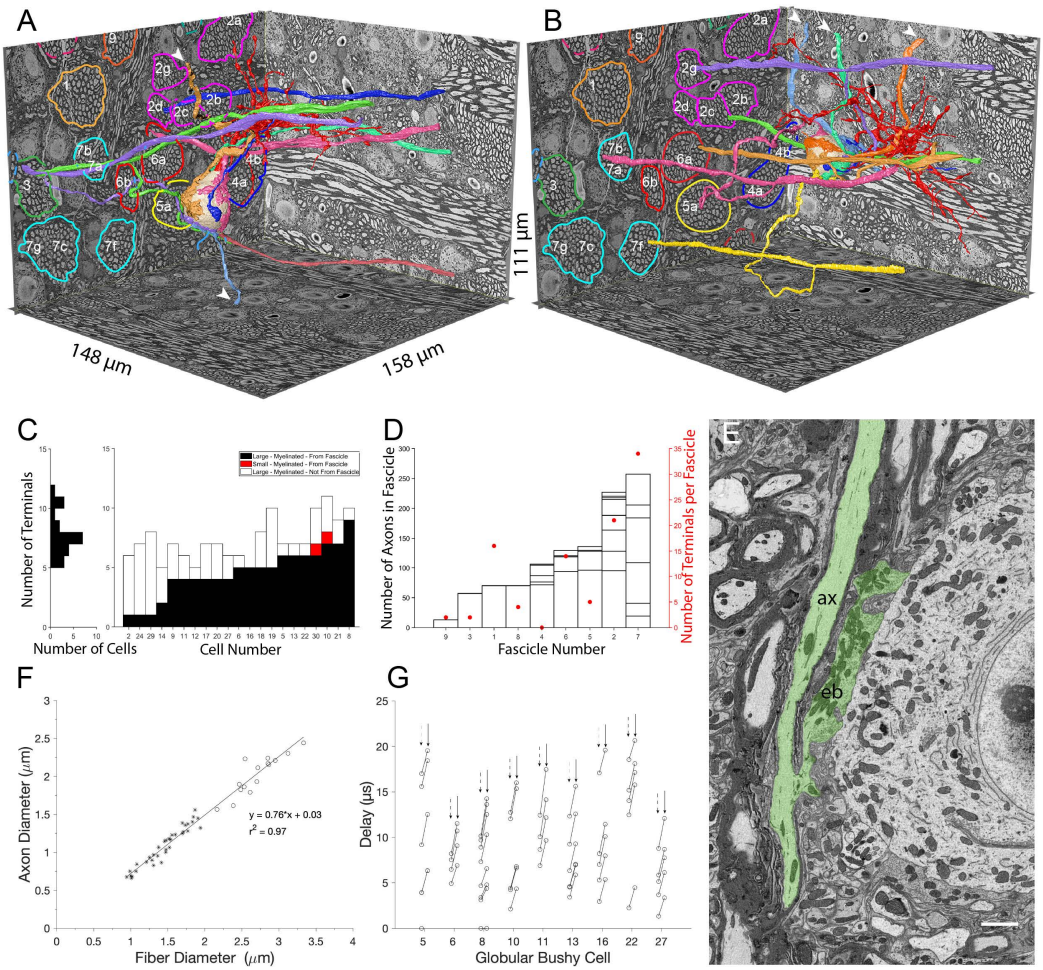

Figure 3. Large somatic terminals link to auditory nerve fibers (ANF) through myelinated branch axons of varying length and fascicle organization. (**A, B**). ANFs and their branches leading to all large inputs for two representative cells. ANF, branch axon and large terminal have same color; each composite structure is a different color. Convergent inputs emerge from multiple fascicles (fascicles circled and named on back left EM wall), but at least two inputs emerge from the same fascicle for each cell (green, purple axons from fascicle 3 in panel (**A**); yellow, mauve axons from fascicle 7 and green, purple from fascicle 2 in panel (**B**)). Some branch axons leave image volume before parent ANF could be identified (white arrowheads). Globular bushy cell (GBC) bodies colored beige, dendrites red, axons mauve and exit volume at back, right EM wall; axon in panel A is evident in this field of view. (**C**) Stacked histogram of branch axons traced to parent ANF (black), branch axons exiting volume without connection to parent ANF (open), small terminals linked to parent ANF (red; included to illustrate these were a minority of endings), arranged by increasing number of large terminals traced to a parent ANF per GBC. GBCs with fewest branch connections to parent ANF (GBC02, 24, 29, 14) were at edge of image volume, so most branch axons could only be traced a short distance. Number of terminals per cell indicated in horizontal histogram at left. (**D**) Number of axons in each fascicle (left ordinate) and number of axons connected to endbulb terminals per fascicle (red symbols, right ordinate). (**E**) Example of *en passant* large terminal emerging directly from node of Ranvier in parent ANF. (**F**) Constant ratio of fiber diameter (axon + myelin) / axon diameter as demonstrated by linear fit to data. All branch fiber diameters (asterisks) were thinner than ANF parent axon diameters (open circles). (**G**) Selected cells for which most branch axons were traced to a parent ANF. Lines link the associated conduction delays from parent ANF branch location for each branch, computed using the individual fiber diameters (length / conduction velocity (leftmost circle, vertical dashed arrows) or values scaled by the axon length / axon diameter (rightmost circle, vertical solid arrow). See Figure 3–***video 1*** for a detailed 3-D view of GBC11 and its inputs.

Figure 3–video 1. Exploration of all large somatic inputs onto a single globular bushy cell (GBC), their branch axons, and parent auditory nerve fibers. This video opens with a full view of GBC11, including its dendrites (red), cell body (beige), axon (pink), all of its large somatic inputs (various colors), and the auditory nerve fibers (ANFs) from which those inputs originate. Somatic inputs and their axon branches, including the parent ANF, share the same color. The view pans around the cell body to show all large terminals, and an axon (cyan) that exited the volume before likely linking to an ANF is indicated by a red arrow. All except two terminals are then removed. The axons of these terminals are traced to branch points from their parent ANFs (magenta arrows). All inputs and their axons are replaced, and a second axon (green) that exits the volume before likely linking to an ANF is indicated (red arrow). The view pans to two ANFs (red and yellow) from the same nerve fascicle, and their branch points (magenta arrows). All other nerve terminals and axons are removed, and the two branch axons are traced to the cell body.

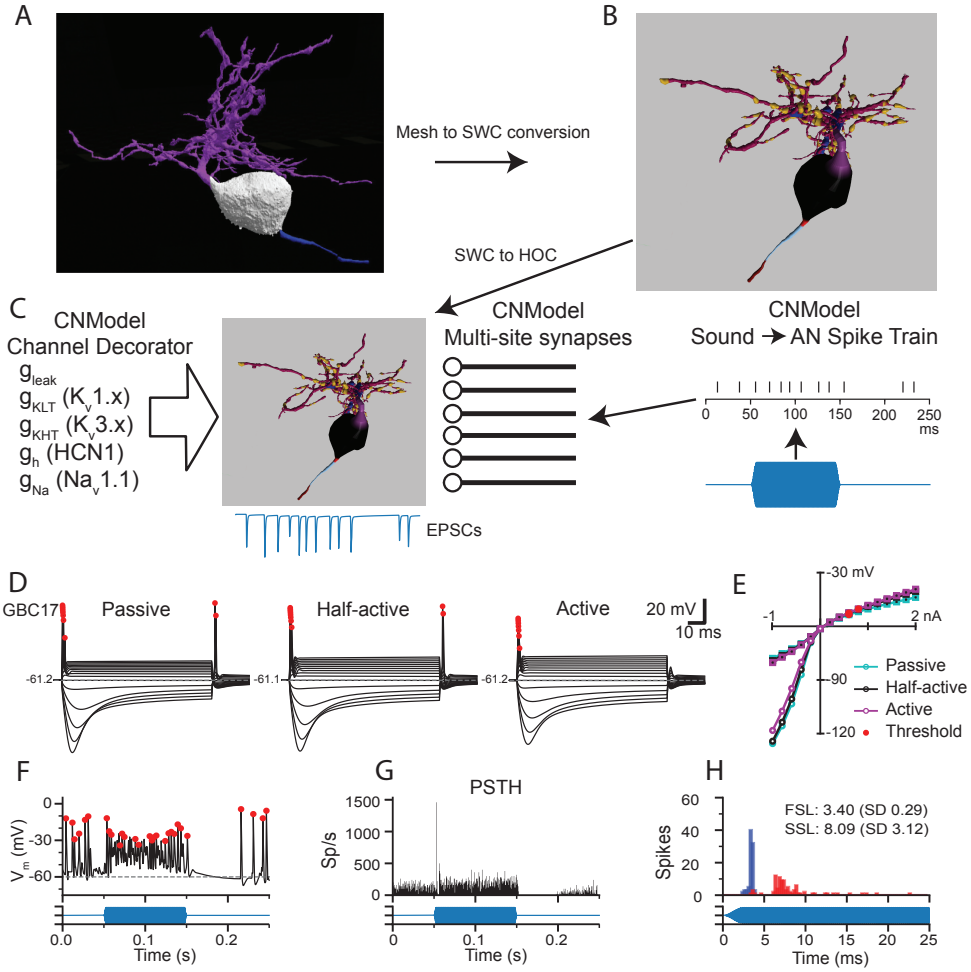

Figure 4. Pipeline to generate compartmental models for analysis of synaptic integration and electrical excitability from the mesh reconstructions of mouse VCN bushy neurons. (**A**) The mesh representation of the volume EM segmentation was traced using syGlass virtual reality software to generate an SWC file consisting of locations, radii, and the identity of cell parts (**B**). In (**B**), the myelinated axon is dark red, the axon initial segment is light blue, the axon hillock is red, the soma is black, the primary dendrite is purple, dendritic hubs are blue, the secondary dendrite is dark magenta, and the swellings are gold. The mesh reconstruction and SWC reconstructions are shown from different viewpoints. See Figure 4–***Figure Supplement 1*** for all reconstructions. See Figure 4–***video 1*** for a 3D view of the mesh and reconstructions for GBC11. (**C**) The resulting SWC model is decorated with ion channels (see Figure 4–***Figure Supplement 2*** for approach), and receives inputs from multi-site synapses scaled by the apposed surface area of each ending. For simulations of auditory nerve input, sounds (blue) are converted to spike trains to drive synaptic release. (**D**). Comparison of responses to current pulses ranging from -1 to + 2 nA for each dendrite decoration scheme. In the Passive scheme, the dendrites contain only leak channels; in the Active scheme, the dendrites are uniformly decorated with the same density of channels as in the soma. In the Half-active scheme, the dendritic channel density is one-half that of the soma. (**E**) Current voltage relationships for the 3 different decoration schemes shown in (**D**). Curves indicated with circles correspond to the peak voltage (exclusive of APs); curves indicated with squares correspond to the steady state voltage during the last 10 ms of the current step. Red circles indicate the AP threshold. (**F**) Example of voltage response to a tone pip in this cell. Action potentials are marked with red dots, and are defined by rate of depolarization and amplitude (see Methods). (**G**) Peri-stimulus time histogram (PSTH) for 50 trials of responses to a 4 kHz 100-ms duration tone burst at 30 dB SPL. The model shows a primary-like with notch response. See Figure 4–***Figure Supplement 4*** for all tone burst responses. (**H**) First spike latency (FSL; blue) and second spike latency (SSL; red) histograms for the responses to the tone pips in **G**. (**F,G,H**) The stimulus timing is indicated in blue, below the traces and histograms.

Figure 4–Figure supplement 1. Segmented globular bushy cells (GBC) and their representations for compartmental modeling, related to Figure 4A and B.

Figure 4–Figure supplement 2. Conductance scaling using voltage clamp simulations for different patterns of dendrite decoration, related to Figure 4C.

Figure 4–Figure supplement 3. Current-clamp responses for all 10 complete bushy cells for each of the ion channel decoration conditions, related to Figure 4D and E.

Figure 4–Figure supplement 4. Peri-stimulus time histograms (PSTH), spike latencies and interpsike interval regularity in response to tone bursts at characteristic frequency, related to Figure 4F-H.

Figure 4–video 1. Comparison of cell structures and regions between a 3D mesh and an SWC representation of a globular bushy cell (GBC). This video opens with a full side-by side views of the GBC11 reconstruction (left), including its dendrites (red), cell body (beige), and axon (pink), and the SWC representation (right) of the same structures. The view then zooms into the cell body and axon, where the transition point from cell body to the axon (yellow arrow), the middle of the unmyelinated initial segment (green arrow), and the transition point where myelination of the axon begins (blue arrow) are indicated. Note that the diameter of the axon increases significantly where it is myelinated. Location of last paranodal loop of myelin is indicated by narrow, peach-colored band to right of the blue arrow on the SWC representation. The view then pans to a dorsolateral view of the cell, where a pink arrow indicates the proximal dendrite, and an orange arrow signifies the primary hub of the cell. The view then pans to a top-down location showing two secondary hubs (orange arrows). The view then shifts to reveal periodic dendrite swellings (three cyan arrows) separated by dendrite shafts (two red arrows). SWC color code: pink, cell body; axon hillock, orange; axon initial segment, light green; myelinated axon, light blue; proximal dendrite, maroon; dendrite hub, greenish-brown; dendrite swelling, cyan; dendrite shaft, gray.

A pipeline for translating high-resolution neuron segmentations into compartmental models consistent with *in vitro* and *in vivo* data

Ten of the GBCs had their dendrites entirely or nearly entirely contained within the image volume, offering an opportunity for high-resolution compartmental modeling. The computational mesh structures of the cell surfaces (Figure1–***Figure Supplement 1***), including the dendrites, cell body, axon hillock, axon initial segment, and myelinated axon were converted to a series of skeletonized nodes and radii (SWC file format (***Cannon et al., 1998***); ***Figure 4***B, right and Figure 4–***Figure Supplement 1*** – mesh and SWC images of all 10 cells) by tracing in 3D virtual reality software (syGlass, IstoVisio, Inc.). The SWC files were in turn translated to the HOC file format for compartmental modeling using NEURON (***Carnevale and Hines, 2006***). The HOC versions of the cells were scaled to maintain the surface areas calculated from the meshes (see Methods). An efficient computational pipeline was constructed that imported cell geometry, populated cellular compartments with ionic conductances, assigned endbulb synaptic inputs accounting for synaptic weights, and simulated the activation of ANFs for arbitrary sounds (see Methods and ***Figure 4***C).

Individual cell models were constructed and adjusted by mimicking *in vitro* measurements for g_{KLT} to set channel densities (see Figure 4–***Figure Supplement 2***). Three models were generated for each cell, varying only in the density of channels in the dendrites. In the "passive" model, the dendrites only had a leak conductance. In the "active" model, the dendrites had the same channel complement and density as the soma. In the "half-active" model, the conductances in the dendrites were set to half of the somatic density. The membrane time constant was slower by nearly a factor of 2 with the passive dendrite parameters than the active dendrite parameters, but the input resistances were very similar across the 3 parameter sets , with no further parameter adjustments. (Figure 4–***Figure Supplement 2***). All 3 parameter sets yielded GBC-like phasic responses to current injection, a voltage sag in response to hyperpolarizing current and a non-linear IV plot (***Figure 4*** D,E and Figure 4–***Figure Supplement 3***). In the passive dendrite models, some cells showed trains of smaller spikes with stronger current injections, or 2-3 spikes with weaker currents (GBCs 09, 10, 11 and 30). Rebound spikes were larger and more frequent with passive dendrites than in the other 2 models. Rebound spikes were present in all cells with the half-active dendrite model, whereas repetitive firing was limited to 2-3 spikes, similar to what has been observed in GBCs previously (***Francis and Manis, 2000***; ***Cao et al., 2007***) The active dendrite models exhibited single-spike phasic responses, and rebound action potentials were suppressed (GBCs 05, 06 and 10) or smaller in amplitude. Because the differences in intrinsic excitability were modest across the models, and because the half-active dendrite model most closely resembled typical responses reported *in vitro*, we used the half-active dendrite models for the remainder of the simulations.

Next, we investigated the responses to simulated sound inputs. For these simulations, the number of synapses in each endbulb was based on the endbulb ASA and the average synapse density (***Figure 1***F). Terminal release was simulated with a stochastic multi-site release model in which each synapse in the terminal operated independently (***Xie and Manis, 2013b***; ***Manis and Campagnola, 2018***). Synaptic conductances were not tuned, but instead calculated based on experimental measurements as described previously (***Manis and Campagnola, 2018***). Action potentials (AP) (marked by red dots in ***Figure 4***D,F) were detected based on amplitude, slope and width at half-height (***Hight and Kalluri, 2016***). ANFs were driven in response to arbitrary sounds via spike trains derived from a cochlear model (***Zilany et al., 2014***; ***Rudnicki et al., 2015***) (***Figure 4***C, right). As expected, these spike trains generated primary-like (Pri) responses in ANFs and yielded Pri or primary-like with notch (Pri-N) responses in the GBC models (***Figure 4***F-G; Figure 4–***Figure Supplement 4***). The predicted SD of the first spike latency in the model varied from 0.232 to 0.404 ms (Figure 4–***Figure Supplement 4***), while the coefficient of variation of interpsike intervals ranged from 0.45 to 0.73. These ranges are similar to values reported for mouse CN *in vivo* (***Roos and May, 2012***). Taken together, these

simulations, which were based primarily on previous electrophysiological measurements and the volume EM reconstructions, without further adjustments, produced responses that are quantitatively well-matched with the limited published data. Using these models, we next explored the predicted contributions of different sized inputs and morphological features to spike generation and temporal coding in GBCs.

Model Predictions

The individual GBCs showed variation in the patterns of endbulb size, dendrite area and axon initial segment length. In this section, we examine the model predictions for each of the fully reconstructed GBCs to address five groups of predictions about synaptic integration and temporal precision in GBCs.

Prediction 1: Endbulb size does not strictly predict synaptic efficacy

The wide variation in size of the endbulb inputs (***Figure 2***C-F) suggests that inputs with a range of synaptic strengths converge onto the GBCs. We then inquired whether individual cells followed the coincidence-detection or mixed-mode models hypothesized by input sizes shown in ***Figure 2***D. To address this question, we first modeled the responses by each of the 10 fully reconstructed GBCs as their endbulb inputs were individually activated by spontaneous activity or 30 dB SPL, 16 kHz tones (responses at 30dB SPL for four representative cells (GBC05, 30, 09, and 17 are shown in ***Figure 5***A; the remaining GBCs are shown in Figure 5–***Figure Supplement 1***). In ***Figure 5***A, voltage responses to individual inputs are rank-ordered from largest (1) to smallest (7,8,or 9) for each cell. Without specific knowledge of the spontaneous rate or a justifiable morphological proxy measure, we modeled all ANFs as having high spontaneous rates since this group delivers the most contacts to GBCs in cat (Fig.9 in ***Liberman, 1991***).

We chose four cells to illustrate the range of model responses. GBC05 and GBC30 (***Figure 5***A1, A2) fit the coincidence-detection model, in that none of their inputs individually drove postsynaptic APs except the largest input for GBC30, which did so with very low efficacy (#postsynaptic APs/#presynaptic APs; see also GBC10, GBC06, GBC02, GBC13 in Figure 4 Supplement 1). GBC09 and GBC17 (***Figure 5***A3, A4) fit the mixed-model, in that the largest inputs (2 large inputs for GBC17) individually drive APs with high efficacy (see also GBC11, GBC18 in Figure 4–***Figure Supplement 1***). This result demonstrates two populations of GBCs based on the absence or presence of high efficacy suprathreshold inputs.

The second largest input for GBC09 (132 μm^2) had higher efficacy than the largest input for GBC30 (172 μm^2). The variation of efficacy for similar ASA was evident, especially between 125-175 μm^2, in a plot of all inputs across the ten GBCs (***Figure 5***D). Since many cells lacked inputs in this range, we created 3 different sizes of artificial synapses (150, 190 and 230 μm^2) onto GBCs 10, 17 and 30 to predict the efficacy of a more complete range of input sizes. The addition of these inputs (stars colored for each cell) reinforced the suggestion that there were two populations of GBCs, of greater (GBCs 09, 11, 17; red curve) or lesser excitability (GBCs 02, 05, 06, 10, 13, 18, 30; cyan curve). Therefore, we combined all synapses (excluding the artificial synapses) from GBCs 09, 11, and 17 into one group, and synapses from all the remaining cells, GBCs 02, 05, 06, 10, 13, 18 and 30, into a second group. GBC18 was included in the lesser excitability group event though it had a single large input, because all of its smaller inputs grouped with the input efficacy for the other cells with lower excitability. We then confirmed the efficacy data by fitting each group with logistic functions with distinct parameters (***Figure 5***D). The group with the greater excitability had half-maximal size for input ASAs of 148.6 (SD 1.1) μm^2 and a maximal efficacy of 0.72 (SD 0.01) μm^2, with a slope factor of 14.3 (SD 1.1)/ μm^2. The fit to the group with lesser excitability (***Figure 5***D, light blue line) yielded a half-maximal size of 204.3 (SD 4.7) μm^2, and with a slope factor of 19.8 (SD 2.2)/ μm^2. Cells with lesser and greater excitability were found in both the coincidence-detection (lesser: GBC02, 05,

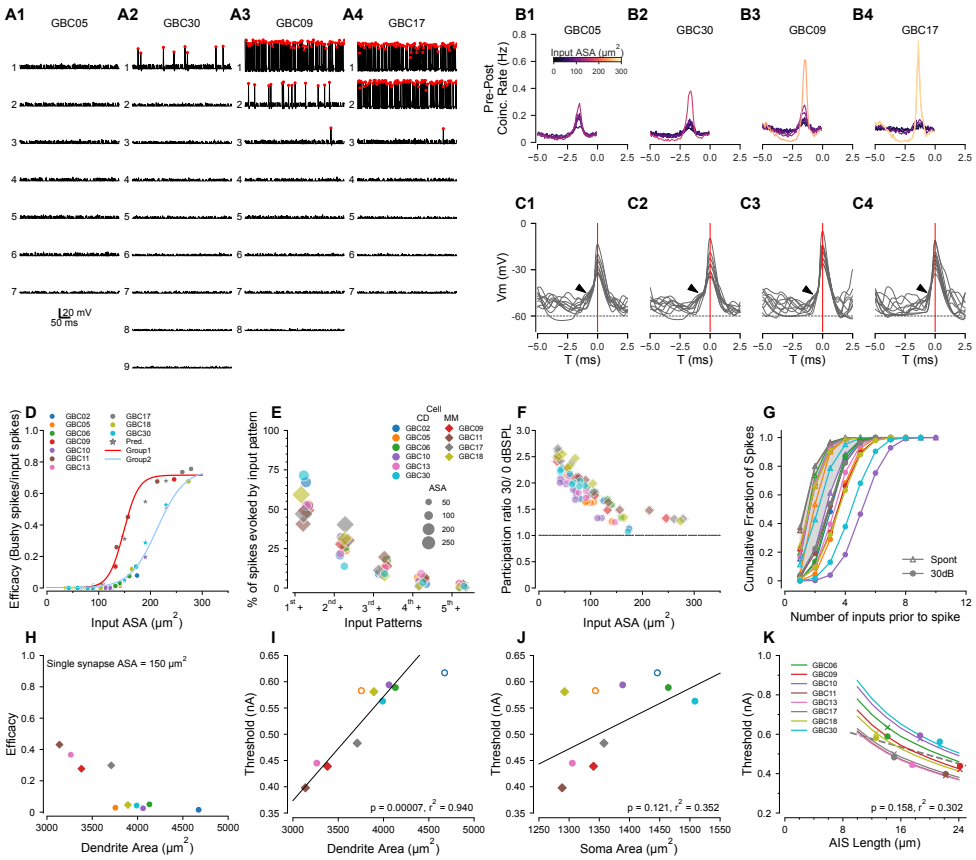

Figure 5. Compartmental models predict sub- and suprathreshold inputs, efficacy dependence on dendrite surface area, and rate-dependent participation in spike generation. (**A1-4**) Simulations showing EPSPs and spikes in response to individual ANFs in 4 model globular busjy cells (GBCs) during a 30 dB SPL tone pip, arranged by efficacy of the largest input. Spikes indicated by red dots. Vertically, traces are ranked ordered by endbulb size. Responses for the other 6 cells are shown in Figure 5–***Figure Supplement 1***. (**B1-4**) Cross-correlations between postsynaptic spikes and spikes from each input ANF during responses to 30 dB SPL tones (all inputs active). Trace colors correspond to the ASA of each input (color bar in (**B1**)). See Figure 5–***Figure Supplement 1*** for cross-correlations for the other 6 cells. (**C1-4**): Voltage traces aligned on the spike peaks for each of the 4 cells in (**B**). Postsynaptic spikes without another spike within the preceding 5 ms were selected to show the subthreshold voltage trajectory more clearly. Zero time (0 ms; indicated by vertical red line) is aligned at the action potential (AP) peak and corresponds to the 0 time in (**B1-4**). Arrowheads indicate EPSPs preceding the SP in panels (**C1-3**); arrowhead in **C4** shows APs emerging directly from the baseline, indicating suprathreshold inputs. (**D**) GBCs could be divided into two groups based on the pattern of efficacy growth with input size. GBCs 09, 11, and 17 formed one group, and GBCs 02, 05, 06, 10, 13 18, and 30 formed a second group with overall lower efficacy. The red line is a best fit logistic function to the higher efficacy group. The blue dashed line is the logistic fit to the lower efficacy group. Stars indicate test ASA-efficacy points, supporting membership in the lower efficacy group for cells 10 and 30. Although GBC13 had a single large input, its smaller AN inputs grouped with the lower efficacy group. (**E**) Comparison of the patterns of individual inputs that generate spikes. Ordinate: 1st+ indicates spikes driven by the largest input plus any other inputs. 2nd+ indicates spikes driven by the second largest input plus any smaller inputs, excluding spikes in which the largest input was active. 3rd+ indicates spikes driven by the third largest input plus any smaller inputs, but not the first and second largest inputs. 4th+ indicates contributions from the fourth largest input plus any smaller inputs, but not the 3 largest. 5th+ indicates contributions from the fifth largest input plus any smaller inputs, but not the 4 largest. Colors and symbols are coded to individual cells, here grouped according to predicted coincidence mode or mixed-mode input patterns as shown in Figure2–***Figure Supplement 2*** and Figure2–***Figure Supplement 3***). See Figure 5–***Figure Supplement 2*** for a additional summaries of spikes driven by different input patterns. (**F**) The participation of weaker inputs (smaller terminal area) is increased during driven activity at 30 dB SPL relative to participation during spontaneous activity. The dashed line indicates equal participation at the two levels. Each input is plotted separately. Colors and symbols are coded to individual cells as in (**D**). (**G**) Cumulative distribution of the number of inputs driving postsynaptic spikes during spontaneous activity and at 30 dB SPL. The color for each cell is the same as in the legend in (**D**). Symbols correspond to the stimulus condition. (**H**) Efficacy for a single 150 μm^2 input is inversely related to dendrite surface area. (**I**) Dendrite area and action potential threshold are highly correlated. Open circles (GBC02 and GBC05) indicate thresholds calculated using the average AIS length, but are not included in the regression. Colors and symbols as in (**D**). **J** Soma area and action potential threshold are not well correlated. Open symbols are as in (**I**). (**K**) Variation of AIS length using the averaged axon morphology reveals an inverse relationship to spike threshold for all cells (lines). Crosses indicate thresholds interpolated onto the lines for the averaged axon simulations; circles indicate thresholds measured in each cell with their own axon. Cells GBC02 and GBC05 are omitted because AIS length is not known. Across the cell population, the thresholds are only weakly correlated with AIS length (linear regression indicated by dashed grey line). Colors as in (**E**).

Figure 5–Figure supplement 1. Cross-correlation plots for 6 additional modeled cells, related to Figure 5A-C.

Figure 5–Figure supplement 2. Contributions of different input patterns to postsynaptic spiking, related to Figure 5E.

06, 10 30; greater: GBC13) and mixed-mode (lesser: GBC18; greater GBC09, 11, 17) categories described above. Additional factors that affect excitability are discussed below in connection with Predcitions 3 and 4.

Prediction 2: Mixed-mode cells operate in both latency and coincidence-detection modes when all inputs are active.

The predicted grouping of cells according to synaptic efficacy of individual inputs raises the question of how these cells respond when all inputs are active. In particular, given the range of synapse sizes and weights, we considered the contribution of the smaller versus larger inputs even within coincidence detection size profiles. To address this question, we computed GBC responses when all ANFs to a model cell were driven at 30dB SPL and active at the same average rate of 200 Hz. We then calculated the cross-correlation between the postsynaptic spikes and each individual input occurring within a narrow time window before each spike.. These simulations and cross-correlations are summarized in ***Figure 5***B-C, for the 4 cells shown in ***Figure 5***A, and in Figure 5–***Figure Supplement 1*** for the other 6 cells.

For GBC05 and GBC30, which had no suprathreshold inputs, all inputs had low coincidence rates. However, not all inputs had equal contribution in that the largest input had a rate 3-4 times the rate of the smallest input ***Figure 5***B1, B2). In both cells the requirement to integrate multiple inputs was evident in voltage traces exhibiting EPSPs preceding an AP (***Figure 5***C1, C2). GBC09 and GBC17 illustrate responses when cells have one or two secure suprathreshold inputs, respectively (***Figure 5***A3, A4). The cross-correlation plots reveal the dominance of high probability suprathreshold inputs in generating APs in GBCs (yellow traces for GBC09, 17). For GBC09 but not GBC17 (likely because GBC17 has two suprathreshold inputs), all subthreshold inputs had appreciable coincidence rates. The summation of inputs to generate many of the APs for GBC09 is seen in the voltage traces preceding spikes, but most APs for GBC17 emerge rapidly without a clear preceding EPSP (***Figure 5***C3, C4, respectively).

To understand how weaker inputs contributed independently of the largest inputs, we also calculated the fraction of postsynaptic spikes that were generated without the participation of simultaneous spikes from the N larger inputs (where N varied from 1 to number of inputs - 1, thus successively peeling away spikes generated by the larger inputs). We focused initially on mixed-mode cells (***Figure 5***E). We first calculated the fraction of postsynaptic spikes generated by the largest input in any combination with other inputs (in the time window -2.7 to -0.5 ms relative to the spike peak as in ***Figure 5***B). This fraction ranged from 40-60% in mixed-mode cells (hexagons, $1^{st}+$ in ***Figure 4***E). The fraction of postsynaptic spikes generated by the second-largest input in any combination with other smaller inputs was surprisingly large, ranging from 25-30% (excluding GBC17 which had 2 suprathreshold inputs; $2^{nd}+$ in ***Figure 5***E). Notably, all combinations of inputs including the 3rd largest and other smaller inputs accounted for about 25% of all postsynaptic spikes. Thus, a significant fraction (about 50%) of postsynaptic spikes in mixed-mode cells are predicted to be generated by various combinations of subthreshold inputs operating in coincidence detection mode.

For GBCs that are predicted to operate in the coincidence-detection mode, we hypothesized that the contributions of different sized inputs would be more uniform. We tested this using tone stimuli at 30dB SPL. Surprisingly, in two of the cells with the largest inputs (GBC02, GBC30), the largest input in combination with all of the smaller inputs (circles, $1^{st}+$ in ***Figure 5***E) accounted for a larger percentage of postsynaptic spikes than in any of the mixed-mode cells. Notably, the largest inputs for these two cells could individually drive postsynaptic spikes, but at very low efficacy. Across the remaining cells, the $1^{st}+$ category accounted for about 50% of all postsynaptic spikes similar to the mixed model cells. These simulations thus predict that, even among coincidence detection profiles, the contributions by individual endbulbs to activity vary greatly, whereby

larger inputs can have a disproportional influence that equals or exceeds that of suprathreshold inputs in mixed-mode cells.

We next inquired whether the participation of weak inputs in AP generation depended on stimulus intensity (spontaneous activity at 0 dB SPL and driven activity at 30 dB SPL), or was normalized by the increase in postsynaptic firing rate. To address this question, we computed a participation metric for each endbulb as #postsynaptic APs for which a presynaptic AP from a given input occurred in the integration window (-2.7 to -0.5 ms relative to the spike peak), divided by the total number of #postsynaptic APs. The smaller inputs have a higher relative participation at 30 dB SPL than larger inputs (***Figure 5***F), suggesting a rate-based increase in coincidence among weaker inputs at higher intensities. This level-dependent role of smaller inputs was also explored in cumulative probability plots of the number of inputs active prior to a spike between spontaneous and sound-driven ANFs. During spontaneous activity, often only one or two inputs were active prior an AP (***Figure 4***G, triangles). However, during tone-driven activity postsynaptic spikes were, on average, preceded by coincidence of more inputs (***Figure 5***G, filled circles). This leads to the prediction that mixed-mode cells depend on the average afferent firing rates of the individual inputs (sound level dependent), and the specific distribution of input strengths. Furthermore, GBCs operating in the coincidence-detection mode show a similar participation bias toward their largest inputs.

Prediction 3: Dendrite surface area is an important determinant of globular bushy cell excitability

Although the synaptic ASA distribution plays a critical role in how spikes are generated, the response to synaptic input also depends on postsynaptic electronic structure, which determines the patterns of synaptic and ion channel-initiated current flow across the entire membrane of the cell. To further clarify how differences in excitability depend on the cell morphology, we examined the relationship between somatic and dendritic surface areas, and cellular excitability. The GBC dendrite surface area spanned a broad range from $3000 - 4500\ \mu m^2$. Interestingly, the GBCs having the smallest dendrite surface area comprised the group with the greatest excitability as measured by current threshold and the efficacy of a standardized $150\ \mu^2$ input (***Figure 5***H), predicting an important mechanism by which GBCs can modulate their excitability. The large difference in excitability between GBC17 and GBC05 (***Figure 5***H), which have similar surface areas, indicates that other mechanisms, perhaps related to dendritic branch patterns, are needed to explain these data fully.

To explore contributions of cell geometry to synaptic efficacy, we plotted threshold as a function of compartment surface area or length. Threshold was highly correlated with dendrite surface area ($p < 0.001, r^2 = 0.94$, ***Figure 5***I), but modestly correlated with soma surface area ($p = 0.121, r^2 = 0.352$, ***Figure 5***J) or the ratio of dendrite to soma surface areas ($p = 0.046, r^2 = 0.511$. Taken together, these simulations predict that dendrite surface area is a stronger determinant of excitability than soma surface area and that excitability is not correlated with innervation category (coincidence detection or mixed mode), under the assumption that ion channel densities are constant across cells.

Prediction 4: Axon initial segment length modulates globular bushy cell excitability

Another factor that can regulate excitability is the length of the AIS. Therefore, in the EM volume we also quantified the lengths of the axon hillock, defined as the taper of the cell body into the axon, and the axon initial segment (AIS), defined as the axon segment between the hillock and first myelin heminode. The axon hillock was short (2.3 (SD 0.9) μm; measured in all 21 GBCs with reconstructed endbulbs). The AIS length averaged 16.8 (SD 6.3) μm (range 14.2–21.4 μm; n = 16, the remaining five axons exited the volume before becoming myelinated) and was thinner than the myelinated axon. Because the conductance density of Na^+ channels was modeled as constant

across cells, the AIS length potentially emerges as a parameter affecting excitability. To characterize this relationship, in the 10 GBCs used for compartmental modeling, we replaced the individual axons with the population averaged axon hillock and initial myelinated axon, and systematically varied AIS length. Indeed, for each cell the threshold to a somatic current pulse decreased by nearly 40% with increasing AIS length across the measured range of values (***Figure 5***K). Although threshold varied by cell, the current threshold and AIS length were not significantly correlated ($p = 0.158, r^2 = 0.302$, ***Figure 5***K). These simulations predict that AIS length and dendrite area together serve as mechanisms to tune excitability across the GBC population, although dendrite area appears to have a greater contribution.

In 20 of 21 cells for which all large inputs were reconstructed, at least one endbulb terminal (range 1-4) extended onto the axon (hillock and/or the AIS), contacting an average of 18.5 (SD 10) μm^2 of the axonal surface (range 0.7–35.2μm^2). The combined hillock/initial segment of every cell was also innervated by 11.8 (SD 5.6) smaller terminals (range 4 – 22; n = 16). These innervation features will be further explored once the excitatory and inhibitory nature of the inputs, and the SR of endbulb terminals are better understood.

Prediction 5: Temporal precision of globular bushy cells varies by distribution of endbulb size

Auditory neurons can exhibit precisely-timed spikes in response to different features of sounds. Mice can encode temporal fine structure for pure tones at frequencies only as low as 1 kHz, although with VS values comparable to larger rodents such as guinea pigs (***Taberner and Liberman, 2005***; ***Palmer and Russell, 1986***)). However, they do have both behavioral (***Cai and Dent, 2020***) and physiological (***Kopp-Scheinpflug et al., 2003***; ***Walton et al., 2002***) sensitivity to sinusoidal amplitude modulation (SAM) in the range from 10-1000 Hz on higher-frequency carriers. As amplitude modulation is an important temporal auditory cue in both communication and environmental sounds, we used SAM to assess the temporal precision of GBC spiking which has been reported to exceed that of ANFs (***Joris et al., 1994a***; ***Louage et al., 2005***; ***Frisina et al., 1990***). Because temporal precision also exists for transient stimuli, we additionally used click trains. Given the variation of mixed-mode and coincidence-detection convergence motifs across GBCs, we hypothesized that their temporal precision would differ across frequency and in relation to ANFs. The left columns of ***Figure 6*** illustrate the flexibility of our modeling pipeline to generate and analyze responses to arbitrary complex sounds in order to test this hypothesis. SAM tones were presented with varying modulation frequency and a carrier frequency of 16 kHz at 15 and 30 dB SPL (see Figure 6–***Figure Supplement 1*** for comparison of SAM responses in ANFs and a simple GBC model used to select these intensities), and 60Hz click trains were presented at 30 dB SPL. We implemented a standard measure of temporal fidelity (vector strength) for SAM stimuli. To analyze temporal precision of click trains, we used the less commonly employed shuffled autocorrelogram (SAC) metric, which removes potential contribution of the AP refractory period to temporal measures (***Louage et al., 2004***).

Here, we illustrate a representative range of cellular responses and analytics available in our pipeline, from intracellular voltage traces (***Figure 6***A, H) recorded in any cellular compartment (cell body depicted here), to event data with associated representations as raster plots and period histograms. GBCs exhibited a more temporally-constrained distribution of GBC spikes in response to SAM tones and click trains (***Figure 6***B-F, I-M, respectively, shown for GBC17) relative to ANFs. Measures of temporal precision demonstrate an improvement between ANFs and GBC responses to SAM tones (higher VS in ***Figure 6***F). The responses to clicks consist of well-timed spikes, followed by a short refractory period before the ANF spontaneous activity recovers and drives the cell (***Figure 6***J, L). The precision of responses to clicks is also better (narrower SAC half-width) in the GBCs than in their ANF inputs (***Figure 6***M). We then compared responses of GBCs to ANFs across a range

of modulation frequencies from 50 - 1000 Hz at 15 dB SPL, which revealed the tuning of GBCs to SAM tones. GBCs had higher VS at low modulation frequencies (< 300 Hz), and lower VS at higher modulation frequencies (> 300 Hz). Responses varied by convergence motif, whereby coincidence-detection GBCs had enhanced VS relative to ANFs at 100 and 200 Hz (***Figure 6***O1-O2, GBC02 and GBC30), but mixed-mode GBCs only at 200 Hz (***Figure 6*** O3-O4, GBC09 and GBC17).

We explored the tuning of GBCs innervated by mixed mode and coincidence detection input profiles to the modulation frequency of SAM tones by manipulating the activation of endbulbs for each cell. At a modulation frequency of 100 Hz, inputs were dispersed in time so that combinations of small inputs and suprathreshold inputs could generate spikes at different phases of modulation. We hypothesized that removing the largest input and, for GBC17, the two largest inputs, would convert mixed mode into coincidence detection profiles. Indeed, this modification improved VS at 50 and 100 Hz, and the tuning profile broadened to resemble the coincidence detection GBCs (green, purple traces in ***Figure 6*** O3-4). The same manipulation of removing the largest input for coincidence detection cells did not change their tuning, except for a small increase in VS at the lowest modulation frequency (50 Hz). Conversely, we hypothesized that removing all inputs except the largest input for mixed mode cells would make the GBCs more similar to ANFs, because they could follow only the single suprathreshold input. In this single input configuration, VS decreased at low modulation frequency and increased at high modulation frequency, making the tuning more similar to ANFs (orange traces in ***Figure 6*** O3-4). A similar manipulation for coincidence detection input profiles, in which the largest input was able to drive postsynaptic spikes only with low probability (largest inputs of the other coincidence detection neurons did not drive spikes in their GBC), decreased the VS at 100 and 200 Hz, but also decreased VS for modulation frequencies $\geq$ 300 Hz. The consistency across cells of changes in modulation sensitivity with these manipulations can also be appreciated across all cells as plotted in ***Figure 6***P1,P2.

We also computed the rate modulation transfer functions (rMTF) for each input configuration (insets in ***Figure 6*** O1-4 and Figure 6–***Figure Supplement 2*** A-F). For coincidence-detection neurons these functions have a band-pass shape, peaking at 200-300 Hz for configurations with all inputs and configurations lacking the largest input. On the other hand, the largest input alone results in low firing rates. For mixed-mode cells, the rMTF is more strongly bandpass and has a higher rate with all inputs, or all inputs except the largest, whereas the rates are lower and the bandpass characteristic is less pronounced with the largest input alone.

Entrainment, the ability of a cell to spike on each stimulus cycle (see Methods for calculation), was predicted to be better than entrainment in the ANFs up to about 300 Hz (Figure 6–***Figure Supplement 3***A,B) for all GBCs with all inputs for the coincidence-detection neurons. Entrainment dropped to low values at 500 Hz and above. Entrainment for mixed-mode cells exceed values coincidence-detection cells, and nearly equal to ANFs up to 200 Hz (Figure 6–***Figure Supplement 3***C,D). Entrainment was exceeded values for the ANF for all cells up to 200 Hz in the absence of the largest input (Figure 6–***Figure Supplement 3***E,F).

Similarly, improvements in temporal precision were evident in response to click trains Figure 6–***Figure Supplement 4***. The half-widths of the SACs (when there were sufficient spikes for the computation) were consistently narrower and had higher correlation indices when all inputs, or all but the largest input were active than when only the largest input was active. The coincidence-detection GBCs showed the highest correlation indices and slightly narrower half-width (Figure 6–***Figure Supplement 4***). Taken together, the different convergence motifs yielded a range of tuning (mixed-mode GBCs more tuned) to the modulation frequency of SAM tones in comparison to ANFs. Notably, the mixed-mode GBCs with the most pronounced tuning were those whose inputs most easily excited their postsynaptic GBC (***Figure 5***), because their response at 100 Hz was similar to that of ANFs. Thus, the ANF convergence patterns play an important role in setting the temporal precision of individual GBCs.

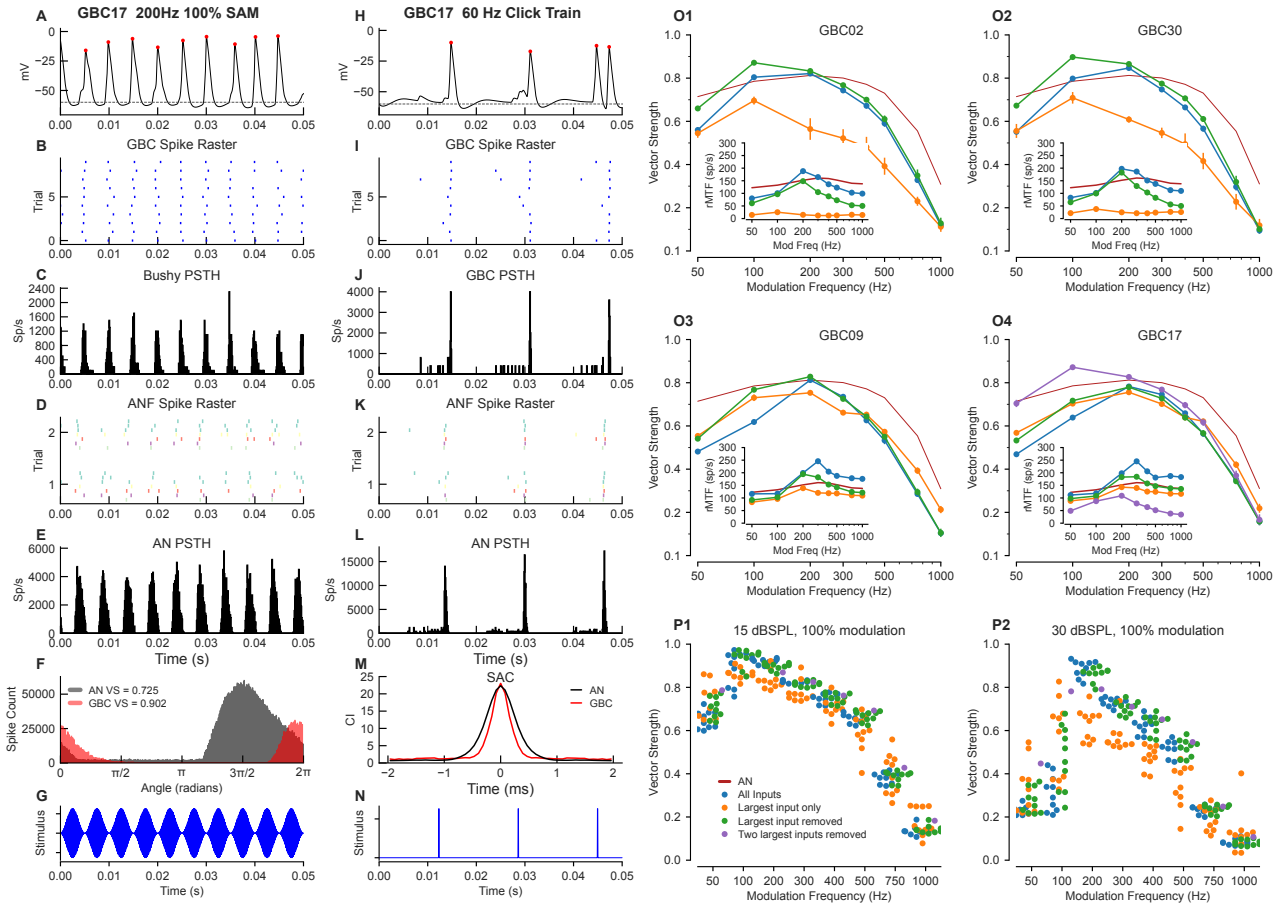

Figure 6. Temporal and rate modulation transfer functions and entrainment to clicks can exceed ANF values and differ between coincidence detection and mixed mode cells. Left column (**A-G**): Example of entrainment to 100% modulated SAM at 200 Hz, at 15 dB SPL. The sound level was chosen to be near the maximum for phase locking to the envelope in ANFs (see Figure 6–***Figure Supplement 1***). (**A**) Voltage showing spiking during a 150 ms window starting 300 ms into a 1-second long stimulus. (**B**) Spike raster for 100 trials shows precise firing. (**C**) PSTH for the spike raster in (**B**). (**D**) Spike raster for all ANF inputs across a subset of 5 trials. Inputs are color coded by ASA. (**E**) PSTH for the ANF. (**F**) Superimposition of the phase histograms for the GBC (black) and all of its ANF inputs (red). (**G**) Stimulus waveform. Center column (**H-N**): responses to a 50 Hz click train at 30 dB SPL. (**H**) GBC membrane potential. (**I**) Raster plot of spikes across 25 trials. (**J**) PSTH showing spike times from I. (**K**) ANF spike raster shows the ANFs responding to the clicks. (**L**) PSTH of ANF firing. (**M**) The shuffled autocorrelation index shows that temporal precision is greater (smaller half-width) in the GBC than in the ANs. See Figure 6–***Figure Supplement 4*** for SAC analysis of other cells. (**N**) Click stimulus waveform. Right column (**O-P**): Summary plots of vector strength. (**O1-4**) Vector strength as a function of modulation frequency at 15 dB SPL for 3 (4 for GBC17) different input configurations. Vertical lines indicate the SD of the VS computed as described in the Methods. Insets show the rate modulation transfer function (rMTF) for each of the input configurations. Red line: average ANF VS and rMTF(insets). See Figure 6–***Figure Supplement 2*** for the other cells. Figure 6–***Figure Supplement 3*** shows spike entrainment, another measure of temporal processing. The legend in (**P1**) applies to all panels in (**O**) and (**P**). (**P**) Scatter plot across all cells showing VS as a function of modulation frequency for 3 (4 for GBC17) different input configurations. (**P1**) VS at 15 dB SPL. (**P2**) VS at 30 dB SPL.

Figure 6–Figure supplement 1. Spike synchronization to stimulus envelope as a function of average stimulus intensity in ANF inputs, related to Figure 6F, P1 and P2.

Figure 6–Figure supplement 2. Vector strength of the 6 other globular bushy cells (GBCs) in response to 100% SAM tones at frequencies from 50 to 1000 Hz on a 16kHz carrier at 15 dB SPL, related to Figure 6O1-4.

Figure 6–Figure supplement 3. Spike entrainment across all globular bushy cells (GBCs) at 15 and 30 dB SPL when different combinations of inputs are active, related to Figure 6P1-2.

Figure 6–Figure supplement 4. Shuffled autocorrelations (SACs) in response to click trains show importance of weaker inputs in improving temporal precision, related to Figure 6M.

GIbular bushy cell dendrites exhibit non-canonical branching patterns and high-degree branching nodes

GBC dendrites have been noted to have dense branching such that they elude accurate reconstruction using light microscopy (***Lorente de Nó, 1981***). Volume EM permitted full and accurate reconstructions, which revealed novel features. Of the 26 GBCs, 24 extended a single proximal dendrite (although one dendrite branched after 1.8 µm), and 2 extended two proximal dendrites. Proximal dendrite length was measured for 22/26 GBCs (proximal dendrites of remaining 4 cells exited image volume), and could reach up to 20 μm (range 3.2 – 19.6 μm; 12.9 (SD 6.2) μm) from the cell body. We used the ten GBCs with complete or nearly complete dendrite segmentations to compute additional summary metrics of dendrite structure. Branches often occurred at near-perpendicular or obtuse angles Nearly all dendritic trees exhibited regions where branches extended alongside one another and could exhibit braiding, whereby branches of the same or different parent branches intertwined, displaying a pattern perhaps unique to mammalian neurons. Dendrites were partitioned qualitatively into categories of little (n = 3), moderate (n = 4) and dense (n = 3) local branching and braiding (***Figure 7***A-C, respectively). EM images reveal the complexity of braided branches and frequent direct contact between them (***Figure 7***D-F, I).

Proximal dendrites expanded into a structure from which at least 2 and up to 14 branches extend (7.0 SD (3.8), n = 10). We name these structures hubs, due to their high node connectivity (7 branches visible in ***Figure 7***G). Secondary hubs were positioned throughout the dendritic tree (***Figure 7***H). One-half (11/22 GBCs) of primary, and some secondary hubs contained a core of filaments that extended through the middle of the structure. This filamentous core was in contact with multiple mitochondria oriented along its axis (***Figure 7***J; and Figure 7–***Figure Supplement 1***), and was also found in a thickened region of a second order dendrite of one of the two large MCs. Dendrites, as noted previously, have many swellings (***Figure 7***H) along higher order branches. Swellings were more numerous than (range 51-126, mean = 74.9 (SD 26.8)), and did not correlate with the number of hubs ($r^2 < 0.001$; Fig. 6H). In rank order, dendrite surface area was comprised of dendritic shafts (58%), swellings (28%), hubs (10%) and the proximal dendrite (4%). (***Figure 7***K).

A complete map of synaptic inputs reveals dendrite branches that lack innervation

We report here the first map for locations of all synaptic terminals onto soma, dendrites and axon of a GBC (GBC09; ***Figure 8***A,B). In addition to 8 endbulb inputs from ANFs, 97 small terminals contacted the cell body. Together these inputs covered 83% of its somatic surface (***Figure 8***C, D). This neuron had 224 inputs across all dendritic compartments (shaft, swelling, hub, proximal dendrite) (***Figure 8***H). Dendritic and small somatic terminals were typically bouton-sized, contained one or two synaptic sites, and could be linked by small caliber axonal segments to other small terminals across the dendrite and/or soma (***Figure 8***A) (cyan arrowheads in ***Figure 8***A′, C). Previous investigation suggested swellings as preferred sites for innervation (***Ostapoff and Morest, 1991***). However, in our reconstruction, innervation density was similar across most compartments (hubs, 10.4/100 μm^2; swellings, 9.3/100 μm^2; shafts 9.1/100 μm^2), and greatest on the proximal dendrite (24/100 μm^2; ***Figure 8***A, E, G, H). At least one endbulb (typically 1 but up to 3) on nearly all GBCs (20/21) extended onto the proximal dendrite (mean = 14.5% of endbulb ASA; black arrow in ***Figure 8***A′). Two endbulbs extended onto axonal compartments of GBC09, indicating that this cell is not exceptional. Somatic endbulbs infrequently (8/159 terminals) innervated an adjacent dendrite of a different GBC.

Notably, entire dendrite branches could be devoid of innervation (black arrows in ***Figure 8***B), and instead were wrapped by glial cells, or extended into bundles of myelinated axons (***Figure 8***F). Even though they are not innervated, these branches will affect the passive electrical properties of the cell by adding surface area. We inquired whether these dendrites constitute sufficient surface area and are strategically located to affect excitability of the cell, by generating a model of GBC09

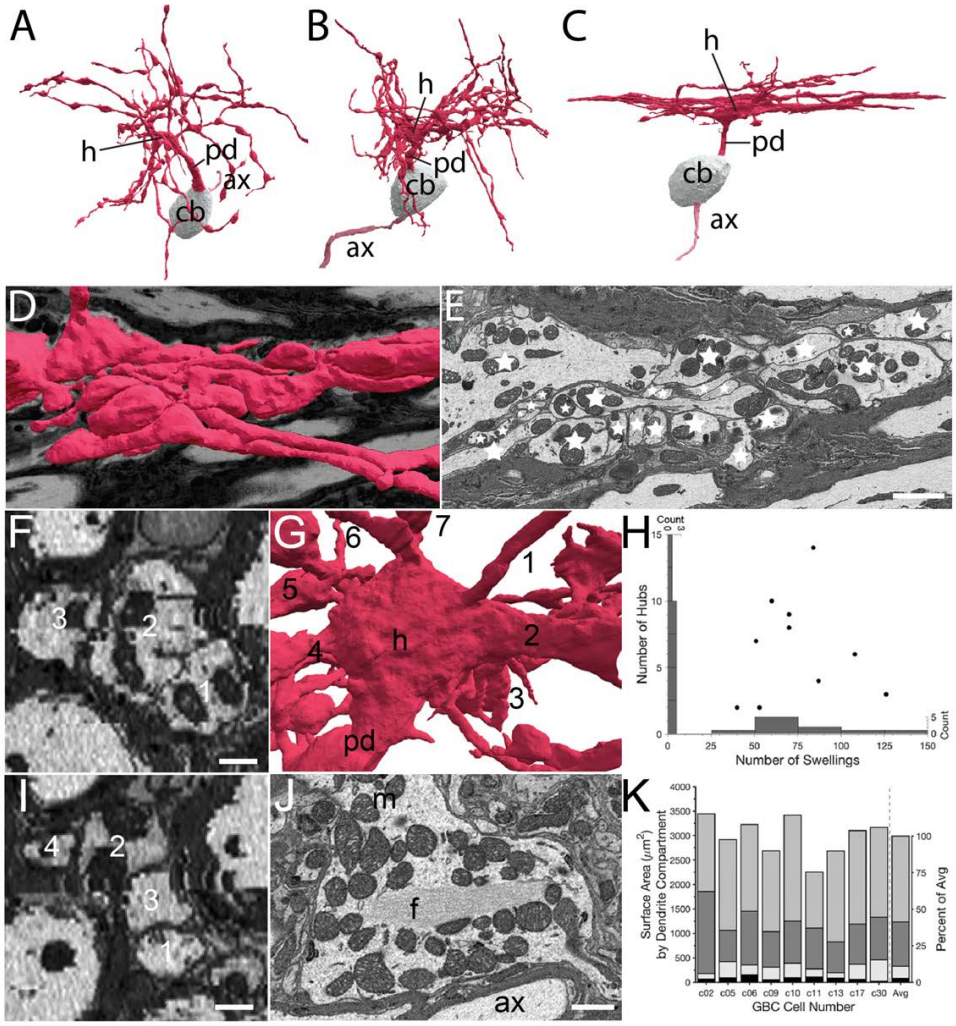

Figure 7. Volume EM reveals unique dendrite hub structures and branching patterns. (**A-C**). Dendrites vary in density of local branching and braiding of branches from the same cell, exhibiting (**A**) little, (**B**) medium or (**C**) dense branching and braiding. (**D-E**). Tangential view of dense braiding, showing (**D**) reconstruction of multiple branches in contact with one another and (**E**) a single EM cross section illustrating contact among the multitude of branches (individual branches identified with asterisks). (**F, I**). Two locations of cross-cut braided dendrites showing intertwining as change in location of branches (numbers) along the length of the braid. Images are lower resolution because viewing perspective is rotated 90° from image plane. (**G**). Reconstruction of dendrite hub (h) and its multiple branches (7 are visible and numbered in this image). (**H**). Swellings and hubs are prominent features of GBC dendrites. Histograms of numbers of swellings and hubs plotted along abscissa and ordinate, respectively. (**J**). Core of many hubs is defined by a network of filaments (f); also see Figure 7–***Figure Supplement 1***. Many mitochondria are found in hubs and can be in apparent contact with the filament network. (**K**). Partitioning of dendrite surface area reveals that proximal dendrite (black), hub (light grey), swelling (dark grey) and shaft (medium grey) compartments, in increasing order, contribute to the total surface area for each cell. Averaged values indicated in stacked histogram, to right of vertical dashed line, as percent of total surface area (right ordinate), and aligned with mean sizes on left ordinate). Scale bars: **E**, 2 microns; **F**, **I**, 0.5 microns; **J**, 1 micron.

Figure 7–Figure supplement 1. Dendritic Hubs, related to Figure 7G and J

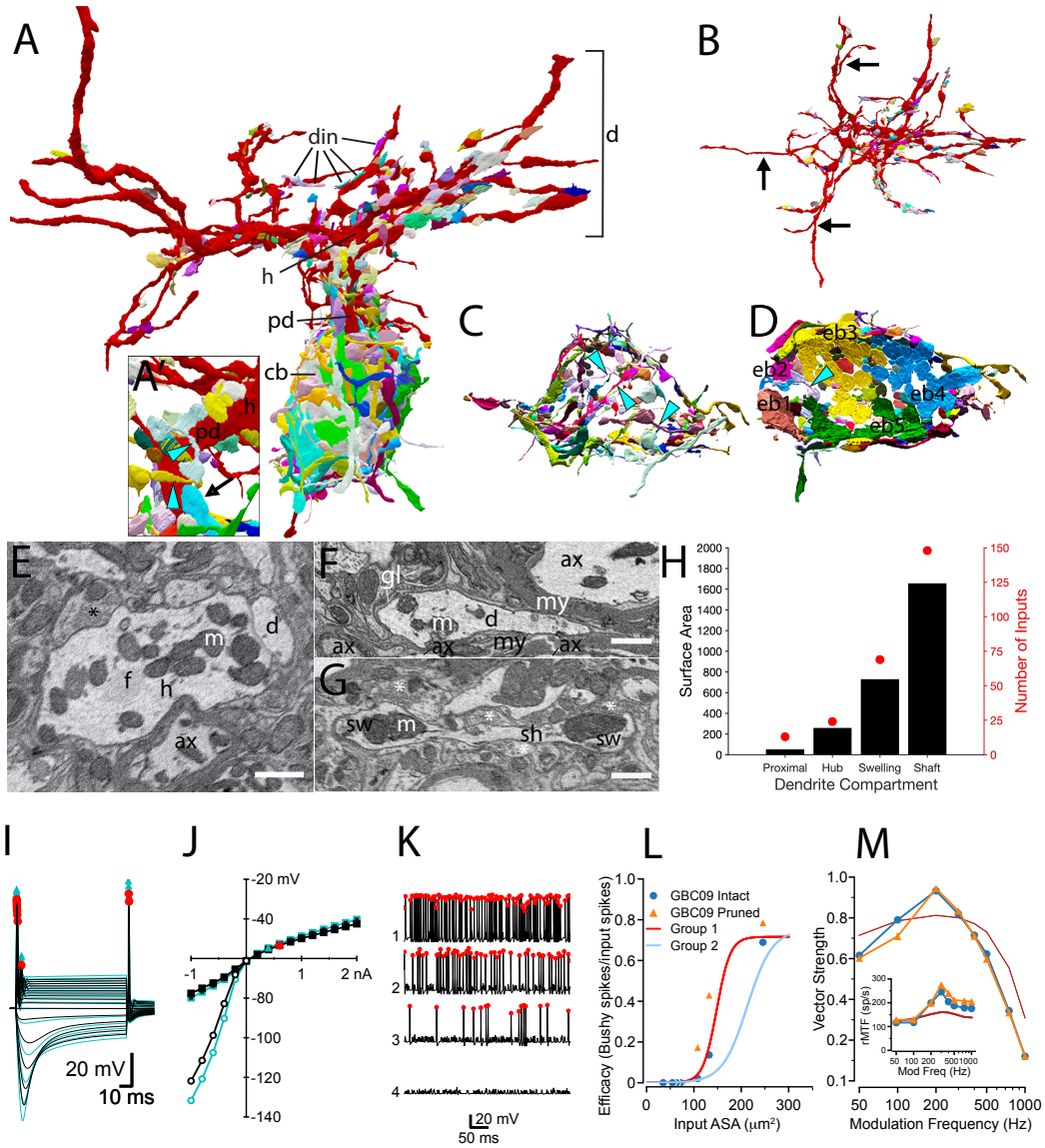

Figure 8. Synaptic map of GBC with modeled effects of removing non-innervated dendrites. (**A**) GBC09 oriented to show inputs (din) to dendrites (red, d), including proximal dendrite (pd), primary hub (h) and cell body (gray, cb). Nerve terminals are colored randomly. Terminals contacting dendrites at higher order sites than the primary hub are bouton-type of varying volume. (**A'**). Closeup view of pd reveals high density innervation by primarily bouton terminals that can be linked by small connections (cyan arrowheads), and extension of a somatic endbulb onto the basal dendrite (arrow). (**B**) Top-down view of dendrites only, illustrating that some branches are not innervated (longest non-innervated branches indicated by arrows) and that other branches are innervated at varying density. (**C**) Bouton terminals innervate all regions of the cb surface. Some boutons are linked by narrow connectors (cyan arrowheads). The cb is removed to better reveal circumferential innervation. (**D**) Inside-out view of cb innervation by endbulbs (eb; each is numbered and a different color) reveals that they cover most of the cb surface. Cb removed to reveal synaptic face of eb's. (**E**) Cross section through primary hub (h), showing filamentous core (f), mitochondria (m), input terminals (asterisks), and contact with dendrite of another cell. (**F**) Non-innervated dendrites (d) can be embedded in bundles of myelinated (my) axons (ax), and also ensheathed by glial cells (gl) and their processes (lines). (**G**) Both dendrite swellings (sw) and shafts (sh) can be innervated asterisks. (**H**) Proximal dendrites are innervated at highest density (number of inputs / surface area), and hubs, swellings and shafts are innervated at similar density. Scale bars: 1 μm in each panel. (I-M) Simulation results after pruning the non-innervated dendrites from this cell. (**I**) Voltage responses to current pulses, as in Figure 4–*Figure Supplement 3*, comparing the intact cell (black traces) with one in which non-innervated have been pruned (cyan traces). (**J**) IV relationship of data in (**I**) Cyan triangle indicates the spike threshold with the dendrites pruned compared to the intact cell (red circle). (**K**) Spikes elicited by the 4 largest individual inputs at 30 dB SPL with the dendrites pruned (compare to data shown in *Figure 4*A3). (**L**) Comparison of the efficacy of individual inputs between intact and pruned cell as a function of ASA. The red and light blue lines (Group1 and Group2) are reproduced from *Figure 4*D. (**M**) Comparison of VS to SAM tones in the intact and pruned configuration. Inset: Rate modulation transfer function (rMTF) comparing intact and pruned dendritic trees. Colors and symbols match legend in **(L)**. Dark red line is the rMTF for the auditory nerve input.

Figure 8–video 1. Exploration of a globular bushy cell (GBC) and all of its synaptic inputs. This video opens with a full view of GBC09, including its dendrites (red), cell body (beige), axon (pink), all somatic inputs (various colors), and all dendritic inputs (various colors). The cell undergoes a full rotation to display all of the inputs. The view zooms into the axon region, and rotates to illustrate all inputs onto the axon, including extensions of two large terminals (blue arrows pointing to purple and yellow terminals). The view zooms out to show the entire cell, the dendrites are removed, and the cell body is tilted. A cut plane passes from the edge to the middle of the cell, providing an inside-out view of the nearly complete synaptic coverage of the cell body. Large terminals are indicated by cyan arrows. All cellular elements are added, and the view shifts to reveal dense innervation of the proximal dendrite, including an extension of a large terminal (green terminal indicated by green arrow). The perspective shifts to a top-down view of the dendrites, indicating several dendritic branches (yellow arrows) that lack synaptic inputs.

with the non-innervated dendrites pruned. Pruning increased the input resistance from 20.2 to 25.1 MΩ, (***Figure 8***I, J) and increased the time constant from 1.47 ms to 1.65 ms. The threshold for action potential generation for short current pulses decreased from 0.439 to 0.348 nA (***Figure 8***J), but the cell maintained its phasic firing pattern to current pulses (***Figure 8***I compared to Figure 3–***Figure Supplement 3***, "Half-active"). These seemingly subtle changes in biophysical parameters increased the efficacy for the 4 largest inputs (0.689 to 0.786 (14%); 0.136 to 0.431 (216%); 0.021 to 0.175 (733%);, 0.00092 to 0.00893 (871%); ***Figure 8***K, L). Note that the increase was fractionally larger for the 2nd and 3rd largest inputs compared to the first, reflecting a ceiling effect for the largest input. We also examined how pruning non-innervated dendrites is predicted to affect phase locking to SAM tones (***Figure 8***M). Pruning decreased VS at 100 Hz, thereby sharpening tuning to 200 Hz relative to ANFs. The rMTF (***Figure 8***M, inset) shows a slightly higher rate after pruning of uninnervated dendrites. From these simulations, we hypothesize that GBCs can tune their excitability with functionally significant consequences by extension and retraction of dendritic branches, independent of changes in their synaptic map.

Discussion

Volume EM provides direct answers to longstanding questions

Key questions about ANF projections onto GBCs have persisted since the first descriptions of multiple large terminals contacting their cell bodies (***Lorente de Nó, 1933***; ***Cajal, 1971***). Volume EM offers solutions to fundamental questions about network connectivity not accessible by LM, by revealing in unbiased sampling all cells and their intracellular structures, including sites of chemical synaptic transmission (for reviews, see (***Briggman and Bock, 2012***; ***Abbott et al., 2020***)). By acquiring nearly 2,000 serial sections and visualizing a volume of over 100 μm in each dimension, we provided reconstruction of the largest number of GBCs to date, permitting more detailed analysis than was possible with previous EM methods that subsampled tissue regions using serial sections (***Nicol and Walmsley, 2002***; ***Spirou et al., 2008***; ***Ostapoff and Morest, 1991***). Here, we report on a population of GBCs in the auditory nerve root with eccentric, non-indented nuclei, ER partially encircling the nucleus, and somatic contact by a large number (5-12) of endbulbs of mostly smaller size. These cytological features, except for ER patterns, define a subpopulation of GBCs in mice more similar to globular (G)BCs than spherical (S)BCs as defined in larger mammals (***Cant and Morest, 1979b***,a; ***Tolbert et al., 1982***; ***Osen, 1969***; ***Hackney et al., 1990***) and are also consistent with criteria based on a larger number of endbulb inputs onto GBCs (***Lauer et al., 2013***) than BCs located in the rostral AVCN of rat (likely spherical bushy cells; see (***Nicol and Walmsley, 2002***)). In cat, the number of endbulb inputs onto GBCs is also large (***Spirou et al., 2005***, mean 22.9) and exceeds the number onto spherical bushy cells (***Ryugo and Sento, 1991***, typically 2).

Nanoscale (EM-based) connectomic studies are providing increasingly large volumetric reconstruction of neurons and their connectivity (***Bae et al., 2021***; ***Scheffer et al., 2020***; ***Witvliet et al., 2021***). In this report, we add pipelines from neuron reconstruction to biophysically-inspired compartmental models of multiple cells. These models expand on previous GBC models that used qualitative arguments, or single or double (soma, dendrite) compartments (***Joris et al., 1994b***,a; ***Rothman et al., 1993***; ***Rothman and Manis, 2003c***; ***Spirou et al., 2005***; ***Koert and Kuenzel, 2021***). By matching inputs to a cochlear model (***Zilany et al., 2014***; ***Rudnicki et al., 2015***), we created a well-constrained data exploration framework that expands on previous work (***Manis and Campagnola, 2018***). We propose that generation of compartmental models, from high-resolution images, for multiple cells within a neuron class is an essential step to understand neural circuit function. This approach also reveals that there are additional critical parameters, such as ion channel densities in non-somatic cellular compartments, including non-innervated dendrites, that need to be measured. From these detailed models, more accurate reduced models that capture the natu-

ral biological variability within a cell-type can be generated for efficient exploration of large-scale population coding.

Toward a complete computational model for globular bushy cells: strengths and limitations

We propose that the pipeline from detailed cellular structure to compartmental model, informed by physiological and biophysical data on GBCs, provides a framework to highlight missing information that is needed to better understand the mechanisms GBCs employ to process sound, and thereby provide a guide for future experimentation. Some of the information that is missing is inherent in the limitations of the methods employed, and other information must derive from experiments using other techniques.

SBEM has provided an unprecedented spatial scale (a cube of roughly 100 μm per side) for high-resolution reconstruction of entire cells (10 complete, 16 partial) in this brain region. A range of dendrite geometries in terms of branching density are revealed, but the number of reconstructed cells remains constrained by the imaged volume due to the tradeoff between spatial resolution, size of the volume, and time to acquire the images. Although many details of GBC dendrite structure are revealed for the first time, it is not clear whether the full diversity of dendrite structure has been captured. The imaging parameters for this volume were set to permit identification of vesicles, vesicle clusters and synapses, but did not allow us to assess vesicle shape. Thus, the excitatory or inhibitory nature of synapses based on vesicle morphology following glutaraldehyde fixation (***Uchizono, 1965***; ***Bodian, 1970***) could not be made. Endbulb neurotransmitter phenotype was known by tracing nerve terminals back to their ANF of origin. The axons of small terminals were not reconstructed, except for selected examples locally. Future analysis of the image volume will require reconstructing longer sections of these axons to reveal regional branching patterns. These patterns can also be matched to other experiments in which axons innervating GBCs from identified source neurons are labeled using genetically driven electron dense markers (***Lam et al., 2015***), and images are collected at higher spatial resolution to permit accurate quantification of synaptic vesicle size, density and shape.

The modeling framework is constrained by anatomical metrics and measurements of biophysical parameters of GBCs from the literature, stemming primarily from brain slice and acute isolated cell experiments. It is encouraging that the response of the model to standard manipulations, such as injection of current steps and activation by tones, illustrates that the fundamental features of the model, including PSTH shapes and firing regularity, that align with experimental biology. The purpose of engaging the modeling pipeline, however, is both to identify its limitations, thus revealing key parameters to guide design of future experiments, and also to predict responses of GBCs that can be tested in future *in vivo* recordings. Given the relatively large number of endbulbs per cell (5-12), it is likely that cells are innervated by ANFs with different distributions of spontaneous rates, and the particular patterns of convergence are expected to affect model responses. Currently, we are not able to assign endbulb size, morphology or axon branching patterns to spontaneous rate classes, although some evidence supports such a correlation (***Wang et al., 2021***; ***Sento and Ryugo, 1989***; ***Liberman, 1991***; ***Rouiller et al., 1986***). Future experiments that define terminal shapes associated with spontaneous rate, perhaps capitalizing on correlations with gene or protein expression (***Sun et al., 2018***; ***Shrestha et al., 2018***; ***Petitpré et al., 2018***), can be mapped onto this data set. Although synaptic sites operated independently in the model, the measured nearly constant density of synapses across differing terminal sizes yielded a monotonic relationship between vesicle release and terminal size. The similar mean amplitudes for mEPSCs across experimental recordings from mouse GBCs (***Gardner et al., 1999***; ***Wang and Manis, 2005***; ***Cao and Oertel, 2010***) argues that parameters such as the number of postsynaptic receptors or synaptic vesicle volume, which could affect synaptic weight, vary similarly across endbulbs and also support a monotonic relation-

ship between weight and endbulb size. Additional factors, such as temporal dynamics of release probability that may differ with size or SR category, or postsynaptic receptor density, can modify this relationship and can be addressed in the model with new experimental data. Furthermore, just as volume EM reveals non-canonical dendrite structures (hubs) and branching properties, the complement of conductances in GBC dendrites, and potential differences among hub, swelling, shaft, proximal dendrite and non-innervated regions is not known. The compartmental models will be improved by new experiments that directly measure these missing conductances and, for all cellular compartments, the co-variance of conductance values for individual cells. Because the models have high spatial resolution, new data can be readily associated with dendrite compartments (proximal dendrite, hubs, swellings, shafts), soma and AIS.

We showed how tuning to SAM tones is predicted to vary based on the entire complement of endbulb sizes onto individual GBCs, but there are few equivalent experimental observations for comparison. The few studies that characterized GBC responses to sound in mice have used limited sets of stimuli (***Roos and May, 2012***; ***Kopp-Scheinpflug et al., 2003***; ***Willott et al., 1984***) and have not yet provided the kind of structure-function correlations that are available from other species. The only published data that we are aware of for responses to SAM stimuli from mouse CN (***Kopp-Scheinpflug et al., 2003***) show lower VS than our model predicts. However, a direct comparison is difficult because that study reported responses generally for VCN (not specified by cell type), and stimuli were delivered at a high intensity, 80 dB SPL, whereas we used a low-intensity sound that results in maximal SAM VS in low-threshold ANFs. In other species (cat, gerbil, guinea pig) SAM VS is lower in all SR classes of ANFs at intensities well above their thresholds, including at 80 dB SPL, than nearer threshold (***Smith and Brachman, 1980***; ***Joris and Yin, 1992***; ***Cooper et al., 1993***; ***Dreyer and Delgutte, 2006***). This intensity-dependent pattern is also characteristic of neurons in the VCN in other species (***Frisina et al., 1990***; ***Rhode and Greenberg, 1994***). Thus, our predicted responses to SAM tones are qualitatively consistent with existing experimental data but this conclusion needs to be experimentally tested.

Other future enhancements to the models, by characterizing inputs by their putative excitatory or inhibitory function based on vesicle shape, are an important next step in the evolution of these detailed models. In addition, mapping local and feedback excitatory and inhibitory pathways near CF from specified cellular sources (***Caspary et al., 1994a***; ***Campagnola and Manis, 2014***; ***Xie and Manis, 2013a***; ***Cant and Morest, 1978***; ***Ngodup et al., 2020***), and knowing their responses to SAM sounds (e.g., for dorsal cochlear nucleus tuberculoventral cells), can help to incorporate their important roles in spectral and temporal processing of GBCs (***Caspary et al., 1994b***; ***Gai and Carney, 2008***; ***Keine and Rübsamen, 2015***; ***Keine et al., 2016***). Lastly, we do not have a good handle on the variability of responses within the GBC class that could be used, even in a statistical sense, to constrain model parameters for specific exploration. Given the increasing prevalence of mice in hearing research, especially in studies of cochlear function and pathology, we expect that these data will be forthcoming.

An optimal dataset to test our predictions would match individual cell responses to sound with the detailed structural information from volume EM. Previous connectomic studies that mapped neural activity from cell populations into the EM volume from the same animal used Ca^{2+} imaging to measure spike-evoked activity (***Bock et al., 2011***; ***Turner et al., 2022***; ***Consortium et al., 2023***; ***Ding et al., 2023***). However, the resolution of the questions regarding GBC function require near-microsecond precision measurements of action potential timing, and bulk Ca^{2+} signals are too slow to provide this information. Emerging technologies such as genetically encoded voltage-sensitive optical indicators measured with high-speed imaging (***Villette et al., 2019***) may become applicable to this system in future experiments.

The anatomically and functionally constrained model developed here can serve as templates onto which new data are mapped in order to explore *in silico* representations of GBC function in

hearing. The models focus attention on experimental data that is missing in the literature, and become a guide to future studies. Furthermore, because EM reveals subcellular and non-neuronal structures, this dataset also is branch point for complementary modeling frameworks to understand other cell functions that contribute to the neural encoding of sound.

Multiple cellular mechanisms to tune excitability

The variability of responsiveness in cells and patterns of convergence in circuits are essential factors that help optimize the representation of sensory information (***Ashida et al., 2019***; ***Perez-Nieves et al., 2021***). We predict that dendrite surface area varies sufficiently to adjust spike threshold across the GBC population. Dendrite surface area defined two GBC populations, where cells with smaller areas exhibited greater excitability. Reconstruction of additional cells will be needed to clarify whether excitability is clustered or occurs along a continuum.These two populations did not respect GBC grouping based on the profile of endbulb sizes (coincidence-detection or mixed-mode) or the density of local dendrite branching. Gene expression profiling in mice has revealed differences between BCs in the rostral VCN and caudal AVCN/rostral PVCN (***Jing et al., 2023***), coupled with differences in electrical excitability. Future experiments that combine techniques will be required to relate these molecular profiles to dendrite branching, dendrite surface area, and somatic innervation profiles revealed only by high-resolution structural imaging. Our demonstration of the lack of synaptic innervation along entire branches and increased excitability following their removal, offers an additional mechanism to tune excitability. Although GBCs lack dendritic spines, they may grow or prune dendrite branches in response to cochlear pathology or changing acoustic environment, as has been shown for other brain regions in pathological states (***Furusawa and Emoto, 2020***), experience-driven paradigms (***Berry and Nedivi, 2016***), or during physiological cycles such as estrous or hibernation (***Ferri and Flanagan-Cato, 2012***; ***von der Ohe et al., 2006***). The dynamics of dendrite branch remodeling have not, to our knowledge, been examined at high temporal resolution, but are amenable to modern imaging methods such as have been applied to studies of dendritic spine structural plasticity.

We also found that the length of the AIS, which is the spike initiation zone for most neurons (***Bender and Trussell, 2012***), varied across GBCs by 50% (14-21 μm). Changing AIS length, while assuming a constant density of Na^+ channels, is predicted to non-linearly change rheobase by 50% (***Figure 4***K). Interestingly, the AIS of each GBC is contacted by multiple small inputs. Inhibitory inputs onto the AIS of other neuron types have been shown experimentally and computationally to modulate spike generation (***Bae et al., 2021***; ***Schneider-Mizell et al., 2021***; ***Veres et al., 2014***; ***Franken et al., 2021***). We reveal that in nearly all GBCs one of the large somatic inputs extends onto the hillock and AIS. In our models, the proximal axon is electrotonically close to the somatic compartment, so further investigation is required to determine whether direct AIS innervation can increase synaptic efficacy for driving spikes. The AIS length and location of Na^+ channels have been also shown to be sensitive to the history of neural activity (***Kuba et al., 2010***; ***Kuba, 2012***; ***Grubb and Burrone, 2010***), and merit investigation in GBCs.

Dendrite surface area and AIS geometry and innervation emerge as potential homeostatic mechanisms to regulate excitability. We expect that reconstructions of a larger population of GBCs will better reveal the distribution of these morphological features, and may clarify additional regulatory mechanisms. Thus, the combination of high-resolution structural analysis and compartmental modeling specifies focused topics for further study.

Convergence of weak and strong inputs regulates temporal fidelity

We provide the first complete catalogue of numbers of ANF inputs and their sizes (38 – 270 μm^2), revealing a broad range of subthreshold endbulb sizes and raising questions about the functions of smaller endbulbs. GBCs were proposed to achieve their highest temporal fidelity by acting as

a coincidence detector for convergence of subthreshold endbulb inputs (***Rothman et al., 1993***; ***Rothman and Young, 1996***; ***Joris et al., 1994a***). In the present simulations, we took advantage of the ability to selectively activate or silence specific inputs, which allowed us to separately assess the contribution of suprathreshold and subthreshold inputs across a biologically relevant range of strengths. Our simulations predict that only about one-half of GBCs in mice operate strictly in the coincidence detection mode, whereas the remainder operate in a mixed integration mode. A larger sample of cells may clarify whether the sizes of the largest inputs across the population of GBCs are truly a continuum or occur in discrete groupings. Furthermore, we find that by conventional measures of phase locking to an amplitude-modulated tone, the activity of the weaker inputs substantially improves temporal precision relative to individual ANFs for modulation frequencies up to 200 Hz. In contrast, the largest inputs alone provide better temporal precision than combined inputs only at high modulation frequencies, especially if they are suprathreshold. Supporting the generality of these observations across stimuli, improved temporal precision in the coincidence and mixed modes is also mirrored when using a different measure, the shuffled correlation index, for transient stimuli. Our results are also consistent with simulations showing that small ANF synapses on dendrites can improve temporal precision in the presence of large somatic inputs (***Koert and Kuenzel, 2021***). We also observed that otherwise subthreshold, but large, inputs can effectively drive more spikes by depending on near-simultaneous activation of weaker inputs, than can larger suprathreshold inputs. The suprathreshold input in mixed mode cells decreased VS to ANF values at low frequencies, raising questions regarding their functional contribution to GBC sound encoding. On the other hand, their activation also increased the AP rate, and thereby elevated the rMTF above ANF values at these same frequencies. Thus, we predict that the pattern of convergence of ANF inputs with a wide range of strengths provides a mechanism for improved temporal precision and higher spike rates over part of the range of behaviorally relevant envelope modulation frequencies.

New dendrite structures

Our high-resolution images revealed a previously undescribed dendrite structure, which we name a hub. The high branching order of hubs helps explain why GBC dendrites are contained locally to the cell body. We also revealed that dendrites branch and align adjacent to one another. This arrangement increases the surface area to volume ratio, which affects the excitability of the cell. Both of these features likely function in part to shorten the overall dendrite electrotonic length and increase the importance of the dendrites in the integration of somatic synaptic inputs. Inspection of published GBC images based on Golgi or tract tracing techniques reveals cells with thickened proximal dendrites (***Webster and Trune, 1982***; ***Lorente de Nó, 1981***; ***Brawer et al., 1974***). We suggest that some of these represent unresolved dense local branching and hub structures that are better revealed by EM across many sections. We noted that swellings were a prevalent feature of the dendrites and, contrary to reports in cat based on subsampling (***Ostapoff and Morest, 1991***), swellings were innervated at similar densities to shafts. The partition of dendrite compartments into hubs, swellings and shafts may have functional significance if, for example, these structures have differential sources of innervation or are endowed with different densities of ion channels or pumps (***Brownell and Manis, 2014***). The latter may relate to filament bundles and concentrations of mitochondria inside of hubs.

Although our SBEM volumes lacked resolution to assess vesicle shape, it is likely that some of the smaller dendritic inputs are inhibitory (***Gómez-Nieto and Rubio, 2009***). Hubs may also provide efficient sites to nullify excitatory inputs occurring along multiple distal branches through current shunting. Many of the dendritic inputs were linked by short branches. Thus, non-innervated dendrites also afford locations for adaptive regulation of synaptic efficacy via formation or retraction of short branches and new terminals.

Methods and Materials

Ethics Approval

All procedures involving animals were approved by the West Virginia University (WVU) Institutional Animal Care and Use Committee and were in accordance with policies of the United States Public Health Service. No animal procedures in this study were performed at other institutions.

Serial Block-Face Scanning Electron Microscopy

All reagents for transcardial perfusion were purchased from Sigma-Aldrich, unless otherwise noted. An adult (P60) FVB/NJ mouse (NCI; Frederick, MD and Jackson Laboratory; Bar Harbor, ME) was anesthetized using Avertin (20 mg/kg) injection IP, and perfused transcardially with normal Ringer's solution containing xylocaine (0.2 mg/ml) and heparin (20 U/ml) for 2 min at 35°C followed by 0.15 M cacodylate buffer containing 2.5% glutaraldehyde (Polysciences), 2% paraformaldehyde (Fisher Scientific) and 2 mM calcium chloride at 35°C for 5 min. The skull was placed on ice for 2 hours, then the brain was removed from the skull and post-fixed for an additional 18 h at 4°C in the same solution. Brain tissue was cut into 200-μm-thick sections in the coronal plane using a vibratome (Ted Pella) in ice-cold 0.15 M cacodylate buffer containing 2 mM calcium chloride, then washed for 30 min in the same solution. The ventral cochlear nucleus (VCN) was identified in free-floating sections using a stereo-microscope, and sections were photographed before and after dissection of the CN from the surrounding tissue.

The tissue sections were prepared for Serial Block-Face Scanning Electron Microscopy Imaging (SBEM) using an established protocol in our group (***Holcomb et al., 2013***). All staining and embedding chemicals were purchased from EM Sciences unless otherwise indicated, and all water was nanopure filtered (Nanopure Diamond, Barnstead International). Initial staining was performed in a solution combining 3% potassium ferricyanide in 0.3 M cacodylate buffer with 4 mM calcium chloride with an equal volume of 4% aqueous osmium tetroxide, for 1 h at room temperature (RT). Tissue was processed sequentially through filtered 1% thiocarbohydrazide for 20 min at RT, 2% osmium for 30 min at RT, and 1% uranyl acetate overnight at 4°C. Tissue underwent triple rinses in H_2O for 5 min each between each step and was triple rinsed in H_2O at RT for 30 min after the final step. Sections were placed into filtered lead aspartate solution (0.066g lead nitrate dissolved in 10 ml of 0.003 M aspartic acid solution, pH adjusted to 5.5 with 1N KOH, warmed in a 60°C oven for 30 min). The tissue was rinsed five times (3 min each), photographed, then dehydrated through graded alcohols into acetone, and flat-embedded in Durcopan resin (Electron Microscopy Sciences) between mylar strips in a 60°C oven for 48 h. Tissue samples were again photographed and shipped to the National Center for Microscopy and Imaging Research (University of California San Diego) for imaging.

Resin-embedded tissue was mounted on an aluminum specimen pin (Gatan) using cyanoacrylic glue and precision trimmed with a glass knife to a rectangle ≈0.5 × 0.75 mm so that tissue was exposed on all four sides. Silver paint (Ted Pella) was applied to electrically ground the edges of the tissue block to the aluminum pin. The entire specimen was then sputter coated with a thin layer of gold/palladium to enhance conductivity. After the block was faced with a 3View ultramicrotome unit (Gatan) to remove the top layer of gold/palladium, the tissue morphology became visible by back-scattered electron detector imaging using a Merlin scanning electron microscope (Carl Zeiss, Inc.). A low-magnification image (≈500X) was collected to identify the proper location in the VCN (caudal and in the auditory nerve root) for serial image collection. This region was selected because it has a high concentration of globular bushy cells (GBC, (***Harrison and Irving, 1966***; ***Osen, 1969***; ***Brawer et al., 1974***)). The imaged volume was located at approximately the mid dorsal-ventral location of the VCN. Imaging was performed using a pixel dwell time of 0.5 μs, tissue was sectioned at a thickness of 60 nm, and the imaging run required 7.5 days. Accuracy of section thickness was

estimated by assuming circularity of mitochondria and comparing the diameter of longitudinally oriented organelles with diameters measured in the image plane (***Wilke et al., 2013***).

A volume of 148 μm x 158 μm x 111 μm was imaged with an in-plane pixel resolution of 5.5 nm. The image volume contained 31 complete cell bodies, including 26 GBCs. Due to the large size of the volume (1.4 TB) and the goal of reducing noise in the image, most of the analysis was performed by down-sampling in the image plane. Voxel averaging at 2 x 2 binning increased the dimensions of each voxel to 11.0nm x 11.0 nm x 60.0nm. With these imaging parameters, synaptic vesicles can be identified and, in many cases, a post-synaptic density, which appears as darkening on the post-synaptic membrane. Synapses were defined by collections of vesicles near the presynaptic membrane across at least 3 sections and with at least one vesicle in contact with the membrane (***Jackson et al., 2021***). Images were assessed to be of high quality for segmentation due to well preserved membranes, as evidenced also by uniform preservation of tightly wrapped myelin, and the absence of degenerating profiles.

Segmentation

Seg3D (https://www.sci.utah.edu/cibc-software/seg3d.html, University of Utah, Scientific Computing and Imaging Institute) was used to manually segment the structures of interest from the raw data volume. These structures (somata, nuclei, dendrites, axons, nerve terminals) were identified and segmented according to accepted morphological criteria for the mammalian CNS (***Peters et al., 1991***). The tracing tool was used to paint all pixels interior to the membrane. This strategy permitted the creation of 3D meshes for adjacent structures that did not overlap. Student segmenters were organized into small teams of trained workers supervised by an expert segmenter (who completed a course called Connectomics taught by Dr. Spirou). Expert segmenters reviewed all work by their team of trained segmenters. The 3D meshes of all dendrites were reviewed by expert segmenters and Dr. Spirou in VR (syGlass software; IstoVisio, Inc.), overlaid onto the EM image volume so that anomalous branches and structures could be identified, and enclosed ultrastructure and membranes could be incorporated into the evaluation. Tracing the dendrites of all 31 cells provided an internal self reference preventing incorrect assignment of branches to a particular cell. Tracing of dendrites for import into the modeling environment provided additional rigorous review for the subset of 10 cells with complete or near-complete dendritic trees, Endbulb terminals were traced by the same segmenting teams with the same review procedures. Tracing all large inputs and several smaller inputs onto the 21 GBCs reported here also provided an internal check that branches of inputs were not missed or assigned to the incorrect terminal. Testing methods for calculation of the ASA followed by performing the calculation for all large inputs onto all cells provided additional rigorous review of the large terminal segmentations.

Fascicles of nerve fibers traverse the volume in the coronal and sagittal planes. ANFs formed the fascicles in the coronal plane. These fascicles were outlined in every 100th section so they could be tracked to determine their extent of splitting and merging. Branches from axons within the fascicles that led to endbulb terminals were also segmented and tabulated, to determine whether axons in particular fascicles gave rise to endbulb terminals within the volume or tended to converge onto the same cellular targets. Terminal size was quantified by measuring the apposed surface area with the postsynaptic membrane, omitting regions where the membranes were separated by intervening glia or extracellular space. We reconstructed the terminals onto each cell that appeared larger than bouton terminals. On two cells we reconstructed all terminals, and from these data we created a histogram of terminal sizes and a definition of minimum size for the large terminal class. We then verified that terminals larger than this threshold were indeed branches of ANFs (see Results). All endbulb axons were traced visually from the terminal retrogradely to their parent ANF or to the location where they exited the image volume. The axon and fiber diameters were calculated from a subset of fibers that had a segment with a straight trajectory either parallel or

perpendicular to the image plane, in order to calculate their axon and fiber diameters. A similar procedure was applied to a subset of ANFs (see Fig. 5F). To visualize the spatial relationship of endbulbs and ANF branches to ANF fascicles, all of these structural elements for all endbulb inputs to four cells were segmented using the tracing tool in syGlass.

Three-Dimensional Reconstruction

3D models of the structure of interest were exported from Seg3D as a VTK file and converted to OBJ format using a custom Python script or, in newer versions of the software, exported directly as OBJ files. The meshes in OBJ format were imported into Blender (https://www.blender.org) for processing. Meshes were first decimated by using the decimate modifier tool in collapse mode to merge neighboring vertices progressively while considering the shape of the mesh ***Low*** (***1997***). The meshes are then smoothed using the smooth modifier tool. While these mesh processing steps are suitable for visualization, they do not produce sufficiently accurate surface area or volume measurements. Thus, we evaluated more consistent mesh processing algorithms.

We implemented accurate mesh processing by applying the GAMer2 algorithms and procedures systematically to all meshes in order to create so-called computational meshes (***Lee et al., 2020b***). Surface meshes of segmented objects were generated by performing marching cubes, and produced structures having greater than 1 million vertices due to the high-resolution images and anisotropic sampling during imaging (resolution in x-y plane was ten times resolution in z direction). Anisotropic sampling generates a stair-step effect in the rendering (***Figure Supplement 1***A). Initial vertex decimation was designed to generate meshes containing 100,000 – 300,000 vertices and reduced time to perform subsequent processing. Experimentation revealed this size range to be the minimum that preserved geometry upon visual inspection. Next, twenty iterations of angle-weighted smoothing (AWS) were applied, which generated nearly equilateral triangles for the mesh faces (***Figure Supplement 1***B). This geometry is a characteristic of a well-conditioned mesh, which maintains complete surfaces through subsequent processing (***Shewchuk, 2002***). Two iterations of normal smoothing (NS) were then applied which, in combination with AWS, resulted in a reduction of surface area. The surface area reached an asymptote after the second NS step, confirmed by running three cell bodies through a second round of AWS and NS, indicating that the stair-step effect was minimized after the first round of AWS and NS (***Figure Supplement 1***C). We visually inspected the meshes during mesh processing and confirmed that all features of the mesh were well-preserved and stair step features were removed after one round of AWS and NS (***Figure Supplement 1***B). Therefore, we determined this stage of mesh processing to be an accurate stopping point.

Assignment of Synaptic Weights

We assigned synaptic weights as a density of synapses per square micron of directly apposed pre- and postsynaptic membrane, the latter of which we term the apposed surface area (ASA). EM affords the opportunity to measure accurately the membrane apposition, and account for features such as extended extracellular space (***Cant and Morest, 1979a***; ***Rowland et al., 2000***), where the membranes separate, and interposition of glial processes. We generated an algorithm and custom Python script to identify only the ASA and calculate its summed value for each nerve terminal https://github.com/MCKersting12/nrrd_tools). This script reads the original segmented image volumes of the two objects contacting one another, which may have been traced in different subvolumes of the original volume (subvolumes were created to permit multiple segmenters to work in parallel), and transforms them to have the same origin (pixel-spacing, height, width, and length). If the segmented terminal and postsynaptic cell have overlapping voxels, the overlap is removed from the soma because the terminal segmentations were typically more accurate. Next, the terminal is dilated by 3 voxels in the x-y plane and then, because the volume is anisotropic, another

3 voxels in all directions. The dilation in z was tested and this value was chosen based on visual inspection to provide overlap selectively of the ASA. The overlapping region between the dilated terminal and the soma volume is extracted as a separate volume, and the marching cubes algorithm is performed on this separated volume. The surface area of the resultant mesh, which appears as a flattened volume, is divided by two because we are only interested in the contact area to generate the ASA.

Synapses can be identified in our SBEM volume by clustering of synaptic vesicles along the presynaptic membrane in at least 3 serial sections, direct contact of at least one vesicle with the presynaptic membrane, and a concavity in the postsynaptic membrane, the latter of which is typical of endbulb terminals in the cochlear nucleus in aldehyde fixed tissue (***Spirou et al., 2008***; ***Cant and Morest, 1979a***; ***Ryugo et al., 1997***). A postsynaptic density is typically found but is not present in all cases, so was not used as an explicit criterion. Each large input contains multiple synapses, so the number of synapses was quantified for 23 terminals of varying sizes, and density (#synapses/μm^2 was calculated using the ASA for each terminal. The average synapse density was applied to terminals for which the ASA was determined but synapses were not counted, to achieve an estimate of the number of synapses in each terminal reconstructed in this study.

Model Generation

Biophysically-based models were generated for each reconstructed cell, using the ASA data for individual auditory nerve inputs, and the compartmental reconstructions. The modeling was performed as a predictive exercise, using previously measured biophysical parameters for synapse release dynamics, postsynaptic receptors, and ion channels, along with a standard model of auditory nerve responses to sound. The principal free parameters were the densities of channels in different cell compartments. The channel densities were calculated based on the ratios of densities for somatic models in a previous study (***Rothman and Manis, 2003c***), measured densities in voltage clamp from mouse GBCs for the low-threshold potassium conductance, and relative densities in the axon initial segment and hillock from other central neurons. Because ion channel densities in the dendrites of bushy cells have not been measured, we bracketed the likely range by testing models with passive dendrites, fully active dendrites (densities were the same as in the soma) and half-active dendrites. Thus, the models are predictive given the constraints of unmeasured channel densities. To accomplish this, the models were built up in a series of steps: morphological reconstruction, surface area adjustments, base channel density adjustment, and overall channel density assignment. Synaptic conductances were constrained by previous measurements (***Raman and Trussell, 1992***; ***Xie and Manis, 2013b***), and the only free variable was the number of sites for each multi-site synapse, which was set according to the ASA measurements and release site counts from the SBEM material.

Translating Reconstructions to NEURON models

We rendered the SBEM mesh into a modified version of the SWC file format (***Cannon et al., 1998***) using the tracing tool in syGlass. Each reconstructed part of the cell is represented as a series of conical frustums with starting and ending radii. We also annotated groups of points with a named morphological feature of the section. Identified morphological features were given new tags in the SWC file, and included the myelinated axon, axon initial segment, axon hillock, soma, proximal dendrites, dendritic hubs, distal dendrites, and dendritic swellings. Next, the SWC files were translated to HOC files using a Python script. The script added groups of SWC points in a 3D shape format (pt3d) to create short sections composed of at least three and up to 50 segments. This translation retained the detailed geometry of the cells. Comment fields in the HOC files referenced the original SWC point for each 3D point in Neuron, which facilitated mapping voltages in processes back to the original mesh representation, and confirming that the translation proceeded correctly. This

annotation also allowed us to perform manipulations that removed specific parts of the original reconstruction.

We then compared the original SBEM mesh files' surface area representations with those of the 3D geometry HOC files. The mesh represented the cell surface at a high resolution that captured membrane crenelations, even after reducing the mesh density with GAMer2 (***Lee et al., 2020b***) and subsequent smoothing. In contrast, the SWC and HOC representations capture the mesh structure using simple frustrated cones, which have smooth surfaces. Consequently, the mesh surface area was always significantly greater than the surface area computed from the HOC representation. The surface area determines the capacitance and plays a fundamental role in establishing ion channel densities and the transmembrane leak resistance in the model cells. We therefore compensated for these surface area differences by inflating the compartment diameters in the HOC file by the ratio between the mesh and HOC areas, while not changing the lengths. Separate inflation factors were calculated for the soma and for the entirety of the dendritic tree, because the mesh's ratio to HOC surface areas for these regions was different. NEURON instantiates compartments (as "segments") from the 3D reconstructions. However, there is no analytical solution to the inverse problem of recalculating the total area's diameters. Therefore, we computed the inflation factor iteratively until the reconstructed area, as computed from NEURON, matched the mesh area. For the bushy cells, the soma's inflation factor averaged 1.486 (SD 0.227), and the factor for the dendritic tree averaged 1.506 (SD 0.145). The ratio of the soma inflation factor to the dendrite inflation factor for different reconstructions varied from 0.78-1.38 (mean 0.995, SD 0.195). The last step in establishing the geometry for simulations was determining the number of segments necessary to maintain an appropriate spatial discretization. The number of segments for each section was recomputed using the d-λ rule (***Carnevale and Hines, 2006***), at 1000 Hz. Because many of the reconstructions already had short section lengths, this step affected only a fraction of the sections for any given cell. All current clamp simulations were run with a time step of 25 µs.

Ion Channels and Receptors

Cells were "decorated" with Hodgkin-Huxley style ion channels based on biophysical measurements from previous studies. The kinetic measurements for K^+ channels were obtained from acutely isolated bushy neurons that lacked dendritic trees (***Rothman and Manis, 2003a***), scaled to 37°C (***Rothman and Manis, 2003b***). We drew K^+ channel density estimates from measurements made from cells in mouse brain slices (***Cao et al., 2007***), scaled as described below. Sodium channels were represented by a modified model (***Xie and Manis, 2013b***), which incorporated cooperative interactions between channels (***Huang et al., 2012***; ***Ilin et al., 2013***; ***Manis and Campagnola, 2018***). Actual conductance densities for the dendrites, axon hillock, axon initial segment, and nodes of Ranvier are not known. To address these uncertainties, we decorated the cell compartments using density distributions that have been estimated for other neurons, as described next.

Axons: Axons were reconstructed from the soma to the first internodal (myelinated) region for 8 of the 10 reconstructed bushy cells. Data from mouse bushy cells from ***Yang et al.*** (***2016***) indicates that the Na^+ channel density is lower in the soma than in the axon hillock and that the action potential initiation begins distally, likely in the AIS. Lacking direct measurements in bushy cells, we used the experimental and model data from ***Kole et al.*** (***2008***) from layer V cortical neurons to guide the relative channel densities. The axon hillock channel density for Na^+ channels was set to five times that of the soma, and the initial segment was 100 times that of the soma. The hillock and AIS compartments were each decorated uniformly, to approximate the uniform distribution reported for immunostaining of Na^+ channels (***Kuba et al., 2015***), although there is some data suggesting that channel density and composition vary with distance from the soma (***Lorincz and Nusser, 2008***; ***Hu et al., 2009***). The assignment of spatially uniform conductance densities to the AIS represents a first-order assumption, as we lack experimental data with appropriate resolution to justify other

distributions in GBCs. With this decoration, the total AIS Na^+ conductance in the model is a function of AIS length, and therefore also affects action potential threshold and amplitude. Variations in AIS length have been correlated with neuronal excitability (***Grubb and Burrone, 2010***; ***Kuba et al., 2010***; ***Kim et al., 2019***; ***Kaphzan et al., 2011***), and tonotopic position in nucleus laminaris (***Kuba et al., 2006***). Na^+, K^+ channel and I_h channel densities are shown in ***Table 1***.

Decoration Type			
Channel	Myelinated axon	AIS	AH
Na	0.0	100.0	5.0
K_{HT}	0.01	2.0	1.0
K_{LT}	0.01	1.0	1.0
I_H	0.0	0.5	0.0
$Leak$	0.00025	1.0	1.0

Table 1. Densities of channels used to decorate the axon compartments of bushy cells. Values are given as ratios relative to the standard decoration of the somatic conductances.

For GBC02 and GBC05, the axon left the tissue block before becoming myelinated. To compensate, we replaced the axon hillock, initial segment and first myelinated region with a “standard axon” based on the average axon lengths and diameters from the other 8 cells for simulations of these cells. These cells were not used in evaluating the effects of AIS length on excitability, although their data is plotted alongside the other cells for comparison.

Dendrites: Based on the SBEM measurements, the surface area of bushy cell dendrites ranged from 2.43-3.23 (mean 2.76 SD 0.24) times the cell body area. Although bushy cell dendrites are short, they have a large diameter and consequently represent a substantial capacitance and conductive electrical load to the soma. The distribution of ion channels on GBC dendrites is not known. Qualitative immunostaining studies hint at the presence of HCN and low-voltage activated K^+ channels in at least the proximal GBC dendrites (***Koch et al., 2004***; ***Oertel et al., 2008***; ***Pál et al., 2005***; ***Wang et al., 1993***) (but see (***Perney and Kaczmarek, 1997***) where dendritic staining for the high-voltage activated channel $K_\upsilon 3.1$ is visible in stellate cell dendrites but not clearly visible in bushy cell dendrites in rat). However, with relatively few synaptic inputs and a limited role for active dendritic integration, it seems likely that voltage-gated ion channels may not be present at high densities in the dendrites. To account for the potential roles of dendritic channels, we therefore bracketed the conductance density range with three models. In each of these models, we decorated all types of dendritic compartments (proximal and distal dendrites, dendritic hubs, and dendritic swellings) with the same conductance densities. First, we used a model in which the densities of the channels in the dendrites were half of those in the soma (“Half-active”). The other two models addressed the extremes of possible channel densities. In the "Passive dendrite" model, the dendrites were uniformly decorated only with leak channels. In the "Active dendrite" model, the dendritic channel density was set uniformly to the somatic channel density for all channels. We refer to these models below as the “dendritic decoration configurations”.

Conductance Scaling: To properly scale the conductances into the somatic and dendritic compartments, we began with the low-voltage activated channel, g_{KLT}, which was measured under voltage clamp to be 80.9 (SE 16.7) nS in CBA mice (***Cao et al., 2007***). Next, to set a baseline value for the conductances, we first computed the mean somatic surface area from the SBEM mesh reconstructions (1352.1 (SD 164.9) μm^2, N=26 bushy cells), and for dendrites from the ten complete reconstructions (3799.5 (SD 435.8) μm^2, N=10 bushy cells). We then chose one cell whose somatic and dendritic areas were closest to the mean of these distributions GBC17: somatic surface area = 1357.6 μm^2; dendritic 3707.7 μm^2) to adjust g_{KLT}. The use of the "average" cell for this step was chosen to be consistent with the use of the mean value from ***Cao et al.*** (***2007***). We then adjusted g_{KLT} by computing the measured g_{KLT} from a voltage clamp protocol that mimicked experimental

measurements (steady-state currents with 100 ms pulses) with only g_{KLT} and a leak conductance inserted into the soma and dendrites for each of the three dendritic distribution assumptions. The soma was initially decorated with g_{KLT} channels at a fixed density of 2.769 mS/cm^2 based on a maximum conductance measured *in vitro* of 80 nS and a measured cell capacitance of 26 pF (***Cao et al., 2007***). However, this capacitance corresponds to a surface area of 2889 μm^2, which is more than twice the area of the measured somas, and is also significantly larger than other previously reported values (12 pF in acutely isolated neurons from guinea pig ***Rothman and Manis*** (***2003a***), 9-12 pF in rat pup bushy cells in slices (***Xu-Friedman and Regehr, 2008***), 9-22 pF in adult CBA mouse bushy cells, Xie and Manis, unpublished). To investigate this discrepancy, we measured the input capacitance (as seen by a somatic electrode) using voltage clamp simulations of the reconstructed cells. The voltage-clamp simulations were stepped at 5 μs, with 1 MΩ of uncompensated series resistance (R_s), to approximate the experimental situation that used 90% compensation of ~ 11 MΩR_s (***Cao et al., 2007***). Voltage steps from -80 to -90 mV were applied to models with only g_{KLT} and g_{leak} channels in the membrane, which yielded values of 13 pF, based on the fastest membrane charging time constant of ~ 15 μs, consistent with the studies cited above. This corresponds to a membrane area of 1460 μm^2, close to 1358 μm^2 measured for the soma area of this cell. We then ran additional voltage clamp simulations with steps from -80 to +20 mV to measure g_{KLT}. Total g_{KLT} was measured from the V-I relationship by fitting a Boltzmann function to the steady-state portion of the simulated currents (Figure 4–***Figure Supplement 3***), after correcting the membrane voltage for the drop across the series resistance, R_s. We iteratively made a linear prediction after each adjustment, by calculating the ratio between the measured conductance and the target value of 80 nS, and applied this to rescale g_{KLT}. Three to five iterations were adequate to arrive within 1% of the target value for g_{KLT} for each of the three dendritic decoration models for the test cell. Once g_{KLT} was determined, the ratio of g_{KLT} to the original model density was then calculated, and applied to all of the other channels at the soma, relative to their total cell conductances in the original models (based on the measurements and models of ***Xie and Manis*** (***2013b***) and measurements of ***Cao et al.*** (***2007***) (g_{KLT}: 80 nS; g_{Na}: 500 nS, g_{KHT}: 58 nS, g_H: 30 nS). The resulting densities, expressed in mS/cm^2 and listed in ***Table 2***, were used to decorate all reconstructed cells. Thus, with this approach, we anchored the model ion channel densities according to our morphological measurements to experimental measurements of g_{KLT} in the same species.

Dendrite Decoration Type			
Channel	Passive	Half-Active	Active
Na	60.2282	29.1104	20.1245
K_{HT}	3.4932	1.6884	1.1672
K_{LT}	4.8183	2.3288	1.6100
I_H	1.8068	0.8733	0.6037
$Leak$	0.1385	0.1385	0.1385

Table 2. Densities of channels in dendrites for 3 models spanning the likely range. All values are in mS/cm^2.

Auditory Nerve Inputs

Auditory nerve spike trains were computed using the *cochlea* package (***Rudnicki et al., 2015***), which is a Python wrapper around the widely-used model of ***Zilany et al.*** (***2014***). These simulations were incorporated into, and controlled by, *cnmodel* (***Manis and Campagnola, 2018***). Although the spike trains generated by these simulators were based on data from cat ANFs, the responses for mouse auditory nerve are quite similar, including irregular interspike intervals and the thresholds are similar in the central range of mouse hearing (***Taberner and Liberman, 2005***). Tonal acoustic stimuli were generated at 100 kHz with rise-fall times of 2.5 ms, and durations from 100 to 1000 ms. Clicks were generated as 100 μs pulses. The intensity was expressed in dB re $2x10^{-5}$ Pa (dB SPL). For

tonal stimuli, the frequency was set to 16 kHz to avoid low-frequency phase locking.

For some simulations, single-frequency tones at 16 kHz were amplitude modulated with a sinusoidal envelope (100% modulation) at frequencies between 50 and 1000 Hz. The depth of response modulation in ANFs is critically dependent on the average stimulus intensity as well as ANF SR (***Smith and Brachman, 1980***; ***Joris and Yin, 1992***; ***Joris et al., 2004***; ***Wang and Sachs, 1993***) and this sensitivity continues to be evident in cochlear nucleus neurons (***Moller, 1972***; ***Frisina et al., 1990***; ***Wang and Sachs, 1994***). We tested responses of the GBC models to SAM tones at an intensity that produces the highest synchronization in the high-spontaneous ANFs, 15 dB SPL, as well as at 30 dB SPL (see Figure 7–***Figure Supplement 1*** for the VS as a function of level in the ANF model). Testing was performed with only high-SR ANFs as inputs, consistent with observations in cats that GBCs are principally innervated by high-SR inputs (***Liberman, 1991***). Testing by including other SR groups would be expected to show higher synchronization at high sound levels (***Wang and Sachs, 1994***) as the medium and low SR fibers continue to synchronize to the envelope. However this would require making specific assumptions about the relationship between ASA and SR in order to appropriately assign SR groups. While recent data (***Wang et al., 2021***) suggests that some mouse GBCs may receive a greater proportion of medium and low-SR inputs than previously suggested for cat, we considered exploration of this dimension in the context of our simulations beyond the goals of the current study.

Endbulb Synapses

The endbulb synapses were modeled using a stochastic multisite release model, as described previously (***Xie and Manis, 2013b***; ***Manis and Campagnola, 2018***) and incorporated into *cnmodel*. Briefly, the release at each endbulb terminal is initiated when an action potential is generated by the auditory nerve model. Each synapse in the terminal then can release transmitter with a release probability, P_r in the range [0,1]. In the present simulations, the release probability was held fixed over time (it was not a function of the history of release event times). Whether a synapse will release or not is determined by drawing a random number from a uniform distribution, and if the number is less than P_r, then a release event is initiated. Transmitter time course was computed by convolution of a Dirac pulse with a bi-exponential function to mimic diffusion across the synaptic cleft, and the concentration time course at the postsynaptic receptors is computed by summing each release event with an ongoing cleft concentration. This glutamate transient then drives postsynaptic receptors. The postsynaptic receptors are based on fast AMPA receptors at the endbulbs in the nucleus magnocellularis of chicken (***Raman and Trussell, 1992***), with kinetics adjusted to match recorded currents at the mouse endbulb (***Xie and Manis, 2013b***). The AMPA receptor model conductances were also adjusted to match measurements of mEPSCs at mouse bushy cells. The receptor model includes desensitization, and the current through the receptor channels includes rectification of the current-voltage relationship by internal channel block from charged polyamines (***Woodhull, 1973***; ***Donevan and Rogawski, 1995***). The cleft glutamate also interacts with NMDA receptors in the synapse, based on the model of ***Kampa et al.*** (***2004***). NMDA receptor conductances were scaled to match the to the voltage-clamp measurements in ***Cao and Oertel*** (***2010***). Each release site of the terminal is treated independently, ignoring the possible consequences of transmitter "spillover". A time-dependent increase in release latency is observed experimentally (see ***Manis and Campagnola*** (***2018***)), but was disabled in the simulations reported here because it has not been fully characterized. The number of synapses at each endbulb is calculated using the ASA and average synapse density as determined from the SBEM data. For all simulations here, the density was 0.7686 $\text{synapses}/\mu\text{m}^2$.

Spike Detection

Spikes in bushy neurons are often small and of variable amplitude, and the EPSPs can be large (10's of mV). Simple approaches using a fixed voltage or slope threshold are not reliable for discerning spikes from EPSPs with somatic recordings. We, therefore, used the method of ***Hight and Kalluri*** (***2016***) to detect spikes based on the width of the peak and the rising and falling slopes. Spike detection parameters were set exactly as in ***Hight and Kalluri*** (***2016***).

Cross Correlation

Correlations between postsynaptic spikes and the input spike trains were calculated as cross-correlations against each of the independent inputs to a cell. The correlations were calculated using the "correlogram" routine from Brian1.4, and were taken with respect to the time of the postsynaptic spike. Presynaptic spikes occuring after the postsynaptic spike are not shown. The result is presented in Hz (spikes/second), as the rate of coincidences between presynaptic spikes from each input and the postsynaptic spike in each time bin, at a time resolution of 0.1 ms.

Rate modulation transfer function

The rate modulation transfer function (rMTF) was calculated as described in ***Walton et al.*** (***2002***). The rMTF was calculated as the average rate at each modulation frequency for spikes starting 250 ms after stimulus onset and ending at the time corresponding to the starting phase during a 1-second SAM tone. The window for the rate calculation set in this way to be sure that all frequencies included complete modulation cycles.

Entrainment

Entrainment was calculated from the interspike interval distribution as described in ***Joris and Yin*** (***1992***) and ***Rudnicki and Hemmert*** (***2017***), with one modification. At low modulation frequencies (50 and 100 Hz), multiple spikes could occur per modulation cycle, both in the auditory nerve and in the bushy cells. This led to low values of entrainment, even though the cells were firing on most cycles. To minimize this confound, we set the lower bound of included interspike intervals to $0.5/f_{mod}$, rather than 0 (the upper bound remained $1.5/f_{mod}$). This does not entirely eliminate the presence of spontaneous or multiple spikes contributing to the entrainment index at low frequencies, but it reduces the chances that they will be included. The ISI distribution was derived from spikes starting 250 ms after tone onset and ending at the longest interval that fell within a complete cycle (determined from the starting phase) during a 1-second SAM tone.

Spike Timing Analysis

Vector strength was computed using the standard equations (***Goldberg and Brown, 1969***), using spikes taken from the last 750 ms of 100 repetitions of 1-s long SAM stimuli. To estimate the error of the vector strength calculation, vector strength was calculated for 10 groups of 10 consecutive repetitions, and the mean and SD computed. Responses with fewer than 50 spikes were not calculated (this appeared only for GBC10 for the configuration with only the largest input active). Vector strength for ANFs was calculated across all spikes of all ANFs connected to the postsynaptic cell. We also calculated shuffled autocorrelations using the method of ***Louage et al.*** (***2004***) for both SAM stimuli and click stimuli. These calculations were verified to reproduce Fig 2. of ***Louage et al.*** (***2004***).

Action Potential Current Threshold Measurement

The minimum current required to elicit an action potential (rheobase) was measured in response to a brief current pulse (20 ms) of variable amplitude. An iterative binary search procedure was used to identify the threshold, with a terminal step size of 1 pA. Ten to twenty iterations were sufficient to resolve threshold to this precision.

Modeling Software Environment

The entire set of simulations were controlled and analyzed by additional Python (V3.7.8, 3.8.6, 3.9.1, 3.10.0) scripts (*VCNModel*). *VCNModel* controlled simulations and organized simulation result files, read cell morphology files into NEURON ***Carnevale and Hines*** (***2006***), and decorated the cells with channels using tools from *cnmodel* (www.github.com/cnmodel). Parametric simulations were managed by shell scripts (bash, zsh) that called the Python scripts. Simulations reported here were run with NEURON 7.7, 7.8.1, 8.0 and 8.1 on an 8-core MacPro (2013), a MacBook Pro (2017), and a 20-core MacStudio (2022); there was no difference in the results of the underlying auditory nerve, bushy cell, or synapse models as determined by the unit tests in *cnmodel* for any versions of NEURON, Python, or hardware. The anatomical structure of the reconstructions was defined by the NEURON HOC files, and the channel densities were set from text (human readable) tables managed in *cnmodel*. The *VCNModel* scripts computed scaling of cell areas (inflation of the SWC/HOC files to match the mesh areas), control of "experiments" (for example, only activating selected AN terminals), data management, plotting, and analysis. Analysis of current voltage relationships and spike detection was handled by the *ephys* package (www.github.com/pbmanis/ephys). Plots were generated using matplotlib (versions 3.2.0-3.5.2) and seaborn (version 0.11.2).

Data and Code Availability

Data (Excel worksheets) and code (Matlab R2022a) for graphs in Figures 1, 2, 5, 6 and 8H are available at www.github.com/gaspirou/pub_file_share. Simulation source code, documentation, and a shell script to set up a working environment is available at www.github.com/pbmanis/VCNModel ("release" branch). Simulation result files used to generate figures 3, 4, 7 and 8I-M and their associated supplemental figures have been uploaded to *Dryad*, and can be accessed at www.dryad.org for review. Code and data for Figure 2, Supplement 1 is included in *VCNModel*. Simulation figures and figure panels can be generated using the *DataTables* script in the *VCNModel* package after downloading the simulation result files.

Acknowledgments

We thank Dr. Ken Hutson for comments on the manuscript, the many student tracers who contributed to cell segmentation, Thomas Deerinck (UCSD) for development of tissue staining protocols and managing image acquisition, and Lyra Gaboardi for movie production. We also thank the reviewers of this manuscript for their very constructive comments. This work was supported by NIH/NIDCD grant R01 DC015901, "The Nanoscale Connectome of the Cochlear Nucleus" (GAS, PBM, MHE). Development of the modeling platform (*cnmodel*, and extensions that implemented decorations of dendrites and various manipulations of the cells wer supported by NIH/NIDCD grant R01 DC004551, "Cellular Mechanisms of Auditory Information Processing" (PBM). SBEM data acquisition was performed at the National Center for Microscopy and Imaging Research, with support from NIH/NINDS grant U24 NS120055 (MHE). Deposition and management of acquired raw and derived EM data within the Cell Image Library was further supported by NIH/NIGMS grant R01GM82949 (MHE).

Additional Information

Funding

Funder	Grant Reference Number	Author
National Institute on Deafness and other Communication Disorders	R01 DC015901	George A. Spirou
National Institute on Deafness and other Communication Disorders	R01 DC004551	Paul B. Manis
National Institute of Neurological Diseases and Stroke	U24 NS120055	Mark H. Ellisman
National Institute of General Medical Sciences	R01 GM082949	Mark H. Ellisman
The funding agencies had no role in study design, data collection and interpretation, or the decision to submit this work for publication		

Ethics

George A. Spirou is the Chief Scientific Officer of IstoVisio, Inc., which makes the syGlass software used to visualize the EM volume and reconstruct the neurons. Carolyna Y. Alves-Pinto, Sean Carr, Mariah Dawson, Mark Ellisman, Matthew Kersting, Paul B. Manis, and Bayan Razzaq have no declarations or affiliations to report.

Author Contributions

George Spirou: Conceptualization, Formal analysis, Software, Investigation, Visualization, Methodology, Funding acquisition, Project administration, Writing - reviewing and editing. Matthew Kersting: Formal analysis, Software, Investigation, Visualization, Writing (portions of original draft). Carolyna Y. Alves-Pinto, Sean Carr, Mariah Dawson, and Bayan Razzaq contributed Formal analysis, Investigation, Visualization. Mark Ellisman: Investigation, Methodology, Visualization. Paul Manis: Conceptualization, Formal analysis, Simulations, Software, Investigation, Visualization, Methodology, Funding acquisition, Writing - reviewing and editing. Portions of this work are derived from Matthew Kersting's Master's thesis in Medical Engineering (University of South Florida).

Author ORCIDs

George A. Spirou https://orcid.org/0000-0001-7677-3585
Matthew Kersting https://orcid.org/0000-0002-7632-1762
Sean Carr https://orcid.org/0000-0002-6757-9104
Bayan Razzaq https://orcid.org/0000-0002-1307-8531
Carolyna Y. Alves-Pinto https://orcid.org/0000-0001-6735-045X
Mark H. Ellisman https://orcid.org/0000-0001-8893-8455
Paul B. Manis https://orcid.org/0000-0003-0131-8961

References

Abbott LF, Bock DD, Callaway EM, Denk W, Dulac C, Fairhall AL, Fiete I, Harris KM, Helmstaedter M, Jain V, Kasthuri N, LeCun Y, Lichtman JW, Littlewood PB, Luo L, Maunsell JHR, Reid RC, Rosen BR, Rubin GM, Sejnowski TJ, et al. The Mind of a Mouse. Cell. 2020 09; 182(6):1372–1376. doi: 10.1016/j.cell.2020.08.010.

Anniko M, Arnesen AR. Cochlear nerve topography and fiber spectrum in the pigmented mouse. Arch Otorhinolaryngol. 1988; 245(3):155–159.

Ashida G, Heinermann HT, Kretzberg J. Neuronal population model of globular bushy cells covering unit-to-unit variability. PLoS Comput Biol. 2019 12; 15(12):e1007563. doi: 10.1371/journal.pcbi.1007563.

Bae JA, Baptiste M, Bodor AL, Brittain D, Buchanan J, Bumbarger DJ, Castro MA, Celii B, Cobos E, Collman F, da Costa NM, Dorkenwald S, Elabbady L, Fahey PG, Fliss T, Froudarakis E, Gager J, Gamlin C, Halageri A, Hebditch J, et al. Functional connectomics spanning multiple areas of mouse visual cortex. bioRxiv. 2021; https://www.biorxiv.org/content/early/2021/08/09/2021.07.28.454025, doi: 10.1101/2021.07.28.454025.

Bender KJ, Trussell LO. The physiology of the axon initial segment. Annu Rev Neurosci. 2012; 35:249–65. doi: 10.1146/annurev-neuro-062111-150339.

Berry KP, Nedivi E. Experience-Dependent Structural Plasticity in the Visual System. Annu Rev Vis Sci. 2016 Oct; 2:17–35. doi: 10.1146/annurev-vision-111815-114638.

Blackburn CC, Sachs MB. Classification of unit types in the anteroventral cochlear nucleus: PST histograms and regularity analysis. J Neurophysiol. 1989; 62(6):1303–1329.

Bock DD, Lee WCA, Kerlin AM, Andermann ML, Hood G, Wetzel AW, Yurgenson S, Soucy ER, Kim HS, Reid RC. Network anatomy and in vivo physiology of visual cortical neurons. Nature. 2011 Mar; 471(7337):177–82. doi: 10.1038/nature09802.

Bodian D. An electron microscopic characterization of classes of synaptic vesicles by means of controlled aldehyde fixation. J Cell Biol. 1970 Jan; 44(1):115–24. doi: 10.1083/jcb.44.1.115.

Bourk TR. Electrical responses of neural units in the anteroventral cochlear nucleus of the cat. Ph.D., Massachussetts Institute of Technology; 1976.

Boyd IA, Kalu KU. Scaling factor relating conduction velocity and diameter for myelinated afferent nerve fibres in the cat hind limb. J Physiol. 1979 Apr; 289:277–97. doi: 10.1113/jphysiol.1979.sp012737.

Brawer JR, Morest DK, Kane EC. The neuronal architecture of the cochlear nucleus of the cat. J Comp Neurol. 1974; 155(3):251–300.

Briggman KL, Bock DD. Volume electron microscopy for neuronal circuit reconstruction. Curr Opin Neurobiol. 2012 Feb; 22(1):154–61. doi: 10.1016/j.conb.2011.10.022.

Brill MH, Waxman SG, Moore JW, Joyner RW. Conduction velocity and spike configuration in myelinated fibres: computed dependence on internode distance. J Neurol Neurosurg Psychiatry. 1977 Aug; 40(8):769–74. doi: 10.1136/jnnp.40.8.769.

Brownell WE, Manis PB. Structures, Mechanisms and Energetics in Temporal Processing. In: Popper AN, Fay RR, editors. Perspectives on Auditory Research, vol. 50 of Springer Handbook of Auditory Research Springer-Verlag; 2014. p. 9–44.

Burda H, Ballast L, Bruns V. Cochlea in old world mice and rats (Muridae). J Morphol. 1988 Dec; 198(3):269–85. doi: 10.1002/jmor.1051980303.

Cai H, Dent ML. Best sensitivity of temporal modulation transfer functions in laboratory mice matches the amplitude modulation embedded in vocalizations. J Acoust Soc Am. 2020 01; 147(1):337. doi: 10.1121/10.0000583.

Cajal SRY. XXVIII. The Acoustic Nevre: Its cochlear branch or cochlear nerve. In: Histology of the nervous system of man and vertebrates, vol. I U.S. Department of Commerce, Springfield, VA: National Technical Information Service; 1971. p. 774–838.

Camarero G, Avendano C, Fernandez-Moreno C, Villar A, Contreras J, de Pablo F, Pichel JG, Varela-Nieto I. Delayed inner ear maturation and neuronal loss in postnatal Igf-1-deficient mice. J Neurosci. 2001 Oct; 21(19):7630–41.

Campagnola L, Manis PB. A map of functional synaptic connectivity in the mouse anteroventral cochlear nucleus. J Neurosci. 2014 Feb; 34(6):2214–30. doi: 10.1523/JNEUROSCI.4669-13.2014.

Cannon RC, Turner DA, Pyapali GK, Wheal HV. An on-line archive of reconstructed hippocampal neurons. J Neurosci Methods. 1998 Oct; 84(1-2):49–54. doi: 10.1016/s0165-0270(98)00091-0.

Cant NB, Morest DK. Axons from non-cochlear sources in the anteroventral cochlear nucleus of the cat. A study with the rapid Golgi method. Neuroscience. 1978; 3(11):1003–1029.

Cant NB, Morest DK. The bushy cells in the anteroventral cochlear nucleus of the cat. A study with the electron microscope. Neuroscience. 1979; 4(12):1925–1945.

Cant NB, Morest DK. Organization of the neurons in the anterior division of the anteroventral cochlear nucleus of the cat. Light-microscopic observations. Neuroscience. 1979; 4(12):1909–1923.

Cao XJ, Oertel D. Auditory nerve fibers excite targets through synapses that vary in convergence, strength, and short-term plasticity. J Neurophysiol. 2010 Nov; 104(5):2308–20. doi: 10.1152/jn.00451.2010.

Cao XJ, Oertel D. The magnitudes of hyperpolarization-activated and low-voltage-activated potassium currents co-vary in neurons of the ventral cochlear nucleus. J Neurophysiol. 2011 Aug; 106(2):630–40. doi: 10.1152/jn.00015.2010.

Cao XJ, Shatadal S, Oertel D. Voltage-sensitive conductances of bushy cells of the Mammalian ventral cochlear nucleus. J Neurophysiol. 2007 Jun; 97(6):3961–75. doi: 10.1152/jn.00052.2007.

Carnevale NT, Hines ML. The NEURON book. Cambridge, UK: Cambridge University Press; 2006. http://www.loc.gov/catdir/enhancements/fy0661/2006277066-d.html.

Caspary DM, Backoff PM, Finlayson PG, Palombi PS. Inhibitory inputs modulate discharge rate within frequency receptive fields of anteroventral cochlear nucleus neurons. J Neurophysiol. 1994 Nov; 72(5):2124–33. doi: 10.1152/jn.1994.72.5.2124.

Caspary DM, Backoff PM, Finlayson PG, Palombi PS. Inhibitory inputs modulate discharge rate within frequency receptive fields of anteroventral cochlear nucleus neurons. J Neurophysiol. 1994; 72(5):2124–2133.

Consortium TM, Bae JA, Baptiste M, Bishop CA, Bodor AL, Brittain D, Buchanan J, Bumbarger DJ, Castro MA, Celii B, Cobos E, Collman F, da Costa NM, Dorkenwald S, Elabbady L, Fahey PG, Fliss T, Froudarakis E, Gager J, Gamlin C, et al. Functional connectomics spanning multiple areas of mouse visual cortex. bioRxiv. 2023; https://www.biorxiv.org/content/early/2023/04/19/2021.07.28.454025, doi: 10.1101/2021.07.28.454025.

Cook SJ, Jarrell TA, Brittin CA, Wang Y, Bloniarz AE, Yakovlev MA, Nguyen KCQ, Tang LTH, Bayer EA, Duerr JS, Bülow HE, Hobert O, Hall DH, Emmons SW. Whole-animal connectomes of both Caenorhabditis elegans sexes. Nature. 2019 07; 571(7763):63–71. doi: 10.1038/s41586-019-1352-7.

Cooper NP, Robertson D, Yates GK. Cochlear nerve fiber responses to amplitude-modulated stimuli: variations with spontaneous rate and other response characteristics. J Neurophysiol. 1993; 70(1):370–386.

Ding Z, Fahey PG, Papadopoulos S, Wang EY, Celii B, Papadopoulos C, Kunin AB, Chang A, Fu J, Ding Z, Patel S, Ponder K, Muhammad T, Bae JA, Bodor AL, Brittain D, Buchanan J, Bumbarger DJ, Castro MA, Cobos E, et al. Functional connectomics reveals general wiring rule in mouse visual cortex. bioRxiv. 2023; https://www.biorxiv.org/content/early/2023/03/30/2023.03.13.531369, doi: 10.1101/2023.03.13.531369.

Donevan SD, Rogawski MA. Intracellular polyamines mediate inward rectification of Ca(2+)-permeable alpha-amino-3-hydroxy-5-methyl-4-isoxazolepropionic acid receptors. Proc Natl Acad Sci U S A. 1995 Sep; 92(20):9298–302. doi: 10.1073/pnas.92.20.9298.

Dreyer A, Delgutte B. Phase locking of auditory-nerve fibers to the envelopes of high-frequency sounds: implications for sound localization. J Neurophysiol. 2006 Nov; 96(5):2327–41. doi: 10.1152/jn.00326.2006.

Ferri SL, Flanagan-Cato LM. Oxytocin and dendrite remodeling in the hypothalamus. Horm Behav. 2012 Mar; 61(3):251–8. doi: 10.1016/j.yhbeh.2012.01.012.

Francis HW, Manis PB. Effects of deafferentation on the electrophysiology of ventral cochlear nucleus neurons. Hearing Res. 2000; 149:91–105.

Franken TP, Bondy BJ, Haimes DB, Goldwyn JH, Golding NL, Smith PH, Joris PX. Glycinergic axonal inhibition subserves acute spatial sensitivity to sudden increases in sound intensity. Elife. 2021 06; 10. doi: 10.7554/eLife.62183.

Frisina RD, Smith RL, Chamberlain SC. Encoding of amplitude modulation in the gerbil cochlear nucleus: I. A hierarchy of enhancement. Hearing Res. 1990; 44(2-3):99–122.

Furusawa K, Emoto K. Scrap and Build for Functional Neural Circuits: Spatiotemporal Regulation of Dendrite Degeneration and Regeneration in Neural Development and Disease. Front Cell Neurosci. 2020; 14:613320. doi: 10.3389/fncel.2020.613320.

Gai Y, Carney LH. Influence of inhibitory inputs on rate and timing of responses in the anteroventral cochlear nucleus. J Neurophysiol. 2008 Mar; 99(3):1077–95. doi: 10.1152/jn.00708.2007.

Gardner SM, Trussell LO, Oertel D. Time course and permeation of synaptic AMPA receptors in cochlear nuclear neurons correlate with input. J Neurosci. 1999; 19:87231–8729.

van Gisbergen JA, Grashuis JL, Johannesma Pu, Vendrik AJ. Statistical analysis and interpretation of the initial response of cochlear nucleus neurons to tone bursts. Exp Brain Res. 1975; 23(4):407–423.

Goldberg JM, Brown PB. Response of binaural neurons of dog superior olivary complex to dichotic tonal stimuli: some physiological mechanisms of sound localization. J Neurophysiol. 1969; 32(4):613–636.

Gómez-Nieto R, Rubio ME. A bushy cell network in the rat ventral cochlear nucleus. J Comp Neurol. 2009 Oct; 516(4):241–63. doi: 10.1002/cne.22139.

Grubb MS, Burrone J. Activity-dependent relocation of the axon initial segment fine-tunes neuronal excitability. Nature. 2010 Jun; 465(7301):1070–4. doi: 10.1038/nature09160.

Hackney CM, Osen KK, Kolston J. Anatomy of the cochlear nuclear complex of guinea pig. Anat Embryol (Berl). 1990; 182(2):123–149.

Harrison JM, Irving R. Ascending connections of the anterior ventral cochlear nucleus in the rat. J Comp Neurol. 1966 Jan; 126(1):51–63. doi: 10.1002/cne.901260105.

Held H. Die centrale Gehörleitung. Arch Anat Physiol, Anat Abt. 1893; p. 201–248.

Hight AE, Kalluri R. A biophysical model examining the role of low-voltage-activated potassium currents in shaping the responses of vestibular ganglion neurons. J Neurophysiol. 2016 08; 116(2):503–21. doi: 10.1152/jn.00107.2016.

Holcomb PS, Hoffpauir BK, Hoyson MC, Jackson DR, Deerinck TJ, Marrs GS, Dehoff M, Wu J, Ellisman MH, Spirou GA. Synaptic inputs compete during rapid formation of the calyx of Held: a new model system for neural development. J Neurosci. 2013 Aug; 33(32):12954–69. doi: 10.1523/JNEUROSCI.1087-13.2013.

Hu W, Tian C, Li T, Yang M, Hou H, Shu Y. Distinct contributions of Na(v)1.6 and Na(v)1.2 in action potential initiation and backpropagation. Nat Neurosci. 2009 Aug; 12(8):996–1002. doi: 10.1038/nn.2359.

Huang M, Volgushev M, Wolf F. A small fraction of strongly cooperative sodium channels boosts neuronal encoding of high frequencies. PLoS One. 2012; 7(5):e37629. doi: 10.1371/journal.pone.0037629.

Ilin V, Malyshev A, Wolf F, Volgushev M. Fast computations in cortical ensembles require rapid initiation of action potentials. J Neurosci. 2013 Feb; 33(6):2281–92. doi: 10.1523/JNEUROSCI.0771-12.2013.

Jackson D, Holcomb P, Ellisman M, Spirou G. Two types of somatic spines provide sites for intercellular signaling during calyx of Held growth and maturation. Synapse. 2021 Mar; 75(3):e22189. doi: 10.1002/syn.22189.

Jing J, Hu M, Ngodup T, Ma Q, Lau SNN, Ljungberg C, McGinley MJ, Trussell LO, Jiang X. Comprehensively defining cellular specializations for initiating parallel auditory pathways in the mouse cochlear nucleus. bioRxiv. 2023; https://www.biorxiv.org/content/early/2023/05/16/2023.05.15.539065, doi: 10.1101/2023.05.15.539065.

Joris PX, Carney LH, Smith PH, Yin TC. Enhancement of neural synchronization in the anteroventral cochlear nucleus. I. Responses to tones at the characteristic frequency. J Neurophysiol. 1994 Mar; 71(3):1022–36. doi: 10.1152/jn.1994.71.3.1022.

Joris PX, Schreiner CE, Rees A. Neural processing of amplitude-modulated sounds. Physiol Rev. 2004 Apr; 84(2):541–77. doi: 10.1152/physrev.00029.2003.

Joris PX, Smith PH, Yin TC. Enhancement of neural synchronization in the anteroventral cochlear nucleus. II. Responses in the tuning curve tail. J Neurophysiol. 1994 Mar; 71(3):1037–51. doi: 10.1152/jn.1994.71.3.1037.

Joris PX, Yin TC. Responses to amplitude-modulated tones in the auditory nerve of the cat. J Acoust Soc Am. 1992; 91(1):215–232.

Kampa BM, Clements J, Jonas P, Stuart GJ. Kinetics of Mg2+ unblock of NMDA receptors: implications for spike-timing dependent synaptic plasticity. J Physiol. 2004 Apr; 556(Pt 2):337–45. doi: 10.1113/jphysiol.2003.058842.

Kaphzan H, Buffington SA, Jung JI, Rasband MN, Klann E. Alterations in intrinsic membrane properties and the axon initial segment in a mouse model of Angelman syndrome. J Neurosci. 2011 Nov; 31(48):17637–48. doi: 10.1523/JNEUROSCI.4162-11.2011.

Keine C, Rübsamen R. Inhibition shapes acoustic responsiveness in spherical bushy cells. J Neurosci. 2015 Jun; 35(22):8579–92. doi: 10.1523/JNEUROSCI.0133-15.2015.

Keine C, Rübsamen R, Englitz B. Inhibition in the auditory brainstem enhances signal representation and regulates gain in complex acoustic environments. Elife. 2016 11; 5. doi: 10.7554/eLife.19295.

Kim EJ, Feng C, Santamaria F, Kim JH. Impact of Auditory Experience on the Structural Plasticity of the AIS in the Mouse Brainstem Throughout the Lifespan. Front Cell Neurosci. 2019; 13:456. doi: 10.3389/fncel.2019.00456.

Koch U, Braun M, Kapfer C, Grothe B. Distribution of HCN1 and HCN2 in rat auditory brainstem nuclei. Eur J Neurosci. 2004 Jul; 20(1):79–91. doi: 10.1111/j.0953-816X.2004.03456.x.

Koert E, Kuenzel T. Small dendritic synapses enhance temporal coding in a model of cochlear nucleus bushy cells. J Neurophysiol. 2021 03; 125(3):915–937. doi: 10.1152/jn.00331.2020.

Kole MHP, Ilschner SU, Kampa BM, Williams SR, Ruben PC, Stuart GJ. Action potential generation requires a high sodium channel density in the axon initial segment. Nat Neurosci. 2008 Feb; 11(2):178–86. doi: 10.1038/nn2040.

Kopp-Scheinpflug C, Fuchs K, Lippe WR, Tempel BL, Rübsamen R. Decreased temporal precision of auditory signaling in Kcna1-null mice: an electrophysiological study in vivo. J Neurosci. 2003 Oct; 23(27):9199–207.

Kuba H. Structural tuning and plasticity of the axon initial segment in auditory neurons. J Physiol. 2012 Nov; 590(22):5571–9. doi: 10.1113/jphysiol.2012.237305.

Kuba H, Ishii TM, Ohmori H. Axonal site of spike initiation enhances auditory coincidence detection. Nature. 2006 Dec; 444(7122):1069–72. doi: 10.1038/nature05347.

Kuba H, Oichi Y, Ohmori H. Presynaptic activity regulates Na(+) channel distribution at the axon initial segment. Nature. 2010 Jun; 465(7301):1075–8. doi: 10.1038/nature09087.

Kuba H, Yamada R, Ishiguro G, Adachi R. Redistribution of Kv1 and Kv7 enhances neuronal excitability during structural axon initial segment plasticity. Nat Commun. 2015 Nov; 6:8815. doi: 10.1038/ncomms9815.

Lam SS, Martell JD, Kamer KJ, Deerinck TJ, Ellisman MH, Mootha VK, Ting AY. Directed evolution of APEX2 for electron microscopy and proximity labeling. Nat Methods. 2015 Jan; 12(1):51–4. doi: 10.1038/nmeth.3179.

Lauer AM, Connelly CJ, Graham H, Ryugo DK. Morphological characterization of bushy cells and their inputs in the laboratory mouse (Mus musculus) anteroventral cochlear nucleus. PLoS One. 2013; 8(8):e73308. doi: 10.1371/journal.pone.0073308.

Lee CT, Laughlin JG, Angliviel de La Beaumelle N, Amaro RE, McCammon JA, Ramamoorthi R, Holst M, Rangamani P. 3D mesh processing using GAMer 2 to enable reaction-diffusion simulations in realistic cellular geometries. PLoS Comput Biol. 2020 Apr; 16(4):e1007756. doi: 10.1371/journal.pcbi.1007756.

Lee CT, Laughlin JG, Moody JB, Amaro RE, McCammon JA, Holst M, Rangamani P. An Open-Source Mesh Generation Platform for Biophysical Modeling Using Realistic Cellular Geometries. Biophys J. 2020 03; 118(5):1003–1008. doi: 10.1016/j.bpj.2019.11.3400.

Liberman MC. Central projections of auditory-nerve fibers of differing spontaneous rate. I: Anteroventral cochlear nucleus. J Comp Neurol. 1991; 313(2):240–258.

Lorincz A, Nusser Z. Cell-type-dependent molecular composition of the axon initial segment. J Neurosci. 2008 Dec; 28(53):14329–40. doi: 10.1523/JNEUROSCI.4833-08.2008.

Louage DHG, van der Heijden M, Joris PX. Temporal properties of responses to broadband noise in the auditory nerve. J Neurophysiol. 2004 May; 91(5):2051–65. doi: 10.1152/jn.00816.2003.

Louage DHG, van der Heijden M, Joris PX. Enhanced temporal response properties of anteroventral cochlear nucleus neurons to broadband noise. J Neurosci. 2005 Feb; 25(6):1560–70. doi: 10.1523/JNEUROSCI.4742-04.2005.

Low T K Tan. Model simplification using vertex-clustering. In: *Proceedings of the 1997 Symposium on Interactive 3D Graphics* New York, NY, USA: Association for Computing Machinery; 1997. p. 75–82.

Manis PB, Campagnola L. A biophysical modelling platform of the cochlear nucleus and other auditory circuits: From channels to networks. Hear Res. 2018 03; 360:76–91. doi: 10.1016/j.heares.2017.12.017.

Manis PB, Marx SO. Outward currents in isolated ventral cochlear nucleus neurons. J Neurosci. 1991; 11(9):2865–2880.

Moller AR. Coding of amplitude and frequency modulated sounds in the cochlear nucleus of the rat. Acta Physiol Scand. 1972; 86(2):223–238.

Ngodup T, Romero GE, Trussell LO. Identification of an inhibitory neuron subtype, the L-stellate cell of the cochlear nucleus. Elife. 2020 11; 9. doi: 10.7554/eLife.54350.

Nicol MJ, Walmsley B. Ultrastructural basis of synaptic transmission between endbulbs of Held and bushy cells in the rat cochlear nucleus. J Physiol. 2002 Mar; 539(Pt 3):713–23. doi: 10.1113/jphysiol.2001.012972.

Lorente de Nó R. Anatomy of the eighth nerve. III. General plan of structure of the primary cochlear nuclei. Laryngoscope. 1933; 33:327–350.

Lorente de Nó R. The Primary Acoustic Nuclei. New York, NY: Raven Press; 1981.

Oertel D, Shatadal S, Cao XJ. In the ventral cochlear nucleus Kv1.1 and subunits of HCN1 are colocalized at surfaces of neurons that have low-voltage-activated and hyperpolarization-activated conductances. Neuroscience. 2008 Jun; 154(1):77–86. doi: 10.1016/j.neuroscience.2008.01.085.

von der Ohe CG, Darian-Smith C, Garner CC, Heller HC. Ubiquitous and temperature-dependent neural plasticity in hibernators. J Neurosci. 2006 Oct; 26(41):10590–8. doi: 10.1523/JNEUROSCI.2874-06.2006.

Osen KK. Cytoarchitecture of the cochlear nuclei in the cat. J Comp Neurol. 1969; 136(4):453–484.

Ostapoff EM, Morest DK. Synaptic organization of globular bushy cells in the ventral cochlear nucleus of the cat: a quantitative study. J Comp Neurol. 1991; 314:598–613.

Pál B, Pór A, Pocsai K, Szücs G, Rusznák Z. Voltage-gated and background K+ channel subunits expressed by the bushy cells of the rat cochlear nucleus. Hear Res. 2005 Jan; 199(1-2):57–70. doi: 10.1016/j.heares.2004.07.020.

Palmer AR, Russell IJ. Phase-locking in the cochlear nerve of the guinea-pig and its relation to the receptor potential of inner hair-cells. Hearing Res. 1986; 24(1):1–15.

Perez-Nieves N, Leung VCH, Dragotti PL, Goodman DFM. Neural heterogeneity promotes robust learning. Nat Commun. 2021 10; 12(1):5791. doi: 10.1038/s41467-021-26022-3.

Perney TM, Kaczmarek LK. Localization of a high threshold potassium channel in the rat cochlear nucleus. J Comp Neurol. 1997; 386(2):178–202.

Peters A, Palay SL, Webster Hd. The fine structure of the nervous system: neurons and their supporting cells. 3rd ed ed. New York: Oxford University Press; 1991. http://www.loc.gov/catdir/enhancements/fy0604/90014201-d.html.

Petitpré C, Wu H, Sharma A, Tokarska A, Fontanet P, Wang Y, Helmbacher F, Yackle K, Silberberg G, Hadjab S, Lallemend F. Neuronal heterogeneity and stereotyped connectivity in the auditory afferent system. Nat Commun. 2018 09; 9(1):3691. doi: 10.1038/s41467-018-06033-3.

Raman IM, Trussell LO. The kinetics of the response to glutamate and kainate in neurons of the avian cochlear nucleus. Neuron. 1992; 9(1):173–186.

Rhode WS, Greenberg S. Encoding of amplitude modulation in the cochlear nucleus of the cat. J Neurophysiol. 1994; 71(5):1797–1825.

Roos MJ, May BJ. Classification of unit types in the anteroventral cochlear nucleus of laboratory mice. Hear Res. 2012 Jul; 289(1-2):13–26. doi: 10.1016/j.heares.2012.04.019.

Rothman JS, Young ED, Manis PB. Convergence of auditory nerve fibers onto bushy cells in the ventral cochlear nucleus: implications of a computational model. J Neurophysiol. 1993 Dec; 70(6):2562–83.

Rothman JS, Manis PB. Differential expression of three distinct potassium currents in the ventral cochlear nucleus. J Neurophysiol. 2003 Jun; 89(6):3070–82. doi: 10.1152/jn.00125.2002.

Rothman JS, Manis PB. Kinetic analyses of three distinct potassium conductances in ventral cochlear nucleus neurons. J Neurophysiol. 2003 Jun; 89(6):3083–96. doi: 10.1152/jn.00126.2002.

Rothman JS, Manis PB. The roles potassium currents play in regulating the electrical activity of ventral cochlear nucleus neurons. J Neurophysiol. 2003 Jun; 89(6):3097–113. doi: 10.1152/jn.00127.2002.

Rothman JS, Young ED. Enhancement of neural synchronization in computational models of ventral cochlear nucleus bushy cells. Aud Neurosci. 1996; 2:47–62.

Rouiller EM, Cronin-Schreiber R, Fekete DM, Ryugo DK. The central projections of intracellularly labeled auditory nerve fibers in cats: an analysis of terminal morphology. J Comp Neurol. 1986; 249(2):261–278.

Rowland KC, Irby NK, Spirou GA. Specialized synapse-associated structures within the calyx of Held. J Neurosci. 2000 Dec; 20(24):9135–44.

Rudnicki M, Hemmert W. High Entrainment Constrains Synaptic Depression Levels of an In vivo Globular Bushy Cell Model. Front Comput Neurosci. 2017; 11:16. doi: 10.3389/fncom.2017.00016.

Rudnicki M, Schoppe O, Isik M, Völk F, Hemmert W. Modeling auditory coding: from sound to spikes. Cell Tissue Res. 2015 Jul; 361(1):159–75. doi: 10.1007/s00441-015-2202-z.

Ryugo DK, Fekete DM. Morphology of primary axosomatic endings in the anteroventral cochlear nucleus of the cat: a study of the endbulbs of Held. J Comp Neurol. 1982; 210(3):239–257.

Ryugo DK, Pongstaporn T, Huchton DM, Niparko JK. Ultrastructural analysis of primary endings in deaf white cats: Morphologic alterations in endbulbs of Held. J Comp Neurol. 1997; 385:230–244.

Ryugo DK, Sento S. Synaptic connections of the auditory nerve in cats: relationship between endbulbs of Held and spherical bushy cells. J Comp Neurol. 1991; 305:35–48.

Ryugo DK, Wright DD, Pongstaporn T. Ultrastructural Analysis of Synaptic Endings of Auditory Nerve Fibers in Cats: Correlations with Spontaneous Discharge Rate. In: *The Mammalian Cochlear Nuclei: Organization and Function*; 1993. p. 65–80.

Scheffer LK, Xu CS, Januszewski M, Lu Z, Takemura SY, Hayworth KJ, Huang GB, Shinomiya K, Maitlin-Shepard J, Berg S, Clements J, Hubbard PM, Katz WT, Umayam L, Zhao T, Ackerman D, Blakely T, Bogovic J, Dolafi T, Kainmueller D, et al. A connectome and analysis of the adult Drosophila central brain. Elife. 2020 09; 9. doi: 10.7554/eLife.57443.

Schneider-Mizell CM, Bodor AL, Collman F, Brittain D, Bleckert A, Dorkenwald S, Turner NL, Macrina T, Lee K, Lu R, Wu J, Zhuang J, Nandi A, Hu B, Buchanan J, Takeno MM, Torres R, Mahalingam G, Bumbarger DJ, Li Y, et al. Structure and function of axo-axonic inhibition. Elife. 2021 12; 10. doi: 10.7554/eLife.73783.

Sento S, Ryugo DK. Endbulbs of Held and spherical bushy cells in cats: Morphological correlates with physiological properties. J Comp Neurol. 1989; 280:553–562.

Shapson-Coe A, Januszewski M, Berger DR, Pope A, Wu Y, Blakely T, Schalek RL, Li PH, Wang S, Maitin-Shepard J, Karlupia N, Dorkenwald S, Sjostedt E, Leavitt L, Lee D, Bailey L, Fitzmaurice A, Kar R, Field B, Wu H, et al. A connectomic study of a petascale fragment of human cerebral cortex. bioRxiv. 2021; https://www.biorxiv.org/content/early/2021/11/25/2021.05.29.446289, doi: 10.1101/2021.05.29.446289.

Shewchuk J. What is a Good Linear Finite Element? - Interpolation, Conditioning, Anisotropy, and Quality Measures. In: *Eleventh International Meshing Roundtable* Sandia National Laboratories; 2002. p. 115–126.

Shrestha BR, Chia C, Wu L, Kujawa SG, Liberman MC, Goodrich LV. Sensory Neuron Diversity in the Inner Ear Is Shaped by Activity. Cell. 2018 08; 174(5):1229–1246.e17. doi: 10.1016/j.cell.2018.07.007.

Smith PH, Joris PX, Carney LH, Yin TC. Projections of physiologically characterized globular bushy cell axons from the cochlear nucleus of the cat. J Comp Neurol. 1991; 304:387–407.

Smith PH, Rhode WS. Characterization of HRP-labeled globular bushy cells in the cat anteroventral cochlear nucleus. J Comp Neurol. 1987; 266:360–375.

Smith RL, Brachman ML. Response modulation of auditory-nerve fibers by AM stimuli: effects of average intensity. Hearing Res. 1980; 2(2):123–133.

Spirou GA, Chirila FV, von Gersdorff H, Manis PB. Heterogeneous Ca2+ influx along the adult calyx of Held: a structural and computational study. Neuroscience. 2008 Jun; 154(1):171–85. doi: 10.1016/j.neuroscience.2008.04.002.

Spirou GA, Rager J, Manis PB. Convergence of auditory-nerve fiber projections onto globular bushy cells. Neuroscience. 2005; 136(3):843–63. doi: 10.1016/j.neuroscience.2005.08.068.

Spirou GA, Brownell WE, Zidanic M. Recordings from cat trapezoid body and HRP labeling of globular bushy cell axons. J Neurophysiol. 1990; 63(5):1169–1190.

Sun S, Babola T, Pregernig G, So KS, Nguyen M, Su SSM, Palermo AT, Bergles DE, Burns JC, Müller U. Hair Cell Mechanotransduction Regulates Spontaneous Activity and Spiral Ganglion Subtype Specification in the Auditory System. Cell. 2018 08; 174(5):1247–1263.e15. doi: 10.1016/j.cell.2018.07.008.

Taberner AM, Liberman MC. Response properties of single auditory nerve fibers in the mouse. J Neurophysiol. 2005 Jan; 93(1):557–69. doi: 10.1152/jn.00574.2004.

Tolbert LP, Morest DK. The neuronal architecture of the anteroventral cochlear nucleus of the cat in the region of the cochlear nerve root: electron microscopy. Neuroscience. 1982; 7(12):3053–3067.

Tolbert LP, Morest DK, Yurgelun-Todd DA. The neuronal architecture of the anteroventral cochlear nucleus of the cat in the region of the cochlear nerve root: horseradish peroxidase labelling of identified cell types. Neuroscience. 1982; 7(12):3031–3052.

Turner NL, Macrina T, Bae JA, Yang R, Wilson AM, Schneider-Mizell C, Lee K, Lu R, Wu J, Bodor AL, Bleckert AA, Brittain D, Froudarakis E, Dorkenwald S, Collman F, Kemnitz N, Ih D, Silversmith WM, Zung J, Zlateski A, et al. Reconstruction of neocortex: Organelles, compartments, cells, circuits, and activity. Cell. 2022 03; 185(6):1082–1100.e24. doi: 10.1016/j.cell.2022.01.023.

Typlt M, Englitz B, Sonntag M, Dehmel S, Kopp-Scheinpflug C, Ruebsamen R. Multidimensional characterization and differentiation of neurons in the anteroventral cochlear nucleus. PLoS One. 2012; 7(1):e29965. doi: 10.1371/journal.pone.0029965.

Uchizono K. Characteristics of excitatory and inhibitory synapses in the central nervous system of the cat. Nature. 1965 Aug; 207(997):642–3. doi: 10.1038/207642a0.

Veres JM, Nagy GA, Vereczki VK, Andrási T, Hájos N. Strategically positioned inhibitory synapses of axo-axonic cells potently control principal neuron spiking in the basolateral amygdala. J Neurosci. 2014 Dec; 34(49):16194–206. doi: 10.1523/JNEUROSCI.2232-14.2014.

Villette V, Chavarha M, Dimov IK, Bradley J, Pradhan L, Mathieu B, Evans SW, Chamberland S, Shi D, Yang R, Kim BB, Ayon A, Jalil A, St-Pierre F, Schnitzer MJ, Bi G, Toth K, Ding J, Dieudonné S, Lin MZ. Ultrafast Two-Photon Imaging of a High-Gain Voltage Indicator in Awake Behaving Mice. Cell. 2019 Dec; 179(7):1590–1608.e23. doi: 10.1016/j.cell.2019.11.004.

Walton JP, Simon H, Frisina RD. Age-related alterations in the neural coding of envelope periodicities. J Neurophysiol. 2002 Aug; 88(2):565–78. doi: 10.1152/jn.2002.88.2.565.

Wang H, Kunkel DD, Martin TM, Schwartzkroin PA, Tempel BL. Heteromultimeric K^+ channels in terminal and juxtaparanodal regions of neurons. Nature. 1993; 365(6441):75–79.

Wang M, Zhang C, Lin S, Wang Y, Seicol BJ, Ariss RW, Xie R. Biased auditory nerve central synaptopathy is associated with age-related hearing loss. J Physiol. 2021 03; 599(6):1833–1854. doi: 10.1113/JP281014.

Wang X, Sachs MB. Neural encoding of single-formant stimuli in the cat. I. Responses of auditory nerve fibers. J Neurophysiol. 1993; 70(3):1054–1075.

Wang X, Sachs MB. Neural encoding of single-formant stimuli in the cat. II. Responses of anteroventral cochlear nucleus units. J Neurophysiol. 1994; 71(1):59–78.

Wang Y, Manis PB. Synaptic transmission at the cochlear nucleus endbulb synapse during age-related hearing loss in mice. J Neurophysiol. 2005 Sep; 94(3):1814–24. doi: 10.1152/jn.00374.2005.

Warr WB. Fiber degeneration following lesions in the anterior ventral cochlear nucleus of the cat. Exp Neurol. 1966; 14(4):453–474.

Waxman SG. Determinants of conduction velocity in myelinated nerve fibers. Muscle Nerve. 1980; 3(2):141–50. doi: 10.1002/mus.880030207.

Waxman SG, Bennett MV. Relative conduction velocities of small myelinated and non-myelinated fibres in the central nervous system. Nat New Biol. 1972 Aug; 238(85):217–9. doi: 10.1038/newbio238217a0.

Webster DB, Trune DR. Cochlear nuclear complex of mice. Am J Anat. 1982; 163(2):103–130.

Wei L, Karino S, Verschooten E, Joris PX. Enhancement of phase-locking in rodents. I. An axonal recording study in gerbil. J Neurophysiol. 2017 10; 118(4):2009–2023. doi: 10.1152/jn.00194.2016.

Wilke SA, Antonios JK, Bushong EA, Badkoobehi A, Malek E, Hwang M, Terada M, Ellisman MH, Ghosh A. Deconstructing complexity: serial block-face electron microscopic analysis of the hippocampal mossy fiber synapse. J Neurosci. 2013 Jan; 33(2):507–22. doi: 10.1523/JNEUROSCI.1600-12.2013.

Willott JF, Demuth RM, Lu SM. Excitability of auditory neurons in the dorsal and ventral cochlear nuclei of DBA/2 and C57BL/6 mice. Exp Neurol. 1984; 83(3):495–506.

Witvliet D, Mulcahy B, Mitchell JK, Meirovitch Y, Berger DR, Wu Y, Liu Y, Koh WX, Parvathala R, Holmyard D, Schalek RL, Shavit N, Chisholm AD, Lichtman JW, Samuel ADT, Zhen M. Connectomes across development reveal principles of brain maturation. bioRxiv. 2021; https://www.biorxiv.org/content/early/2021/06/03/2020.04.30.066209, doi: 10.1101/2020.04.30.066209.

Woodhull AM. Ionic blockage of sodium channels in nerve. J Gen Physiol. 1973 Jun; 61(6):687–708. doi: 10.1085/jgp.61.6.687.

Xie R, Manis PB. Glycinergic synaptic transmission in the cochlear nucleus of mice with normal hearing and age-related hearing loss. J Neurophysiol. 2013 Oct; 110(8):1848–59. doi: 10.1152/jn.00151.2013.

Xie R, Manis PB. Target-specific IPSC kinetics promote temporal processing in auditory parallel pathways. J Neurosci. 2013 Jan; 33(4):1598–614. doi: 10.1523/JNEUROSCI.2541-12.2013.

Xu-Friedman MA, Regehr WG. Retrograde tuning of tuning. Neuron. 2008 Jul; 59(1):3–5. doi: 10.1016/j.neuron.2008.06.013.

Yang Y, Ramamurthy B, Neef A, Xu-Friedman MA. Low Somatic Sodium Conductance Enhances Action Potential Precision in Time-Coding Auditory Neurons. J Neurosci. 2016 11; 36(47):11999–12009. doi: 10.1523/JNEUROSCI.1475-16.2016.

Yin TCT, Smith PH, Joris PX. Neural Mechanisms of Binaural Processing in the Auditory Brainstem. Compr Physiol. 2019 09; 9(4):1503–1575. doi: 10.1002/cphy.c180036.

Young ED, Robert JM, Shofner WP. Regularity and latency of units in ventral cochlear nucleus: Implications for unit classification and generation of response properties. J Neurophysiol. 1988; 60(1):1–29.

Zheng Z, Lauritzen JS, Perlman E, Robinson CG, Nichols M, Milkie D, Torrens O, Price J, Fisher CB, Sharifi N, Calle-Schuler SA, Kmecova L, Ali IJ, Karsh B, Trautman ET, Bogovic JA, Hanslovsky P, Jefferis GSXE, Kazhdan M, Khairy K, et al. A Complete Electron Microscopy Volume of the Brain of Adult Drosophila melanogaster. Cell. 2018 07; 174(3):730–743.e22. doi: 10.1016/j.cell.2018.06.019.

Zilany MSA, Bruce IC, Carney LH. Updated parameters and expanded simulation options for a model of the auditory periphery. J Acoust Soc Am. 2014 Jan; 135(1):283–6. doi: 10.1121/1.4837815.

Key Resources

Reagent type (species) or resoure	Designation	Source or reference	Identifiers	Additional Information
Strain, strain background (Mouse)	FVB/NJ	Jackson Laboratory	JAX Stock # 001800; RRID:IMSR_JAX:001800	
Chemical compound, drug	2,2,2 – Tribromoethanol	TCI Chemicals	T1420	
Chemical compound, drug	tert-Amyl Alcohol	TCI Chemicals	P0059	
Chemical compound, drug	xylocaine	Sigma	PHR1257	
Chemical compound, drug	heparin	Sigma	H5515	
Chemical compound, drug	Cacodylic acid	EM Sciences	RT12201	
Chemical compound, drug	glutarldeyhde	EM Sciences	100503-972	
Chemical compound, drug	Paraformaldehyde - EM grade	source	RT19208	
Chemical compound, drug	calcium chloride	Sigma	223506	
Chemical compound, drug	potassium ferrocyanide	EM Sciences	RT20150	
Chemical compound, drug	Nanopure water	Barnstead International	D11901	
Chemical compound, drug	osmium tetroxide	EM Sciences	19132	
Chemical compound, drug	thiocarbohydrazide	EM Sciences	21900	
Chemical compound, drug	uranyl acetate	EM Sciences	22400	
Chemical compound, drug	lead nitrate	EM Sciences	17900	
Chemical compound, drug	ethanol	Fisher Chemical	A962P-4	
Chemical compound, drug	acetone	Fisher Chemical	A962P-4	

Key Resources (continued)

Reagent type (species) or resource	Designation	Source or reference	Identifiers	Additional Information
Chemical compound, drug	Durcopan resin	EM Sciences	14040	
Chemical compound, drug	Aclar strips	EM Sciences	50425-10	
Chemical compound, drug	Silver paint	Ted Pella	16031	
Chemical compound, drug	Gold/palladium sputter target	Ted Pella	91651	
Microscope	Merlin Scanning Electron Microscope	Zeiss		
Core	National Center for Microscopy and Imaging Research	University of California at San Diego	RRID:SCR_016627	https://ncmir.ucsd.edu
Software	Seg3D		RRID:SCR_002552	www.seg3d.org
Software	Blender 2.9		RRID:SCR_008606	https://www.blender.org
Software	syGlass 1.7	IstoVisio, Inc.	RRID:SCR_017961	https://www.syglass.io
Software	NEURON V7.7-V8.0		RRID:SCR_005393	http://www.neuron.yale.edu
Software	Python V3.7-3.10		RRID:SCR_008394	https://www.python.org
Software	cnmodel			https://github.com /cnmodel/cnmodel.git
Software	Prism V9.3	GraphPad, Inc.	RRID:SCR_002798	https://www.graphpad.com
Software	Adobe Illustrator V26.0.3	Adobe, Inc.	RRID:SCR_010279	https://www.adobe.com/products/illustrator.html

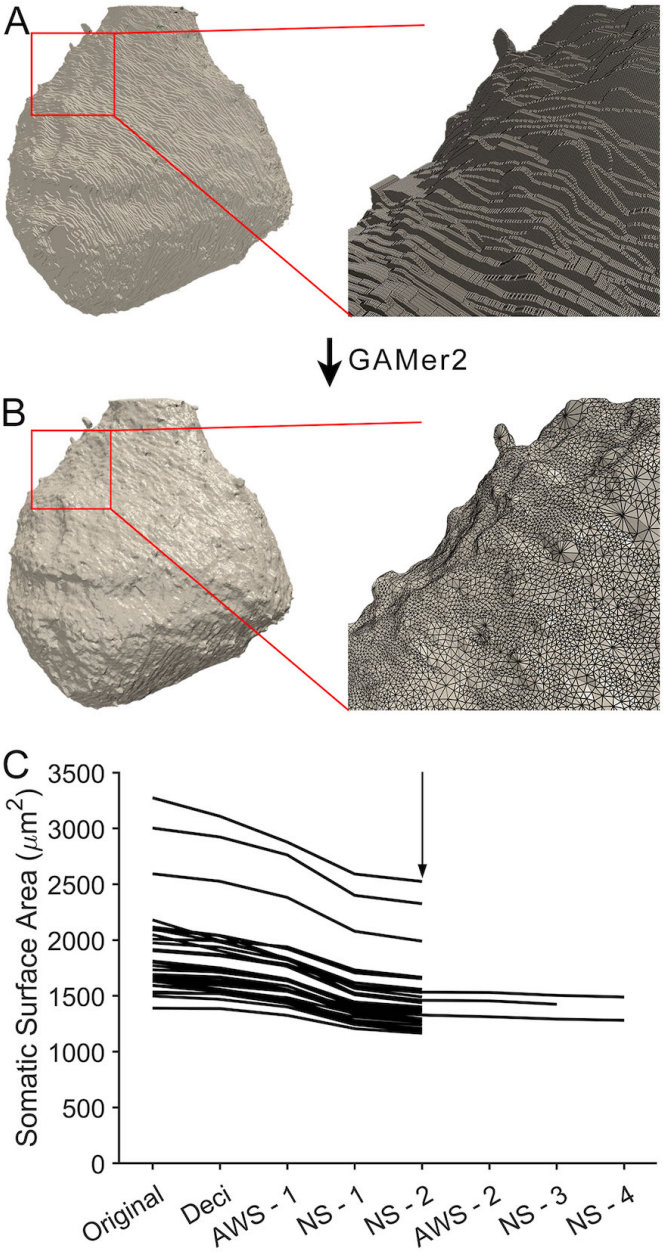

Figure 1–Figure supplement 1. Steps in mesh generation and compartmental representation from EM volumes, related to Figure 1A. (**A**) Cell membranes of objects (cell body of a bushy cell in this case) were traced and assembled into stacks. Each tissue section appears as a slab, seen clearly in expanded view at right. The slab thickness is the 60nm section thickness used during imaging. (**B**) The GAMer2 algorithm (***Lee et al., 2020b***) was used to create a mesh surface enclosing the volume, comprised of isosceles triangles, that preserved real surface irregularities such as small protrusions. (**C**) Decimation and smoothing algorithms were successively applied until the meshed surface area reached an asymptote (vertical arrow). The change in area for all reconstructed somas are shown. After testing multiple cycles on three cells, values at NS-2 stage (see Methods) were used for all cells.

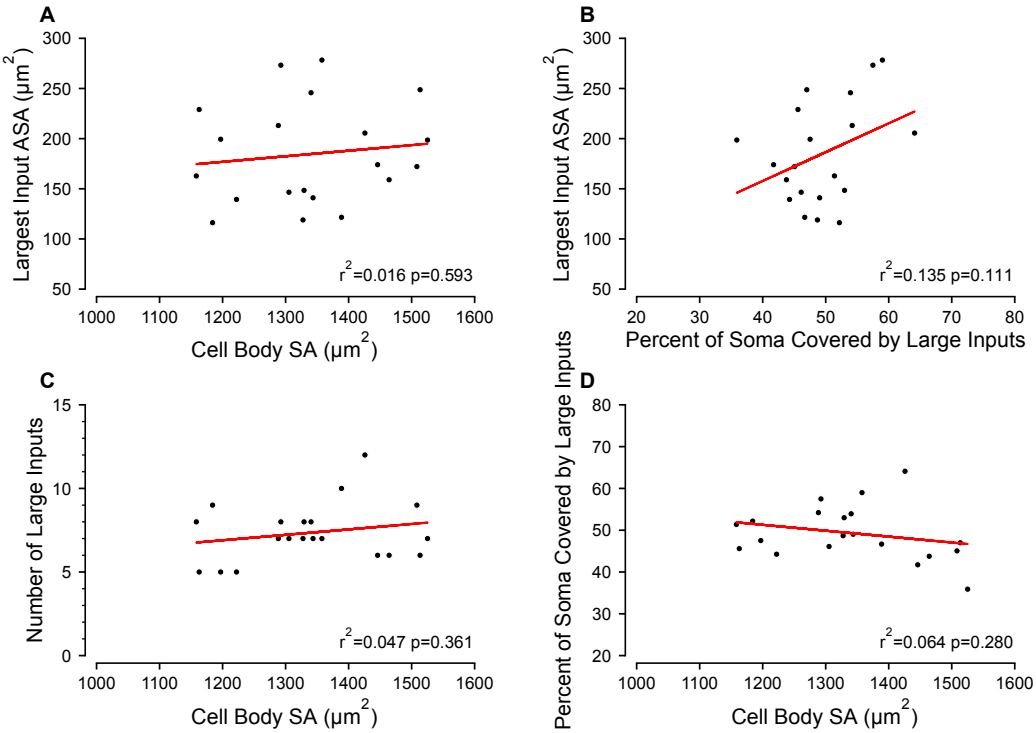

Figure 2–Figure supplement 1. Morphological correlations for synapse and somatic area, related to Figure 2C,D. (**A**) There was no relationship between cell body surface area (SA) and the apposed surface area (ASA) of the largest input. (**B**) There was a weak correlation between the somatic coverage by large inputs and the largest input area. (**C**) There was no correlation between cell body area and the number of large inputs. (**D**) There was no correlation between the area coverage by large inputs and the cell body area.

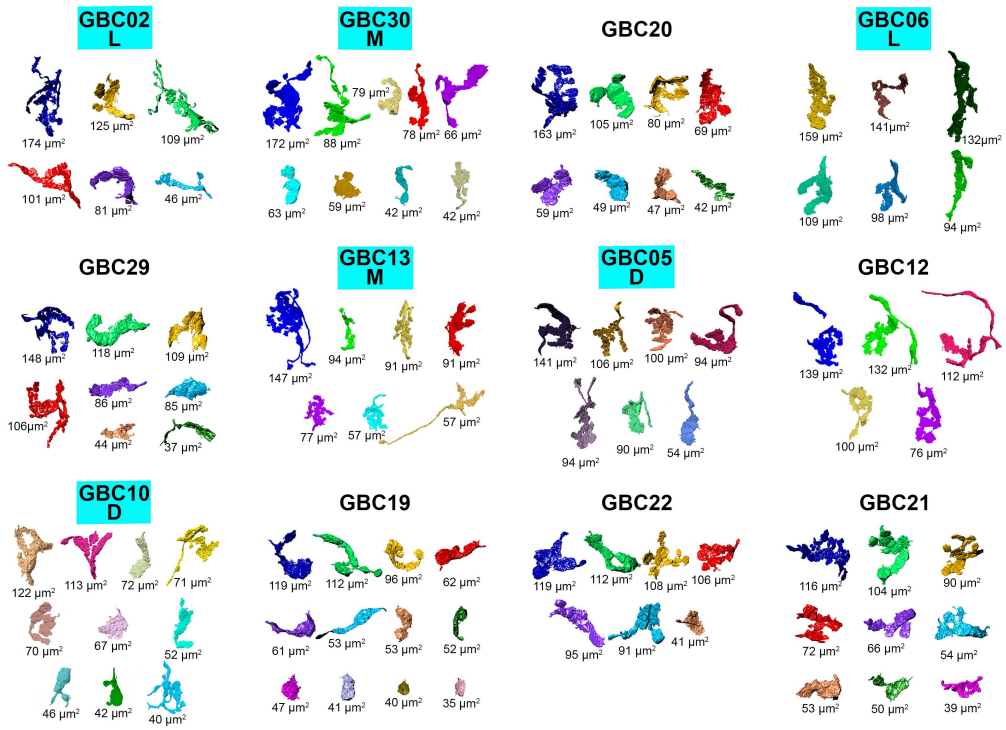

Figure 2–Figure supplement 2. Large somatic terminals onto each globular bushy cell (GBC) that fit the Coincidence Detection model, related to Figure 2E. Terminal groups are arranged from top left to bottom right in order of decreasing size of their largest input. Apposed surface area (ASA) is indicated next to each terminal. The number of terminals ranges from 5 (GBC12) to 12 (GBC19). Six of these GBCs (label enclosed in blue box) had dendrites fully reconstructed and were used for compartmental modeling. The extent of their local dendrite branching is indicated by L, low; M, moderate; D, dense. Scale bar omitted because these are 3D structures and most of the terminal would be out of the plane of the scale bar.

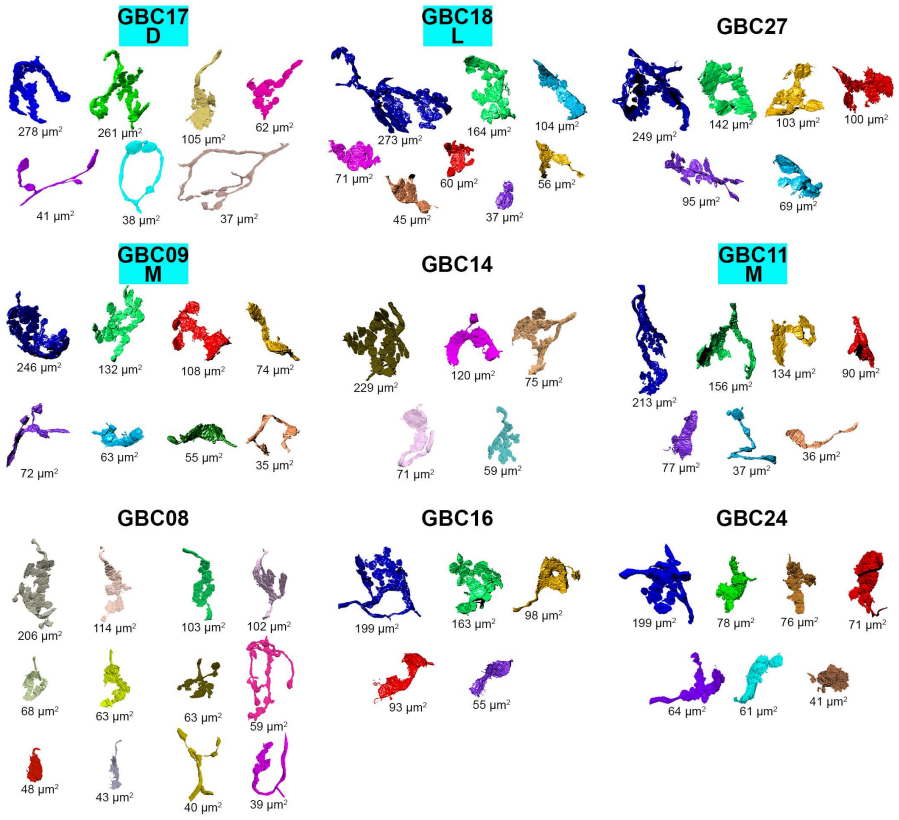

Figure 2–Figure supplement 3. Large somatic terminals onto each globular bushy cell (GBC) that fit the mixed Coincidence Detection/ First-Arrival model, related to Figure 2F. Terminal groups are arranged from top left to bottom right in order of decreasing size of their largest input. Apposed surface area (ASA) is indicated next to each terminal. The number of terminals ranges from 5 (GBC14, GBC16) to 12 (GBC08). Four of these GBCs (label enclosed in blue box) had dendrites fully reconstructed and were used for compartmental modeling. The extent of their local dendrite branching is indicated by L, low; M, moderate; D, dense. Scale bar omitted because these are 3D structures and most of the terminal would be out of the plane of the scale bar.

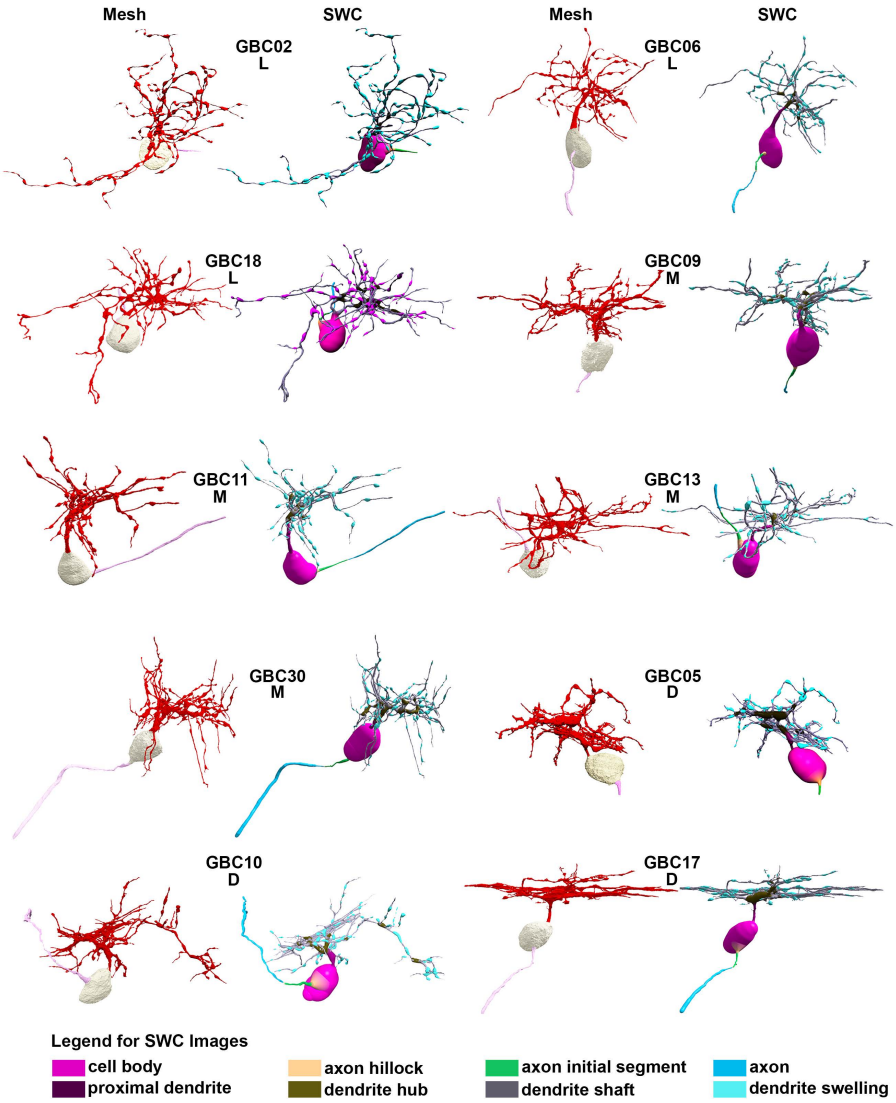

1645

Figure 4–Figure supplement 1. Segmented globular bushy cells (GBC) and their representations for compartmental modeling, related to Figure 4A and B. Panels are labeled by cell number. For each GBC, the segmentation as computational meshes is depicted at left. Cell bodies are light grey, dendrites are red, and axons are pink. Cells are aligned to permit the most encompassing views of their dendrites. Meshes were converted to SWC format, which represents structures as a series of linked skeleton points with associated radius, using 3D virtual reality software (syGlass). The SWC representations are shown at right for each pair of images. Axon and dendrite subcompartments were annotated during SWC creation, which permitted quantification of their surface areas. Cells are clustered into three groups by the extent of local dendrite branching and braiding: low (L: GBCs 02, 06, 18), moderate (M: GBCs 09, 11, 13, 30), and dense (D: GBCs 05, 10, 17). Cellular compartments are color coded in the SWC files, as depicted in the legend. Scale bar is not included because it does not apply throughout the depth of the 3D structure. Images scaled to fit within figure panels so cells are pictured at different scales.

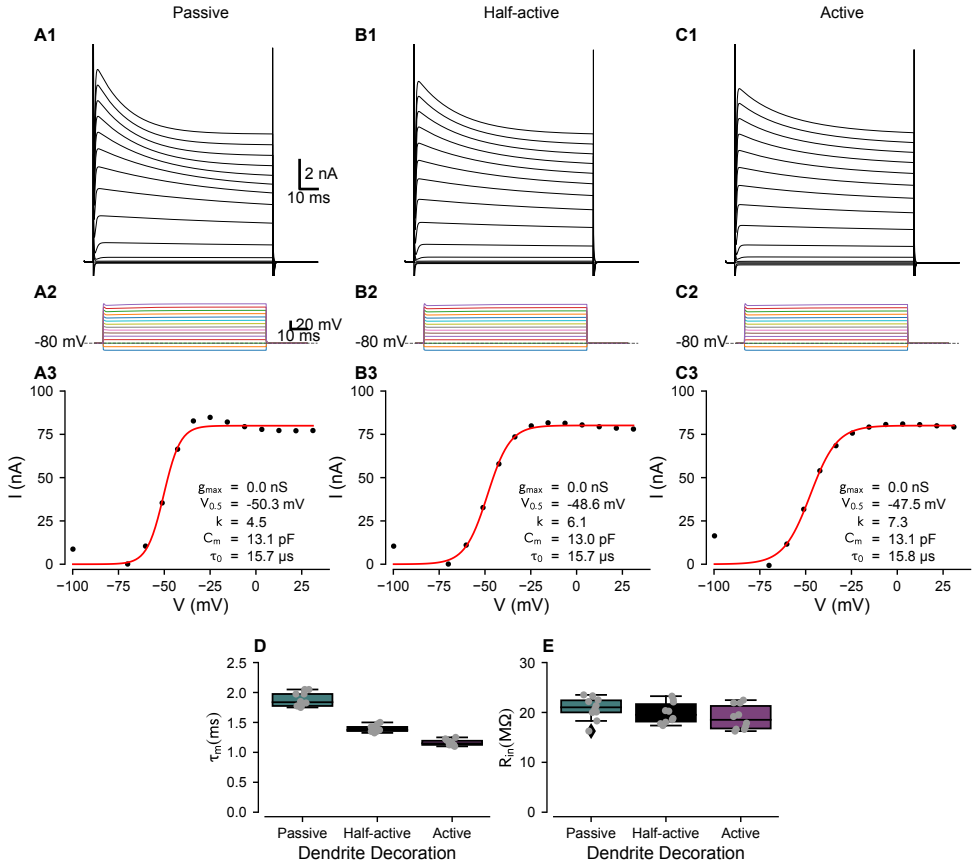

Figure 4–Figure supplement 2. Conductance scaling using voltage clamp simulations for different patterns of dendrite decoration, related to Figure 4C. Voltage-clamp simulations were used to compute total channel densities to match experimental data for different dendritic decoration configurations. (**A**) Passive dendrites. (**A1**): voltage clamp protocol with steps as in panel (**A2**). The transients at the start and end of the steps represent the charging of the cell membrane capacitance, which was not compensated in the model cell. (**A3**) Steady-state conductance calculated from the data in A1. The inset text indicates the fits to a Boltzmann function of the form

$$g(V) = \frac{1}{1 + e^{-(V - V_{0.5})/k}}$$

where $V_{0.5}$ is the half-activation voltage and k is the slope factor. C_m is the cell capacitance, calculated from an exponential fit to the initial charging curve for small negative voltage steps, and τ_0 is the clamp charging time constant (fastest time constant, representing somatic capacitance). (**B**) and (**C**) 1-3 are in the same format as (**A1-3**), with different channel decoration of the dendrites. (**D**) Input resistance measures from the 10 completely reconstructed cells for each of the decoration conditions from current-clamp simulations (see Figure 4–*Figure Supplement 3*). Boxplots: Shaded area indicates interquartile distances, whiskers indicate 5-95% confidence limits. (**E**) Time constant measurements from the 10 completely reconstructed cells for each of the decoration conditions from current clamp simulations. Boxplots are formatted as in (**D**). Scale bars in (**A1**) apply to (**B1**) and (**C1**). Scale bars in (**A2**) apply to (**B2**) and (**C2**).

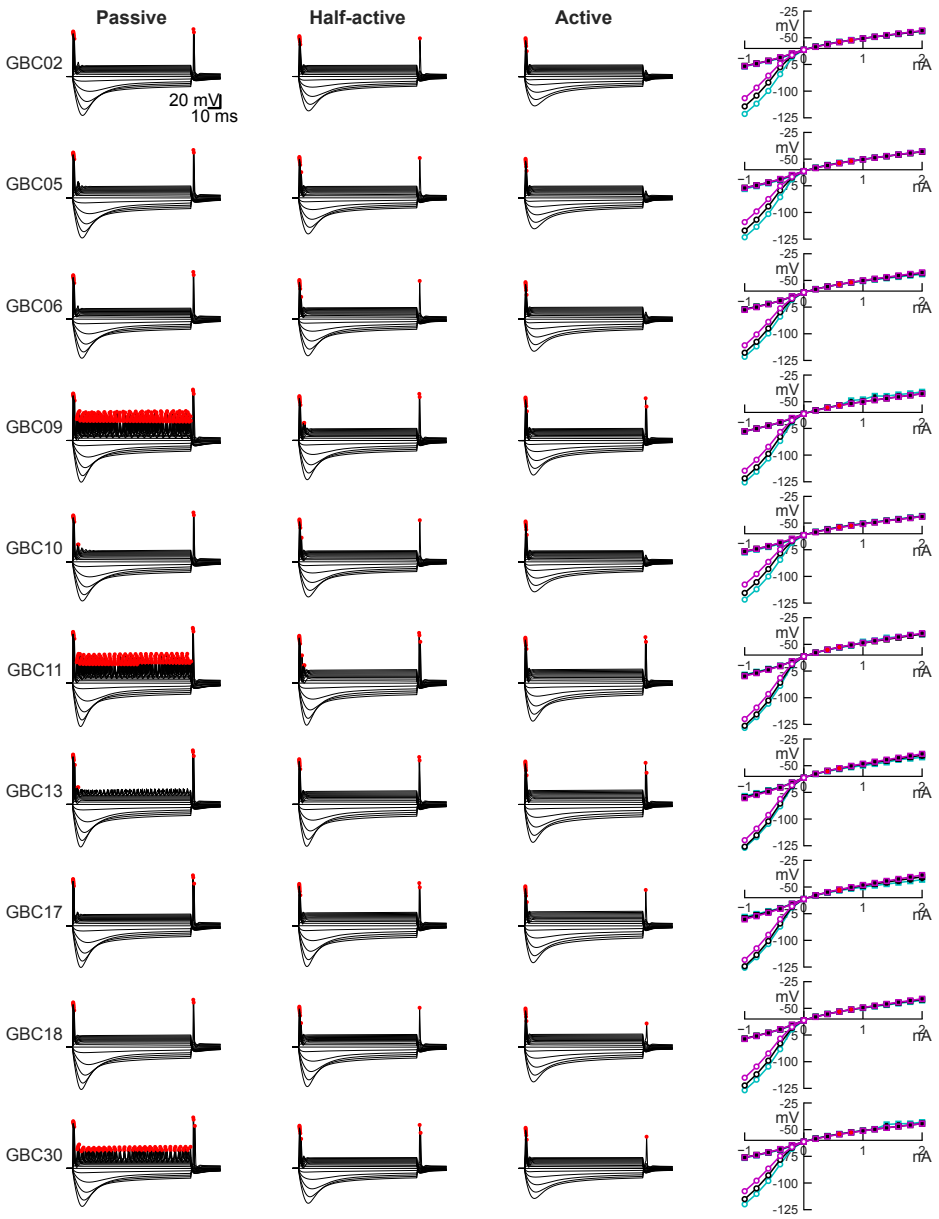

Figure 4–Figure supplement 3. Current-clamp responses for all 10 complete bushy cells for each of the ion channel decoration conditions, related to Figure 4D and E. All current-voltage relationships show traces from -1 to + 2 nA, in 0.2 nA steps. Action potentials are indicated by red dots. The calibration bar in the top row applies to all traces. The right-most column shows the steady-state current-voltage relationships (squares) and peak (circles, for hyperpolarization only) for each of the decoration conditions (Passive: cyan; Half-active: black, Active: magenta). Note that some model cells (GBCs 09, 11, 30) show small repetitive spikes with stronger depolarization with the passive dendrites. Most cells show spikes at anodal break, but these are attenuated or absent when the dendrites are fully active.

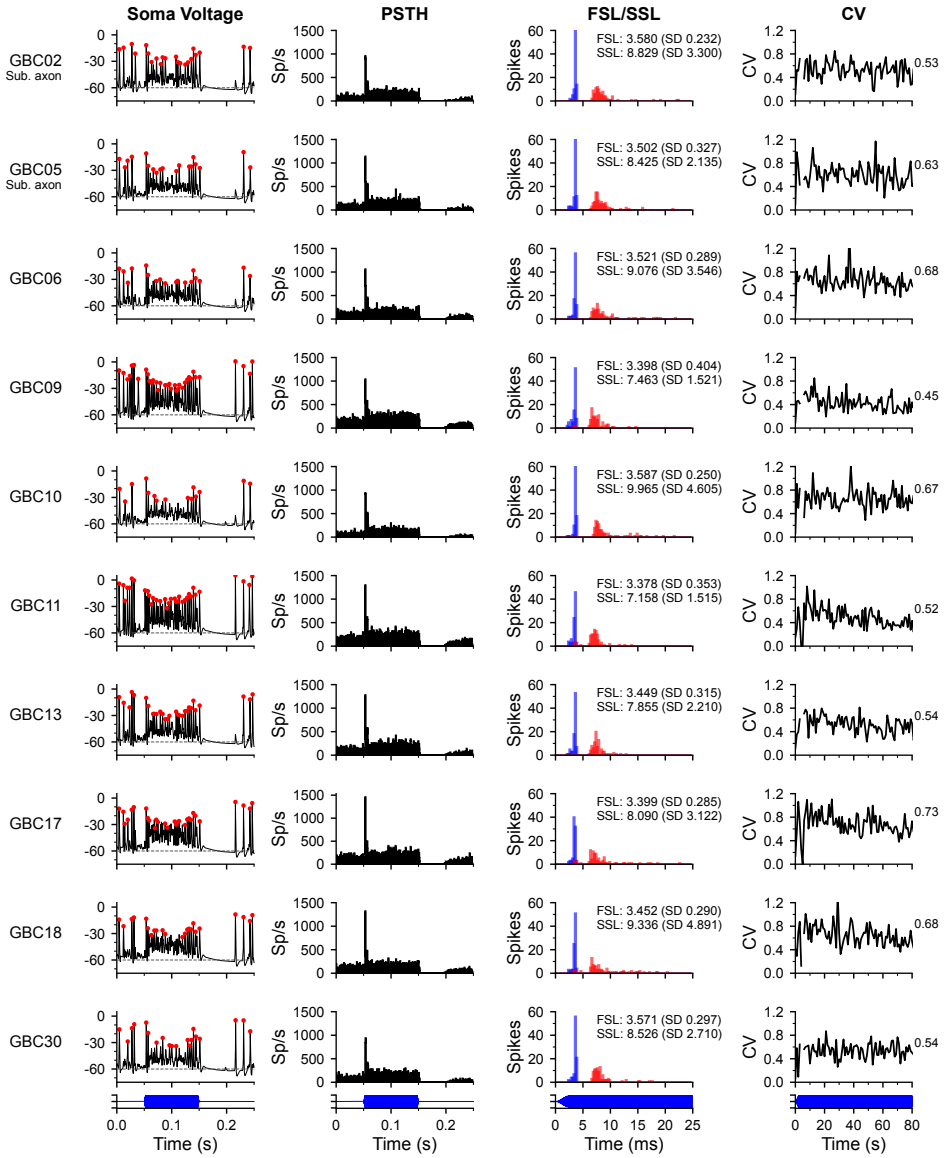

Figure 4–Figure supplement 4. Peri-stimulus time histograms, spike latencies and interpsike interval regularity in response to tone bursts at characteristic frequency, related to Figure 4F-H. Each row shows the responses for one cell. The reconstructed axon of cells GBC02 and GBC05 left the volume prior to myelination and were simulated with a substitute axon ("Sub. axon") that had the average hillock, initial segment and myelinated axon lengths and diameters from the other 8 cells. Otherwise, each cell was simulated using its own reconstructed axon. The first column (Soma Voltage) shows the somatic voltage for one trial for a stimulus at the characteristic frequency at 30 dB SPL. The stimulus starts after 50 ms and is 100 ms in duration. The PSTH column shows the spike rate as a function of time averaged over 100 repetitions of the tone pip, with 0.5 ms bins. The (FSL/SSL) column shows the first spike latency distribution (FSL, blue) and second spike latency distribution (SSL, red) ; text shows the mean and SD of the FSL and SSL. The rightmost column plots the coefficient of variation (CV) of interspike intervals corrected for a 0.7 ms refractory period (CV'). . Intervals beginning less than 25 ms before the end of the stimulus were not included to minimize end effects. The CV' value is indicated to the right of each plot. All CV' values fall in the range of 0.3-0.7 reported for mouse primary-like neurons (***Roos and May, 2012***). The bottom row of plots shows the stimulus waveform timing for each column (blue).

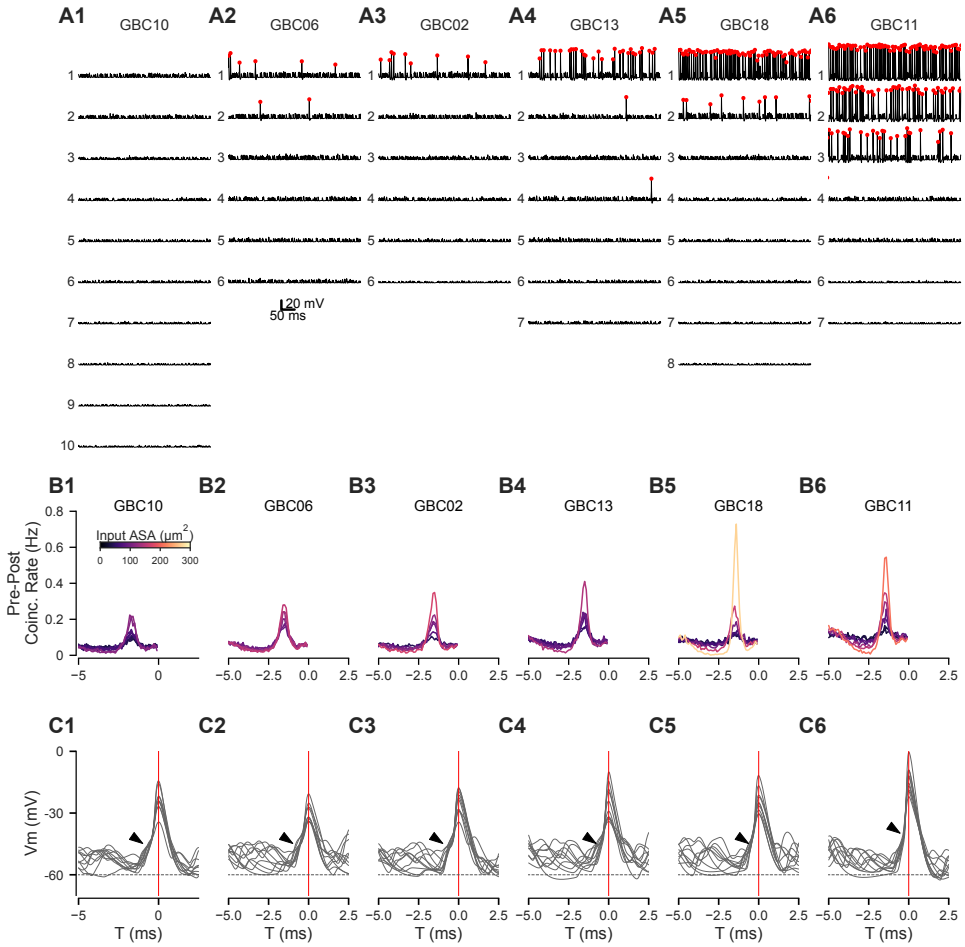

Figure 5–Figure supplement 1. Cross-correlation plots for 6 additional modeled cells , related to Figure 5A-C. Each cell is plotted in the same format as in ***Figure 5***A, D and E. Summary information is presented in panels ***Figure 5***D-J.

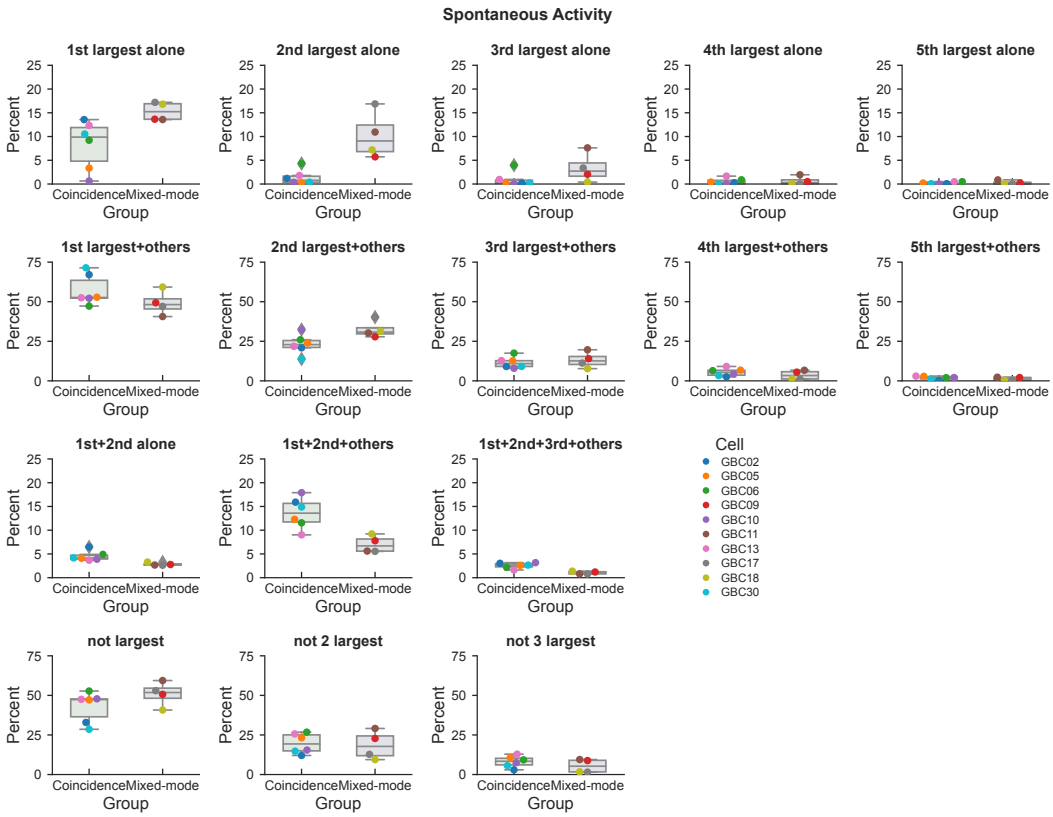

Figure 5–Figure supplement 2. Contributions of different input patterns to postsynaptic spiking, related to Figure 5E. For each panel, the contributions are measured in gobular bushy cells GBC02, GBC05, GBC06, GBC10, GBC13, GBC30 ("Coincidence" group) and contributions measured in the mixed-mode group of cells GBC09, GBC11, GBC17, GBC18 ("Mixed-mode" group). The panels are titled according to the particular patterns of input, and plot the percent of postsynaptic spikes that were generated by each pattern. Cell colors are the same as in other figures. The bars show the median, interquartile distances, and 5-95% whiskers. Points that fall outside of the expected distribution are indicated with diamonds. Results are shown for spontaneous activity. Individual cells are noted by the color in the legend.

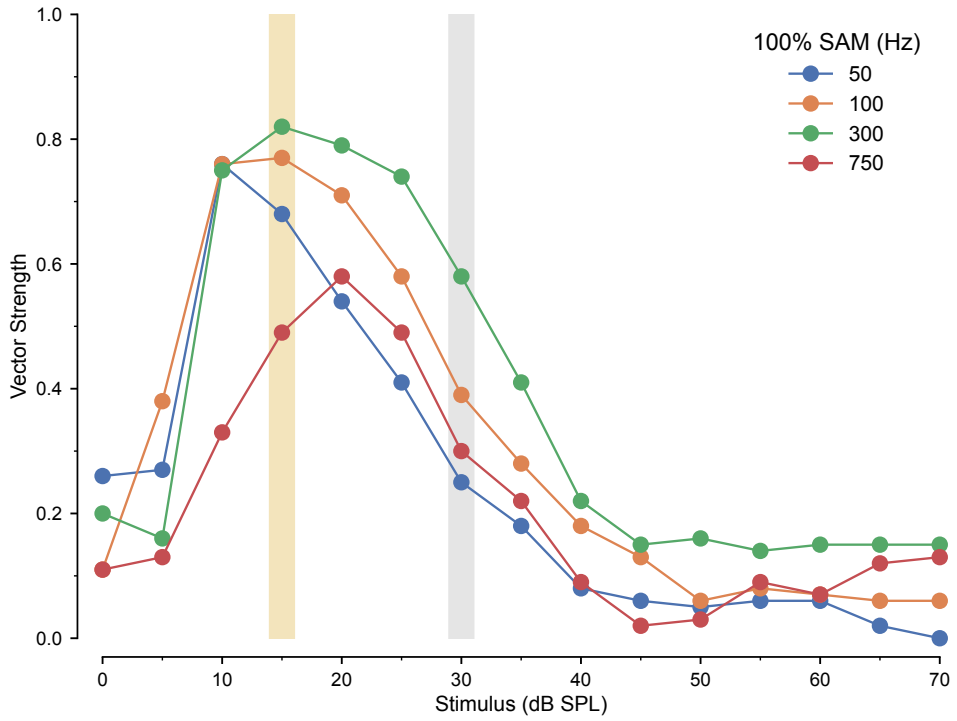

Figure 6–Figure supplement 1. Synchronization to stimulus envelope as a function of average stimulus intensity in ANF inputs, related to Figure 6F, P1 and P2. Vector strength of response to 100% SAM across frequency for the ANF model. Carrier frequency was 16 kHz. Color bars indicate 15 dB SPL (gold) used in ***Figure 6***, O1-4 and P1, and 30 dB SPL (gray), as used in ***Figure 6***, P2.

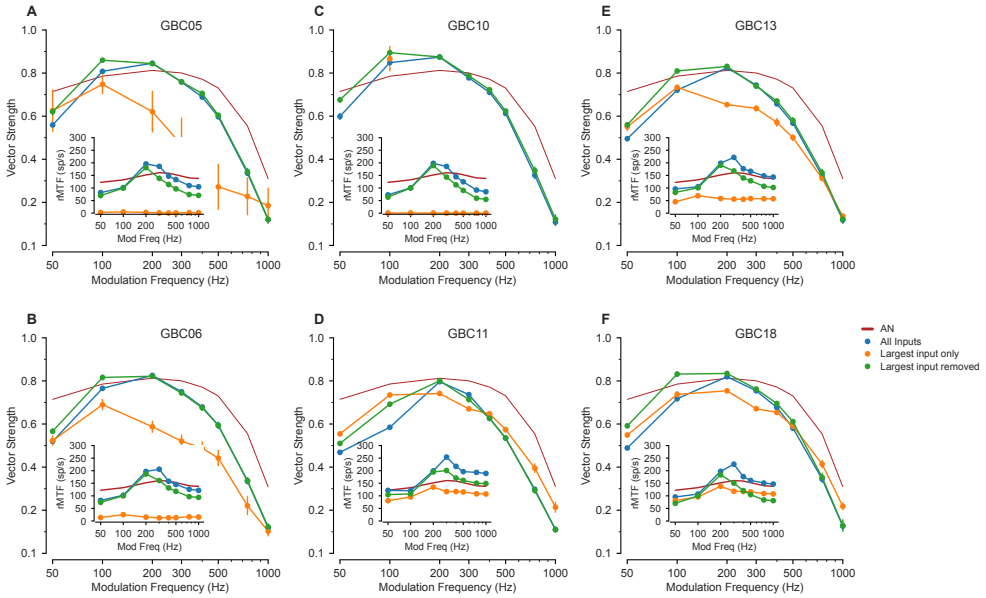

Figure 6–Figure supplement 2. Vector strength of the 6 other globular bushy cells (GBCs) in response to 100% SAM tones at frequencies from 50 to 1000 Hz on a 16kHz carrier at 15 dB SPL, related to Figure 6O1-4. These simulation results are also included in Figure6–*Figure 6*P1. Each plot shows vector strength for 3 (or in the case of GBC 17, 4) different synaptic input configurations. The vertical lines indicate the SD of the vector strength (VS) computed as described in the Methods. Insets show the rate modulation transfer function (rMTF; see Methods and Materials for calculation) across SAM frequencies for each synaptic configuration. (**A**) Cell GBC05, (**B**) Cell GBC06, (**C**) Cell GBC10, (**D**) Cell GBC11, (**E**) Cell GBC13, (**F**) Cell GBC18. GBC10 had too few spikes with only the largest input to compute VS above 100 Hz.

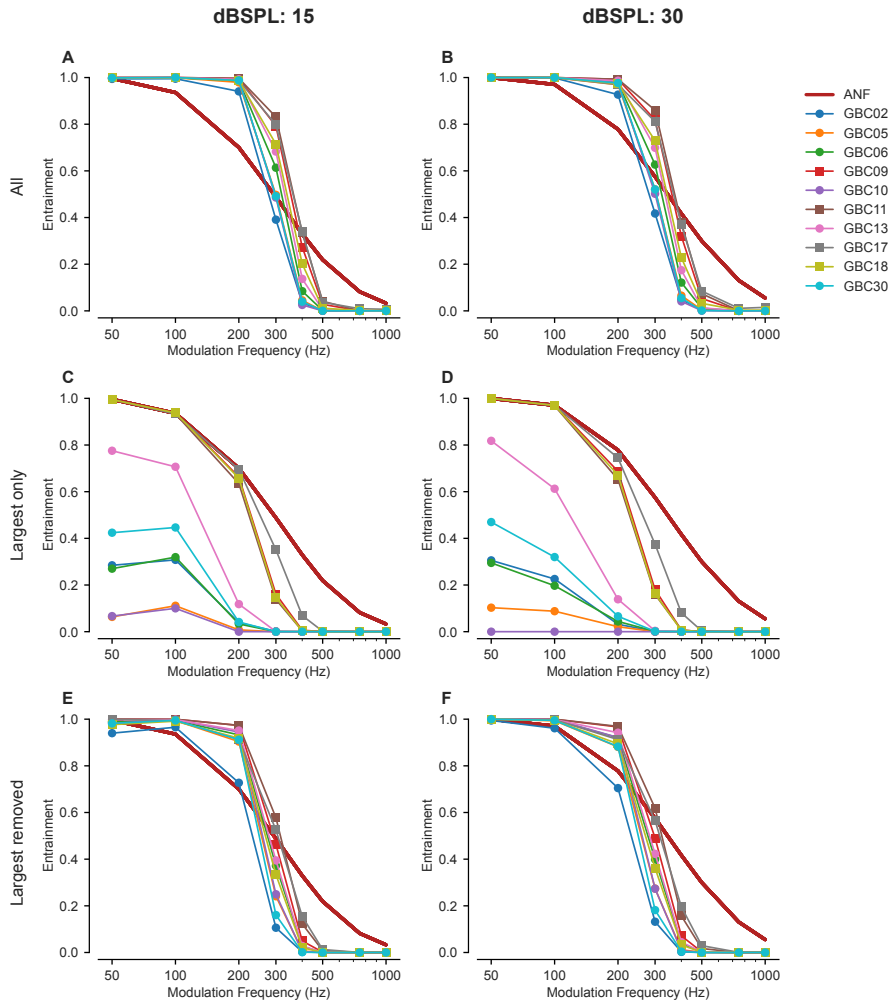

Figure 6–Figure supplement 3. Spike entrainment across all globular bushy cells (GBCs) at 15 and 30 dB SPL when different combinations of inputs are active, related to Figure 6P1-2. Entrainment could exceed ANF values when all (A, B) or all except the largest (E, F) inputs were active. The largest inputs alone (C, D) showed entrainment less than or equal to that of ANFs. Symbols: Mixed-mode cells: □, coincidence-detection cells: ○. ANFs: dark red line.

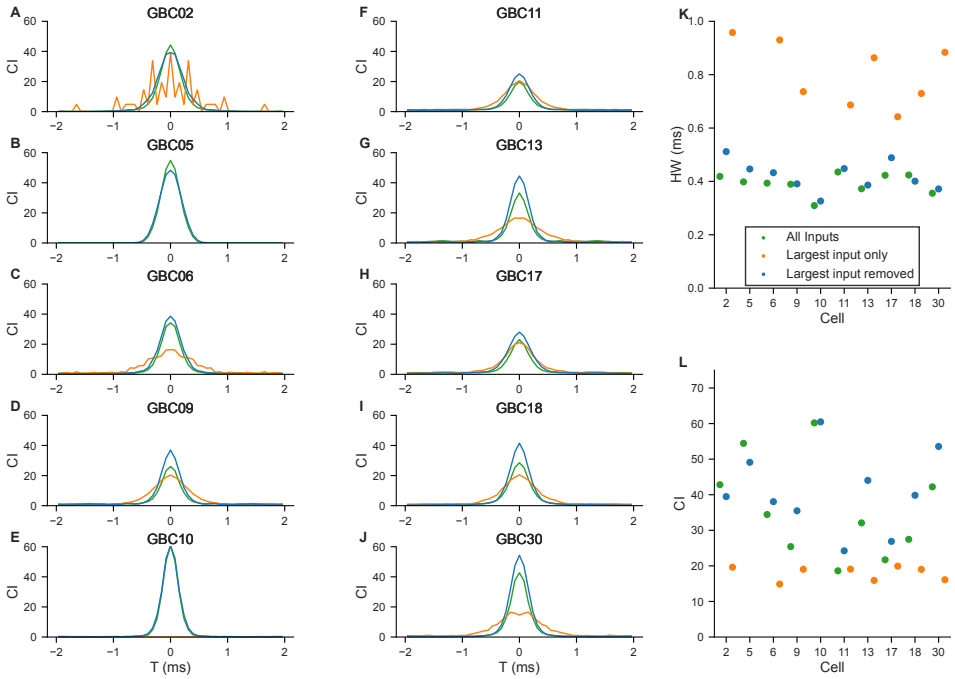

Figure 6–Figure supplement 4. Shuffled autocorrelations (SACs) in response to click trains show importance of weaker inputs in improving temporal precision, related to Figure 6M. SACs were computed for click evoked spike trains as shown in ***Figure 6***. (**A-J**) SACs computed for each of the globular bushy cells (GBCs) for 3 different input configurations (colors are indicated in panel (**K**)). For GBC05 (**B**) and GBC10 (**E**), there were insufficient spikes in the largest input only condition for the SAC calculation. (**K**) Half-width of the SAC for each cell and configuration. computed from Gaussian fits to the SACs in panels (**A-J**). (**L**) SAC correlation index (CI) at 0 time for each cell and configuration.

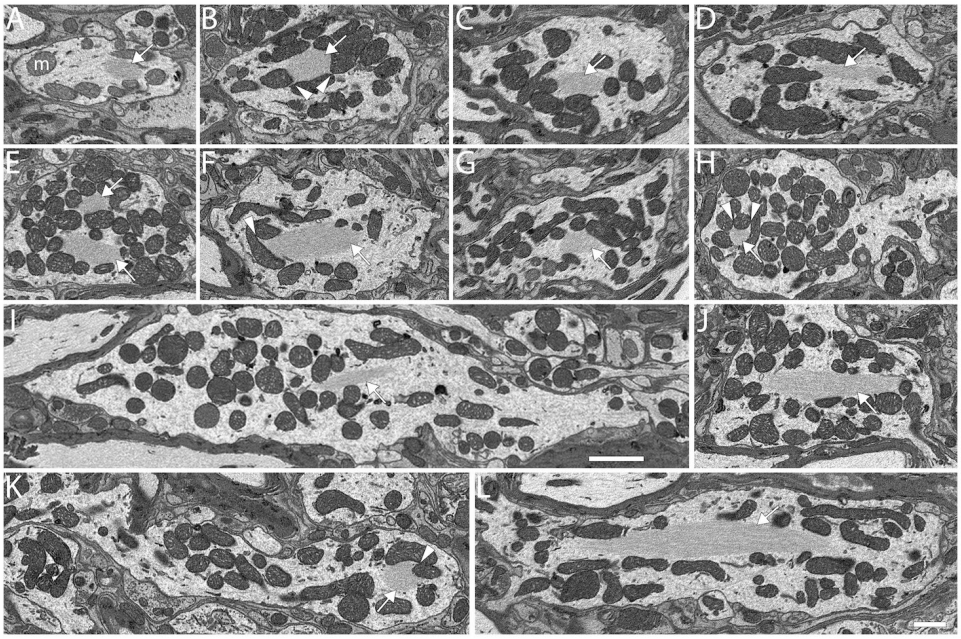

Figure 7–Figure supplement 1. Dendritic Hubs, related to Figure 7G and J. Filament core (white arrows) in primary globular bushy cell (GBC) hubs and dendrite of one multipolar cell (MC). A-L. MC04, GBCs 05, 14, 27, 08, 10, 09, 24, 17, 30, 29, 16. Filaments appear in close apposition to mitochondrion outer membranes and can fill narrow spaces defined by those membranes (white arrowheads). Scale bar = 1 micron in panel L applies to all panels except panel I scale bar = 2 microns.